UNIVERSITY OF SOUTHAMPTON

FACULTY OF PHYSICAL AND APPLIED SCIENCES

Physics

Quantum Optics of Electrons in Graphene

by

Paul Clark

Thesis for the degree of Doctor of Philosophy

May 2017

UNIVERSITY OF SOUTHAMPTON

ABSTRACT

FACULTY OF PHYSICAL AND APPLIED SCIENCES

Physics

Doctor of Philosophy

QUANTUM OPTICS OF ELECTRONS IN GRAPHENE

by Paul Clark

The unique properties of graphene's band structure can lead to negative refraction of charge carriers incident on PN junctions. When coupled with an angular dependent transmission probability this can be utilised to form a novel split path interferometer. Many practical challenges are present and novel methods of fabrication are required to realise such a device. A large mean free path is required in order to achieve ballistic transport; a fundamental requirement of such a lensing device. Graphene on a hexagonal boron nitride (hBN) substrate is used in order to remove as many scattering sites as possible to enable the devices to be modelled using ballistic transport. Bubbles between graphene and boron nitride flakes are found and a method for their removal explained. Equipment was modified to allow the use of the latest graphene flake dry transfer methods, which enable the fabrication of hBN-graphene-hBN sandwich devices with one dimensional edge contacts. Multiple device designs are proposed which would exhibit interesting physics and give evidence for negative refraction in graphene and for the angular transmission probability of Klein tunnelling. The possibility of using He ion carving to produce a very small quantum point contact was explored and a nanoribbon with a width of 8 nm was fabricated and measured.

Contents

Declaration of Authorship

I, Paul Clark , declare that the thesis entitled *Quantum Optics of Electrons in Graphene* and the work presented in the thesis are both my own, and have been generated by me as the result of my own original research. I confirm that:

- this work was done wholly or mainly while in candidature for a research degree at this University;
- where any part of this thesis has previously been submitted for a degree or any other qualification at this University or any other institution, this has been clearly stated;
- where I have consulted the published work of others, this is always clearly attributed;
- where I have quoted from the work of others, the source is always given. With the exception of such quotations, this thesis is entirely my own work;
- I have acknowledged all main sources of help;
- where the thesis is based on work done by myself jointly with others, I have made clear exactly what was done by others and what I have contributed myself;
- none of this work has been published before submission

Signed:.....

Date:.....

Acknowledgements

There are many people whom I wish to acknowledge and give thanks to for help during this PhD. Prof. Hendrik Ulbricht for your continued support, guidance and encouragement. Zondy Webber for technical help with cleanroom use and helping with access to the Jeol e-beam. All of the technicians in the Mountbatten building who have helped train me on the use of their extensive range of equipment and advice with nanofabrication techniques. To Dr James Bateman, David Hempston, Muddassur Rashid, Jamie Vovrosh and Dr Nathan Cooper for excellent stimulating discussions in the office and for great suggestions of solutions to whatever the current problem was. The late Prof Peter de Groot for kindly allowing me the use of his cryostat and his help and patience in guiding me on its use. My family for their encouragement and support throughout the years. My parents Martin and Patricia, my brothers Daniel and Lewis.

Lastly to Gemma for your patience and support throughout my PhD and beyond, I am forever indebted to you.

Chapter 1

Introduction

The ability to have ballistic transport of charge carriers in graphene opens up a new line of methods which can be used to explore quantum optics of electrons. Analogies can be drawn between photons and ballistic electrons which leads to the investigation of comparable quantum optics experiments.

Quantum optics of electrons has already seen some early experimental implementations, for example Neder et al (1) investigated using an AlGaAs-GaAs two dimensional electron gas in the quantum Hall regime to form a double Mach-Zender Interferometer with quantum point contacts as beam splitters. They show that two indistinguishable electrons can be interfered to reproduce the famous Hanbury Brown and Twiss experiment (2). This was a progression on the work of Henny (3). Using a beam splitter in AlGaAs-GaAs, Oliver (4) has shown antibunching of electrons consistent with treating the Hanbury Brown and Twiss experiment with Fermi-Dirac statistics. Loudon wrote a very nice paper to compare theoretically the difference in statistics if Bosons or Fermions hit a 50/50 beam splitter (5) and therefore linked electrons to the sound body of quantum optics theory.

The work presented here represents a step towards the realisation of quantum

computing with continuous variables, in contrast to the much more common use of the electron spin as qubit. It represents an independent and new attempt to use the motion of electrons in solid state structures as a resource for quantum information and ultimately quantum computation (6).

If our new scheme could be shown to work, then its clear advantage would be the scaling up to include many gates by simply adding more beam splitters. Coherence would only need to be preserved for each single step and not the full network. The advantage of using electrons instead of photons is the larger control to prepare non-classical by gates and the larger quantity of electrons available in solid state structures. The unique properties of graphene, especially the ballistic transport will allow to reduce the destructive decoherence mechanisms which are otherwise considerably stronger than for photons. With these essentials, it seems promising to investigate the use of electrons in graphene for quantum information processing.

In a bit more detail in our new scheme, position and momentum of the electrons injected by an Ohmic contact and propagating in the low-dimensional structure such as graphene may be modelled by Gaussian thermal distributions. Gaussian states are treated routinely within the framework of quantum information (QI) with continuous variables (7). The basis of our proposed QI scheme is to use a beam splitter to generate entanglement between the two output states, which has been shown to work as an entangler if Gaussian states are provided at the inputs of the beam splitter (8). One can see the position of each electron exiting the beam splitter and its choice of the two output paths to form the qubit of information.

In addition the operation of a 50/50 beam splitter can be interpreted in a more computational formalism as the realisation of a Hadamard gate which is one of the fundamental logic gates required for quantum computation. This interpretation of beam splitter operations as quantum gate operations is the same as in quantum computation with linear optics (9). While the framework of continuous variables

for quantum information and the use of linear optics components is solid for photons, it still needs further development for our case of electrons in low-dimensional materials. The experiments performed in this thesis aim to make a very first step in aiming to realise a beam splitter for electrons in graphene, which may then motivate more intense research, theoretically and experimentally, towards a full quantum information architecture based on continuous variables.

1.1 Graphene's Band Structure

Electricity is conducted in solids by the transport of charged particles called electrons. The characteristics of this transport are determined by the interaction of the electrons with the solid through which it is travelling. In a crystalline solid the recurring patterns of structure within the solid material influence the electron transport properties by determining the bandstructure in which the electrons can travel. Solids are generally split into three different categories depending on their bandstructure: conductors, insulators and semiconductors. In insulators the electrons have no bands in which they can travel. In conductors the intrinsic electron energy (Fermi Energy) resides inside the band allowing conduction and in semiconductors their energy rests close to a band which makes them insulators until their energy is changed to bring it into a conduction band at which point they become conducting. Graphene's band structure does not directly fit into any of these three categories however; the conduction and valence bands both diminish linearly as they approach each other forming a single point known as a Dirac point. (10) In undoped graphene the Fermi energy lies at the Dirac point. Although the Fermi energy is not within a band, there is no "gap" of defined energy which has to be overcome to produce conduction. Due to this graphene is best described as a semi-metal as shown in Figure 1.1.

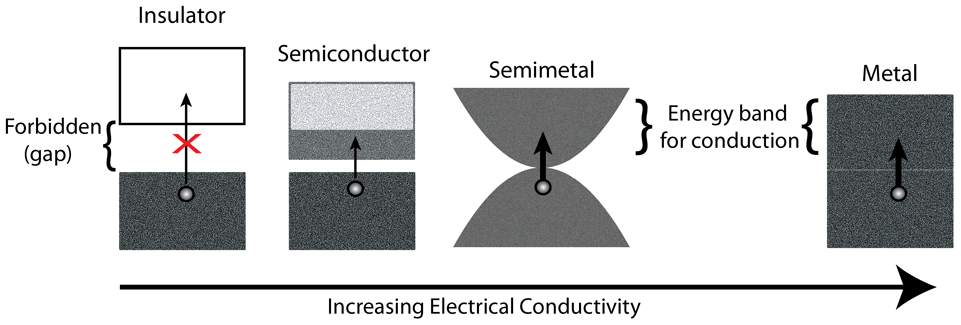

Figure 1.1: A comparison of the bandstructure of insulators, semiconductors, semimetals and metals. (11)

The next point to note about graphene's bandstructure, and one which has caused much of the hype surrounding graphene is the linear dispersion. Figure 1.2 shows the whole bandstructure of an isolated sheet of graphene and on the inset is a zoomed in look at the Fermi level at one of the K points. It shows that there is a linear relationship between the wavevectors and the energy. This is unusual when compared to semiconductors and is a defining feature which is governed by the underlying physics. In a semiconductor the dispersion is usually parabolic (12) as the energy, ε and wavevector, k_F are related by:

$$\varepsilon(\boldsymbol{k_F}) = \varepsilon(0) + \frac{\hbar^2 k_F^2}{2m^*} \tag{1.1}$$

Where m^* is the effective mass of the electron and $\hbar$ is the reduced Planck constant.

In contrast for monolayer graphene the dispersion relation is given by:

$$\varepsilon(\boldsymbol{k_F}) = \hbar V_F \boldsymbol{k_F} \tag{1.2}$$

Where V_F is the Fermi velocity. (13)

Given that the velocity is calculated from the dispersion relation via:

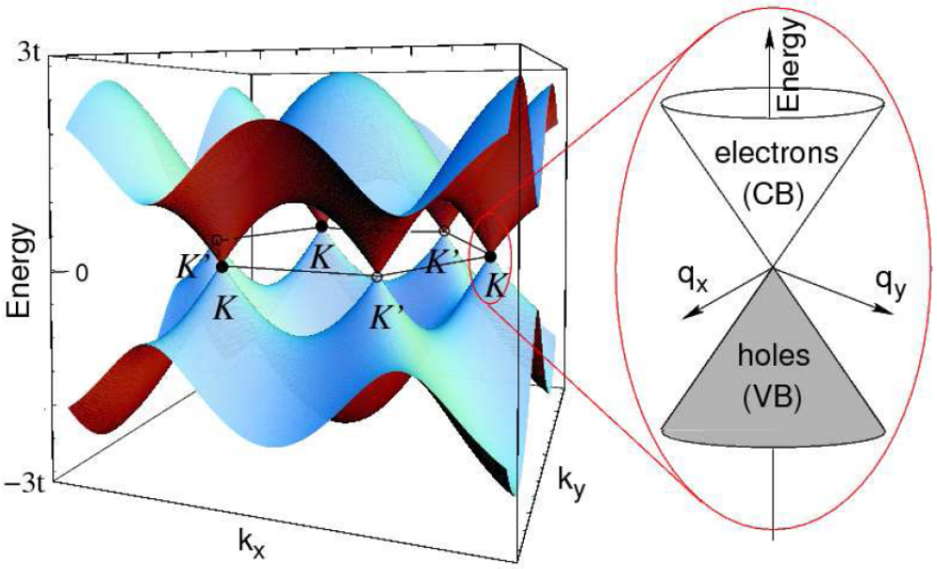

Figure 1.2: The bandstructure of Graphene and, inset, the K point where the dispersion is linear close to the Fermi energy. (14)

$$\boldsymbol{V_{group}} = \frac{1}{\hbar}\frac{d\varepsilon(\boldsymbol{k_F})}{d\boldsymbol{k_F}} \tag{1.3}$$

It is easy to see that for graphene the velocity of the electrons is given by:

$$\boldsymbol{V} = V_F\frac{\boldsymbol{k_F}}{k_F} \tag{1.4}$$

This has been found to be somewhere in the region of $c/300 = 1 \times 10^6 ms^{-1}$, quite a significant speed indeed, but we should remember that this is the velocity of the charge carriers between their collisions. The average velocity of the charge carriers can only approach this large value as we remove the impurities and imperfections in the system which are causing the scattering collisions. Chapters 3.3 and 3.4 discuss ways in which to reduce these scattering sites and approach a physical representation of the perfect graphene sheet.

There are four valence electrons per Carbon atom, three of which are used for the

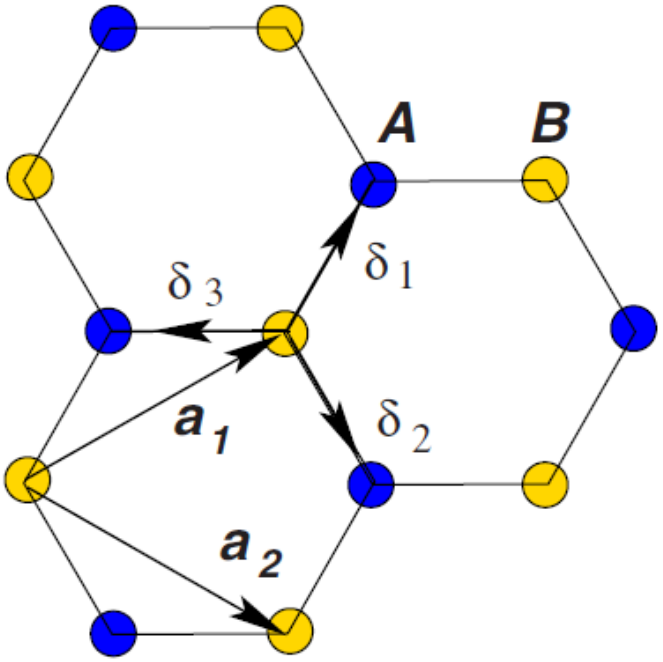

Figure 1.3: The honeycomb lattice structure of graphene. Two triangular lattices, represented by blue and yellow circles, make up the hexagonal structure. The two primitive lattice vectors are labeled a_1 and a_2. The nearest neighbour vectors are marked as δ_1, δ_2 and δ_3. (10)

sp^2 bonds. The fourth electron is in a p_z orbital and forms the π band. As there are two of these p_z electrons per unit-cell there are two π bands known as π and π^*. The primitive lattice vectors, shown in Figure 1.3, are $a_1 = \frac{a_0}{2}\left(3, \sqrt{3}\right)$ and $a_2 = \frac{a_0}{2}\left(3, -\sqrt{3}\right)$ in the Cartesian basis where a_0 is the distance between nearest neighbours, which for the hexagonal carbon lattice is 1.42Å.

The reciprocal lattice vectors, shown on the reciprocal lattice in Figure 1.4, are given by $b_1 = \frac{2\pi}{3a}\left(1, \sqrt{3}\right)$ and $b_2 = \frac{2\pi}{3a}\left(1, -\sqrt{3}\right)$.

To look at the tight binding model for graphene we must first look at the energy eigenstates in crystalline structures (15). Bloch's theorem states that energy eigenstates for electrons in a crystal can be written as Bloch waves. Bloch waves

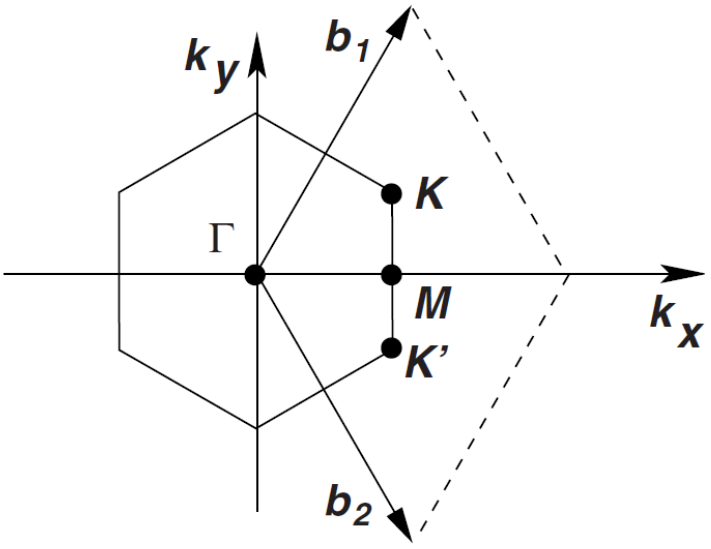

Figure 1.4: The reciprocal lattice of graphene with the reciprocal primitive lattice vectors, b_1 and b_2. The two non equivilant K points are labeled K and K'. (10)

are described by:

$$\psi_{n\vec{k}}\left(\vec{r}+\vec{R}\right)=e^{ik.\vec{R}}u\left(\vec{r}\right) \tag{1.5}$$

Where $\vec{r}$ is position, $\vec{R}$ is a real space translation vector of the crystal, $\vec{k}$ is the wavevector and u is a periodic function with the same period as the crystal.

We can make a linear combination of atomic orbitals on N lattice sites:

$$\psi_{n\vec{k}}\left(\vec{r}\right)=\frac{1}{\sqrt{N}}\sum Re^{ik.\vec{R}}\phi\left(\vec{r}\right) \tag{1.6}$$

The Ansatz to start with for the wavefunction is: (16)

$$\psi_{\vec{k}} = \sum_{\vec{R}\epsilon G} e^{i\vec{k}.\vec{R}} \phi\left(\vec{x} - \vec{R}\right) \tag{1.7}$$

Where G is the set of lattice vectors and $\phi\left(\vec{x}\right)$ are the atomic wavefunctions of the p_z orbitals. There are two p_z orbitals per unit cell with wavefunctions ϕ_1 and ϕ_2; one for each carbon atom. The tight binding approximation assumes that these wavefunctions are localised at the position of the atom. (17). A linear combination of these two wavefunctions gives the total wavefunction ϕ:

$$\phi\left(\vec{x}\right) = b_1\phi_1\left(\vec{x}\right) + b_2\phi_2\left(\vec{x}\right) = \sum_n b_n\phi_n \tag{1.8}$$

Where the subscripts 1 and 2 represent the two atoms in the unit-cell.

We set up the Hamiltonian of the system:

$$H = \frac{p^2}{2m} + \sum_{\vec{R}\epsilon G}\left(V_{at}\left(\vec{x} - \vec{x_1} - \vec{R}\right) + V_{at}\left(\vec{x} - \vec{x_2} - \vec{R}\right)\right) \tag{1.9}$$

$x_{1,2}$ denote the position of the two carbon atoms within the unit cell. We next need to solve the Schrödinger equation.

$$H\psi_k = E\left(\vec{k}\right)\psi_k \tag{1.10}$$

Since there are two parameters, b_1 and b_2, two equations are required and we find them by projecting $\psi_{\vec{k}}$ onto the two states ϕ_1 and ϕ_2.

$$E\left(\vec{k}\right)\langle\phi_j|\psi\rangle = \langle\phi_j|\Delta U_j|\psi\rangle \tag{1.11}$$

$$H\phi_1 = \Delta U_1 \phi_1 \tag{1.12}$$

$$H\phi_2 = \Delta U_2 \phi_2 \tag{1.13}$$

$$\Delta U_j = V_{at}\left(\vec{x} - \vec{x_j} - \vec{R}\right) \tag{1.14}$$

Now we can calculate $\langle\phi_1|\psi\rangle$ and $\langle\phi_2|\psi\rangle$.

$$\langle\phi_1|\psi\rangle = b_1 + b_2\left(\int \phi_1^* \phi_2\right)\left(1 + e^{-i\vec{k}.\vec{a_1}} + e^{-i\vec{k}.\vec{a_2}}\right) \tag{1.15}$$

$$\langle\phi_2|\psi\rangle = b_2 + b_1\left(\int \phi_2^* \phi_1\right)\left(1 + e^{i\vec{k}.\vec{a_1}} + e^{i\vec{k}.\vec{a_2}}\right) \tag{1.16}$$

We can define $\gamma_0 = \int \phi_1^* \phi_2 = \int \phi_2^* \phi_1$, $\alpha = 1 + e^{-i\vec{k}.\vec{a_1}} + e^{-i\vec{k}.\vec{a_2}}$ and $\alpha^* = 1 + e^{i\vec{k}.\vec{a_1}} + e^{i\vec{k}.\vec{a_2}}$. Next we can calculate $\langle\phi_1|\Delta U_1|\phi\rangle$ and $\langle\phi_2|\Delta U_2|\phi\rangle$:

$$\langle\phi_1|\Delta U_1|\phi\rangle = b_2\gamma_1\left(1 + e^{-i\vec{k}.\vec{a_1}} + e^{-i\vec{k}.\vec{a_2}}\right) \tag{1.17}$$

$$\langle\phi_2|\Delta U_2|\phi\rangle = b_1\gamma_2\left(1 + e^{i\vec{k}.\vec{a_1}} + e^{i\vec{k}.\vec{a_2}}\right) \tag{1.18}$$

Now we can use these results with Equation 1.11 to find the two simultaneous equations:

$$E\left(\vec{k}\right) b_1 + \alpha b_2 \left(\gamma_0 E\left(\vec{k}\right) - \gamma_1\right) = 0 \tag{1.19}$$

$$E\left(\vec{k}\right) b_2 + \alpha^* b_1 \left(\gamma_0 E\left(\vec{k}\right) - \gamma_1\right) = 0 \tag{1.20}$$

To find $E\left(\vec{k}\right)$ we can construct a matrix, M:

$$\begin{pmatrix} E\left(\vec{k}\right) & \alpha\left(\gamma_0 E\left(\vec{k}\right) - \gamma_1\right) \\ \alpha^*\left(\gamma_0 E\left(\vec{k}\right) - \gamma_1\right) & E\left(\vec{k}\right) \end{pmatrix} \begin{pmatrix} b_1 \\ b_2 \end{pmatrix} = 0 \tag{1.21}$$

Solving for the determinant $det\left[M\right] = 0$ and solving the resultant quadratic equation we find that the dispersion relation, $E\left(\vec{k}\right)$ is: (18)

$$E\left(\vec{k}\right) = E_F \pm \gamma_0 \sqrt{1 + 4\cos\left(\frac{\sqrt{3}k_x a}{2}\right)\cos\left(\frac{k_y a}{2}\right) + 4\cos^2\left(\frac{k_y a}{2}\right)} \tag{1.22}$$

This bandstructure is shown in Figure 1.2. The K and K' points can be seen where the two bands meet. The inset of Figure 1.2 shows the bandstructure close to the K and K' points which is conical in shape and the dispersion close to the Fermi energy is linear.

If we look at the energy dispersion around the K and K' points we can find the low energy properties near the Fermi energy. We can set the wave vector for the valley K as $q = K + k$ where $|k| << 1$ and then we will find that:

$$E\left(q\right) \approx \pm\hbar v_F |k| \tag{1.23}$$

Where the Fermi velocity, $v_F = \frac{3a|\gamma_0|}{2h} \approx 1 \times 10^6 ms^{-1}$. The K' points have the same result.

Because of the linear dispersion relation we can draw many similarities between charge carriers in graphene and photons. The energy of a photon is given by $E(k) = \hbar ck$ which is remarkably similar to Equation 1.23. As our usual method of determining the effective mass in crytalline structures, m^*, of particles assumes a parabolic dispersion it thus diverges when given a linear dispersion. This leads to some confusion with the carriers in graphene often described as "massless".

$$m^* = \hbar^2 \left(\frac{d^2 E(k)}{dk^2} \right)^{-1} \tag{1.24}$$

For a more appropriate method of finding the effective mass of the electron we start by defining the momentum of the particle:

$$p = \hbar k = m^* v_g \tag{1.25}$$

Where v_g is the group velocity given by:

$$v_g = \frac{1}{\hbar} \frac{dE(k)}{dk} \tag{1.26}$$

Combining these two equations gives an alternative definition of the effective mass:

$$m^* = \hbar^2 k \left(\frac{dE(k)}{dk} \right)^{-1} \tag{1.27}$$

When we apply this to the dispersion relation of graphene we get for the effective mass of charge carriers:

$$m^* = \frac{\hbar k}{v_F} \tag{1.28}$$

For nearly massless particles we do not usually describe them using the Schrödinger equation but instead use the Dirac equation. To look at that we can expand the Hamiltonian around the K and K' points, that is at $q = K + k$:

$$H(q) = \begin{pmatrix} E(q) & \gamma_0 \alpha_q \\ \gamma_0 \alpha_q^* & E(q) \end{pmatrix} \tag{1.29}$$

Where α_q and α_q^* are the same as α and α^* defined above except that k is substituted with q. Evaluating this Hamiltonian in the vicinity of the K point yields:

$$H_K^0(k) = \hbar v_F \begin{pmatrix} 0 & i(k_x - ik_y) \\ -i(k_x + ik_y) & 0 \end{pmatrix} = \hbar v_F \vec{\sigma} \cdot \vec{k} \tag{1.30}$$

Where $\vec{\sigma} = (\sigma_x, \sigma_y)$ are the Pauli matrices.

The eigenvectors for the momentum around K is:

$$\Psi_{\pm,K}(k) = \frac{1}{\sqrt{2}} \begin{pmatrix} e^{-i\theta_k/2} \\ \pm e^{i\theta_k/2} \end{pmatrix} \tag{1.31}$$

The eigenvalues are $E = \pm \hbar v_F k_F$ where the $\pm$ denotes the π^* or π band respectively.

Around the K' point the momentum wavefunction is:

$$\Psi_{\pm,K'}(k) = \frac{1}{\sqrt{2}} \begin{pmatrix} e^{i\theta_k/2} \\ \pm e^{-i\theta_k/2} \end{pmatrix} \tag{1.32}$$

and the Hamiltonian is:

$$H^0_{K'}(k) = \hbar v_F \vec{\sigma^*} \cdot \vec{k} \tag{1.33}$$

Where $\vec{\sigma^*} = (\sigma_x, -\sigma_y)$.

We can define the helicity of the eigenfunctions as the projection of the momentum along the pseudospin direction (10). The operator, $\hat{h}$, for the helicity is given by:

$$\hat{h} = \frac{1}{2}\vec{\sigma} \cdot \frac{\vec{p}}{|\vec{p}|} \tag{1.34}$$

We can see that the states $\Psi_K(r)$ and $\Psi_{K'}(r)$ are eigenstates of $\hat{h}$:

$$\hat{h}\Psi_K(r) = \pm\frac{1}{2}\Psi_K(r) \tag{1.35}$$

$$\hat{h}\Psi_{K'}(r) = \mp\frac{1}{2}\Psi_{K'}(r) \tag{1.36}$$

Electrons in graphene have a positive helicity and holes have a negative helicity. Equation 1.35 implies that $\vec{\sigma}$ has its two eigenvalues aligned either with the direction of the momentum, $\vec{p}$, or against it. We should be careful to note that this helicity is not associated with the real spin of the electron, but the pseudospin is a further quantum number which is only reliant on these two properties of the wavefunction.

1.1.1 Landau Levels

It is interesting to look at the way electrons in graphene behave when subjected to a magnetic field. Let us then describe a plane of graphene with lengths L_x and L_y in the x and y directions and a magnetic field acting perpendicular to the plane in the z direction. What results is a quantisation of cyclotron orbits of the charged particles. The charge carriers can only occupy orbits with discrete energy values which are known as Landau levels. The degeneracy of these levels means that a large number of charged particles can occupy each level and the occupancy of the levels is dependant on the magnetic field. Let us assume that we have q non-interacting charged particles with spin S in an area $A = L_x L_y$ and we apply our magnetic field B in the z direction:

$$B = \begin{pmatrix} 0 \\ 0 \\ B \end{pmatrix} \tag{1.37}$$

The Hamiltonian we will use is:

$$H = \frac{1}{2m^*}\left(\hat{p} - \frac{q\hat{A}}{c}\right)^2 \tag{1.38}$$

Where $\hat{p}$ is the momentum operator and $\hat{A}$ is the electromagnetic vector potential given by $B = \bigtriangledown \times \hat{A}$.

For simplicity we use the Landau gauge where $\hat{A} = \begin{pmatrix} 0 \\ Bx \\ 0 \end{pmatrix}$. Now the Hamiltonian is given by:

$$\hat{H} = \frac{\hat{p}_x^2}{2m^*} + \frac{1}{2m^*}\left(\hat{p}_y - \frac{qB\hat{x}}{c}\right)^2 \tag{1.39}$$

Due to our choice of gauge the $\hat{p}_y$ operator commutes with this Hamiltonian and it can therefore be replaced by its eigenvalue $\hbar k_y$. Now we use the definition of the cyclotron frequency $\omega_c = qB/m^*c$ and the Hamiltonian is now:

$$\hat{H} = \frac{\hat{p}_x^2}{2m^*} + \frac{1}{2}m^*\omega_c^2\left(\hat{x} - \frac{\hbar k_y}{m^*\omega_c}\right)^2 \tag{1.40}$$

This is very similar to the Hamiltonian for the quantum harmonic oscillator but with a potential shift of $x_0 = \hbar k_y/m^*\omega_c$.

The energy levels, E_n of this system are thus given by:

$$E_n = \hbar\omega_c\left(n + \frac{1}{2}\right), n \geq 0 \tag{1.41}$$

The degeneracies mentioned earlier appear due to the fact that the energy of the system does not depend on the quantum number k_y.

1.2 Quantum Optics of Electrons

The Hanbury Brown and Twiss experiment uses time averaged intensity correlations. However a stream of particles will have a varying intensity around its mean value due to shot noise (19). Shot noise is an intrinsic characteristic of a stream of particles due to their discrete nature. When combining two indistinguishable streams of degenerate fermions (e.g. electrons) the shot noise can be partially suppressed due to the Pauli Exclusion principle which is a purely quantum effect. (20)

For classical particles, we would say that they are distinguishable and that given enough processing power and or time we could calculate and predict the future positions, velocities or energies of the particles. However for quantum particles it is usually the case that we cannot distinguish between them and that each individual quantum particle of a particular species or type is identical. We use wavefunctions to describe them and to deal with the indistinguishability we can make predictions which map out the probabilities of a particle starting in one state and ending in another.

For fermions which are anti-symmetric, when we exchange one particle for another, as we can do with indistinguishable particles, we use equation 1.42.

$$|n_1, n_2\rangle = \frac{1}{\sqrt{2}} \left(|n_1\rangle |n_2\rangle - |n_2\rangle |n_1\rangle \right) \tag{1.42}$$

As we can see, if we have particles which are identical and in the same state, that is $n_1 = n_2$, then we get zero which cannot be a state vector. This means that two fermions cannot occupy the same single-particle state, which is known as the Pauli exclusion principle.

Equation 1.43 gives the probability of finding an electron at a particular energy given the temperature and Fermi level of the system.

$$\overline{n_i(\epsilon_i)} = \frac{1}{e^{(\epsilon_i - \mu)/kT} + 1} \tag{1.43}$$

Where T is the temperature, k is Boltzmann's constant ϵ_i is the energy of the single particle state i and μ is the total chemical potential. This is the Fermi-Dirac distribution. At a temperature of $0K$ all of the electrons have an energy equal to or less than the Fermi level. As we move to finite temperatures there is a spread in the energy levels of the electrons which is centred around the Fermi

level, this means that at higher temperatures we are less certain about the energy of the electrons which are involved in the charge transport. Careful control of the temperature is required in order to have full control of the system as this spread could easily allow an electron to traverse a barrier which it might not otherwise be able. For a given temperature in a thermal reservoir the average particle number, $\hat{N}_k = \hat{a}_k^\dagger \hat{a}_k$, for a single mode k at an energy ϵ_k is:

$$\left\langle \hat{N}_k \right\rangle = n_i(\epsilon_k) \tag{1.44}$$

The variance of this gives us a look at the fluctuations in the occupation of this particle number, this is given by:

$$\left\langle \left[\Delta \hat{N}_k\right]^2 \right\rangle = \left\langle \hat{N}_k \right\rangle \left(1 - \left\langle \hat{N}_k \right\rangle\right) \tag{1.45}$$

$$F = \frac{\left\langle \left[\Delta \hat{N}_k\right]^2 \right\rangle}{\left\langle \hat{N}_k \right\rangle} = \begin{cases} > 1 & \text{Boson super-Poisson} \\ 1 & \text{Classical Poisson} \\ < 1 & \text{Fermion sub-Poisson} \end{cases} \tag{1.46}$$

Photons are bosons and obey Bose-Einstein statistics, whereas electrons are fermions which obey Fermi-Dirac statistics. Photons from a thermal source have a super-Poisson distribution which means that they tend to bunch together and therefore the time variance of particle arrival is larger than the mean. Electrons on the other hand tend not to bunch, but rather spread out which means that the variance is smaller than the mean; they have sub-Poisson distributions.

This difference can be shown very nicely by the Hong Ou Mandel effect (21). Initially performed with photons the interference experiment works by combining

two photon sources with a 50 : 50 beam splitter and measuring the coincidence rates of the two outputs of the beam splitter whilst varying a delay between the sources. When two indistinguishable photons arrive at the beam splitter at the same time they tend to bunch and take the same path to the same output path. This leads to the coincidence rates decreasing and a dip is seen in the coincidence rates as the delay brings about a match of the arrival times of the photons at the beam splitter. The dip reaches zero when the photons are arriving at the exact same time and are completely indistinguishable. This gives a measure of the similarity or difference between two light sources.

In contrast for electrons when two electron sources are combined with a beam splitter, they will tend not to take the same output path, rather they start to take a path each. This is called anti-bunching (22).

1.3 Graphene Electronics

Although graphene has been touted for its multiple exceptional qualities, including mechanical strength (23), thermal conductivity (24) and impermeability (25) its true promise lies with the distinctive and unusual electrical properties. The inaugural graphene paper from Novoselov and Geim (26) was published in 2004 and already within one year other groups were able to produce their own flakes, electrically contact them and show the quantum hall effect in graphene (27). Soon after the fractional hall effect was reported (28). Owing to graphene's unusual bandstructure, which allows the tabletop experimental observation of many high energy physics phenomena, the field of research into the graphene electronic devices is vast and moving at a very fast pace. By using local gates to define areas of different electric field within the 2D plane of the graphene sheet, many new

devices could be envisaged each tuned to explore a different effect. An early example of a 2D potential landscape in graphene is the work by Williams et al (29). Their device was a PN junction formed by a topgate covering half of the graphene flake, separated from the graphene by a layer of Al_2O_3 roughly $30nm$ thick. They were able to look at the quantum Hall effect in the PN junction and showed clear plateaus relating to the presence of Landau levels. They were able to investigate the effects of switching both the direction of the magnetic field and the carrier charge as it is assumed that both holes and electrons are involved in the charge transport in PN junctions. Taychatanapat and Jarillo-Herrero looked at transport through a PNP with bilayer graphene (30). Their devices also utilised a layer of Al_2O_3 deposited on the surface of the graphene bilayer to form a dielectric which allows the formation of a topgate which influences only a local area. This arrangement allowed the PNP barrier to be explored in the bilayer graphene flake. A transport gap was found, however it was only sustained at very low temperatures due to the coulomb interactions from the materials in contact with the graphene.

Dean et al showed that the mobility of graphene devices could be dramatically improved by using hexagonal boron nitride (hBN) as a substrate for the graphene flakes (31); they tripled the mobility of their samples from $\sim 20,000\ cm^2V^{-1}s^{-1}$ to $\sim 60,000\ cm^2V^{-1}s^{-1}$. Mayorov et al demonstrated ballistic transport at room temperature by encapsulating the graphene in hexagonal boron nitride (32). They found that by sandwiching the graphene flake in between two flakes of hBN they had a mean free path of $l = 3\mu m$ which was longer than the device dimensions they could achieve. They were limited in the device dimensions by bubbles in the layers of the hBN-graphene-hBN stack, which meant that they had to define the device on the flat sections between the bubbles. Wang et al showed that it is possible to contact the graphene sheet by its edge to form a one dimensional contact (33). This changed the required steps in fabrication of the hBN-graphene-hBN sandwich which allowed the stack to be formed without introducing the

surface of the graphene to any dissolved PMMA or other contaminants. Using this new dry transfer technique and contacting the edge of their sample they were able to achieve devices with mean free path as large as $l = 15\mu m$. Once again the upper limit on the mean free path was found to be the physical dimensions of the device.

1.4 Quantum Transport

Transport of charged particles (electrons or holes) through nanostructured devices is largely different to the transport of the charges though a bulk medium. Scattering of charges dominates the transport characteristics in bulk materials and it is this which gives rise to classical electrical resistance. In nanostructured devices it is possible to have a mean free path which is many times longer than the device. This can lead to ballistic transport in which the charges do not scatter as they traverse the device. Ballistic transport is necessary for quantum interferometry of electrons as scattering of the electrons can cause random phase shifts, this reduces or in the worst case eliminates the visibility of quantum interference.

Length scales:

- Device length: L, the distance between two ohmic contacts between which the conduction flows.
- Fermi Wavelength: λ_F, only the electrons at near the Fermi level contribute to the conduction
- Mean free path: l_m, also known as the momentum relaxation length it is the average distance an electron can move before a collision which changes its momentum. This is dominated by static scatterers.

- Phase relaxation length: l_ϕ, the average distance an electron moves before the information in its phase is lost by unpredictable phase jumps or changes. This is most affected by dynamic scatterers.
- De Broglie wavelength: λ_{dB}, related to the kinetic energy of the electron by $\lambda_{dB} = \frac{h}{p} = \frac{h}{m^* v}$.

These length scales will dictate the regime which dominates the electron transport in a nanostructured device. The possible regimes are:

- Classical incoherent transport: $L >> l_m$ & l_ϕ.
- Localisation: $l_m << l_\phi << L$. Phase coherent transport can lead to universal conduction fluctuations.
- Diffuse: $L > l_m$, scattering is occurring increasing resistance and slowing transport down.
- Ballistic: $L << l_m$ & l_ϕ, no scattering is occurring in the device between ohmic contacts. Quantised conduction is possible.

If a device has dimensions which are smaller than the mean free path and the phase relaxation length then this enables some interesting experiments which can probe the wave like nature of electrons as in Young's double slits or their quantum statistical nature as in Hong Ou Mandel.

Electrons within an applied electric field **E** experience a force e**E** which causes a drift velocity v_d. When the system is in a steady state the change in momentum due to the force is equal to the change in momentum due to the scattering as in equation 1.47 (34)

$$\left[\frac{d\mathbf{p}}{dt}\right]_{scattering} = \left[\frac{d\mathbf{p}}{dt}\right]_{field} \tag{1.47}$$

This gives:

$$\frac{m^* v_d}{\tau_m} = e\mathbf{E}$$

Where τ_m is the momentum relaxation time and m^* is the effective mass of the electron and therefore:

$$v_d = \frac{e\tau_m}{m^*}\mathbf{E}$$

Mobility μ is defined as the ratio of the drift velocity to the electric field as in equation 1.48:

$$\mu = \left|\frac{v_d}{\mathbf{E}}\right| = \frac{|e|\,\tau_m}{m^*} \tag{1.48}$$

The mean free path, l_m, is related to the Fermi velocity, v_f, and the momentum relaxation time, τ_m, as in equation 1.49:

$$l_m = v_f \tau_m \tag{1.49}$$

At low temperatures the only electrons which contribute to the conductance are the ones at the Fermi level hence Fermi velocity, v_f, is the correct term to use.

From equations 1.48 and 1.49 it is seen that:

$$l_m = \frac{v_f \mu m^*}{|e|} \tag{1.50}$$

Where m^* is the effective mass of the electron. In graphene it has been found that

v_f is constant at $v_f = 10^6 ms^{-1}$ and with m^* and e constant it is easy to see that the mobility, which is easily measured, gives us a direct method to find the mean free path within devices.

To measure the mobility of a graphene device, a constant source-drain voltage is applied across the flake and the global backgate voltage is varied to record the conductivity of the device as the charge carrier density is swept.

Conductivity, σ, in a two dimensional conductor such as graphene is defined as in Equation 1.51.

$$\sigma = \frac{IL}{VW} \tag{1.51}$$

Where I is the current, V is the voltage, W is the width and L is the length of the graphene flake between the ohmic contacts. (12)

Resistivity, ρ, is the inverse of conductivity:

$$\rho = 1/\sigma \tag{1.52}$$

Equation 1.53 shows how the charge carrier density, n, is related to the capacitive coupling, C, between the backgate and the graphene flake and the voltage, V, applied to the backgate relative to the voltage at the Dirac point, V_d.

$$n = C\left(V - V_d\right)/e \tag{1.53}$$

The mobility, μ, is then found using the relationship shown in 1.54 between the charge carrier density, n, the

$$\mu = 1/ne\rho \tag{1.54}$$

It has been found that the mobility of graphene samples is highly affected by the substrate on which the sample is placed. The most popular substrate used is SiO_2 at a thickness of $300nm$. This is used because it allows the graphene flakes to be found under an optical microscope due to a contrast which is caused by interference at the interfaces.

It has been shown that the SiO_2 substrate causes impurity scattering sites which unlike phonon scattering cannot be suppressed by low temperatures. The surface roughness of the SiO_2 substrate combined with trapped charges make it very difficult to fabricate devices which utilise the full potential of graphene as an electrical conductor.

The mobility of device "S9" which is described in Section 3.10.2 is $25,000cm^2V^{-1}s^{-1}$ when measured at room temperature, this allows a mean free path of 340 nm.

Consideration has been made to make changes to the substrate in order to maximise the mobility of the samples. The simplest, although still technically challenging, is to remove the substrate all together by suspending the graphene. This can be achieved by first placing two or more metal contacts on the graphene flake and then exposing the sample to Hydrofluoric acid (HF), this removes the SiO_2 both around and beneath the graphene but not beneath the metal contacts. Thus the graphene flake becomes a suspended doubly clamped bridge between the metal contacts.

Mobilities as high as $200,000cm^2V^{-1}s^{-1}$ have been found in suspended graphene devices. (35) This equates to a mean free path of $3.4\mu m$ which gives plenty of space for device fabrication with current technologies. However suspended samples would prove very challenging to add local gates and are not suitable for carving

as any carved features would require a support otherwise the graphene will roll up into a scroll. Adding these supports would obviously negate the benefits of suspending the graphene.

A new method for suspending graphene flakes has been discovered and developed by modifying a method which is used to transfer graphene flakes between substrates. It is found that graphene flakes can be transferred onto a substrate which has been prepared with metal contacts with an appropriate sized gap between them according to the size of the graphene flake. The flake can be transferred with sufficient accuracy such that it rests on the metal contacts and forms a suspended bridge between the contacts without being clamped. This method removes the need to use dangerous substances such as HF.

Recently it has been found that hexagonal Boron Nitride (hBN) is an ideal candidate as a better substrate for graphene devices. hBN has a very similar crystalline structure to graphene, with the carbon atoms replaced with alternating boron and nitrogen atoms. Its has a lattice mismatch with graphene of less than 2% and is electrically insulating and thus it is an atomically flat insulating substrate. It is thought that these properties are responsible for reports of mobilities as high as $500,000 cm^2 V^{-1} s^{-1}$ in graphene samples which are sandwiched between hBN flakes. (32).

Using the above mentioned transfer method it has been possible to place flakes of graphene on to selected flakes of hBN and then contact them for electrical measurements.

1.5 Veselago, Klein & Ballistic Transport

As shown by Cheianov et al (36), using the work previously published by Veselago (37), graphene devices should be able to exhibit the property of negative refraction by using appropriate local gates to control the electrostatic landscape of the graphene device. This speculative control requires that there are no scattering sites within the devices as these would diminish any lensing or reflective effects. As such ballistic transport of the electrons within the graphene device is a requirement.

In order to achieve ballistic transport in graphene devices it is required that the mean free path between collisions be larger than the dimensions of the device. The charge carrier mobility is an excellent indicator of mean free path for a given device. This presents practical challenges in the fabrication and design of the graphene devices. It has been found that the SiO_2 substrate, which was very commonly used in early production of graphene devices, causes a large number of scattering sites which lead to a decreased mobility and thus decreased mean free path when compared to a free standing or unperturbed system (31). However if local gates are to be used then free standing graphene is not practical, Mayorov et al (32) use hexagonal boron nitride as a substrate as it provides a smoother surface onto which the graphene can be placed. This smoothness removes the scattering sites present in SiO_2 substrate, however it can lead to bubbles under the transferred graphene flake, which then cause the high degree of scattering to return (38). A method is found to remove the bubbles and produce flat sections of graphene on hBN large enough to fabricate the proposed devices. Further, a dry transfer technique which was reported by Wang et al (33) including a method to electrically contact the pristine graphene layer was incorporated in the fabrication of the latest devices. This allows the graphene to be contacted at the edges whilst protecting the graphene layer from contaminants. It has the added benefit of leaving a high

quality dielectric on the top of the device which can be used to attach a top gate to, allowing a potential landscape to be created and controlled in the 2-D plane of the graphene flake. The use of top gates to define the structure of the devices is necessary as carving the structure by removal of material was found to introduce unwanted scattering sites due to the uncontrolled chemical terminations at the edges.

Cheianov et al (39) showed that in fact the electrons incident on a PN junction in graphene exhibit an effect similar to that described by Klein (40) known as Klein tunnelling; this is discussed in Chapter 2.2. The transmission of electrons through the PN junction is a function of their angle of incidence, Chapter 2.4.1 describes this phenomenon.

By simulating negative refraction and also the subsequent Fabry-Perot like angular transmission probability, experiments can be designed towards a ballistic interferometer for electrons in graphene analogous to already used systems in quantum optics.

1.6 Split Path Interferometer

By combining the negative refraction effect with the selective angular transmission a device could be envisioned which allows the electrons to travel along two physically separated paths which then recombine at the drain. By introducing a phase delay into one of the paths relative to the other an interference of electrons which travel down the separate paths should be possible.

A phase delay can be introduced into one of the arms of the Split Path Interferometer by two methods: using the Aharonov Bohm effect as the two paths form a closed loop through which a magnetic flux can pass or by locally modifying the

wavelength of the electron in one of the arms using thin top gates to form $PP'P$ or $NN'N$ barriers in the electron path. $PP'P$ and $NN'N$ barriers as shown in Figure 2.7 are formed of three regions all of which have electrical potential energy which sits on the same side of the Dirac point but the middle region has a different potential to the outer two. Section 2.4.3 describes such barriers in further detail. Devices are fabricated which test the negative refraction effect in graphene and then along with the angular dependant transmission of a PNP barrier form a split path interferometer. An alternative device configuration is suggested which uses the PNP barriers as collimators, 50/50 beam splitters and mirrors by tuning the potential of the gates.

1.7 Quantum Computing

Classical computational devices as are common in the world around us at present operate using a two state system, usually represented by 0s and 1s. That is to say that a bit in a classical computer can be either 0 or 1. They are deterministic in their nature and can be formed by any system with a finite set of discrete stable states. Quantum mechanics however allows a superposition of states; a quantum bit or qubit in a quantum computer is described by:

$$\alpha \left|0\right\rangle + \beta \left|1\right\rangle \tag{1.55}$$

Where α and β are complex numbers satisfying:

$$|\alpha|^2 + |\beta|^2 = 1 \tag{1.56}$$

The probability of measuring the state $|0\rangle$ is $|\alpha|^2$ and $|1\rangle$ has a probability of

$|\beta|^2$. After a measurement the system is in the measured state and any further measurements will yield the same result until the system is reset or manipulated into a mixed state once more.

1.7.1 Quantum Gates

We use gates to manipulate bits and facilitate a calculation to be made. Some basic gates which are used in classical computers are the AND, OR and NOT gates. These gates test the conditions of one or more inputs and give an output depending on some logic performed on those inputs as shown below.

AND Gate

Input 1	Input 2	Output
1	1	1
1	0	0
0	1	0
0	0	0

OR Gate

Input 1	Input 2	Output
1	1	1
1	0	1
0	1	1
0	0	0

NOT Gate

Input	Output
1	0
0	1

As a qubit comprises of a probability of being one or the other of the two states possible and is not a defined value until measured the gates used in quantum computing act on both states simultaneously. The Pauli gates, X, Y and Z, show how

these differ from classical gates. Quantum gates can be represented by transformation matrices. Here I will use the basis:

$$\begin{bmatrix} |0\rangle \\ |1\rangle \end{bmatrix} \tag{1.57}$$

The transformation matrices for the Pauli X, Y and Z gates are:

$$X = \begin{bmatrix} 0 & 1 \\ 1 & 0 \end{bmatrix} \tag{1.58}$$

$$Y = \begin{bmatrix} 0 & -i \\ i & 0 \end{bmatrix} \tag{1.59}$$

$$Z = \begin{bmatrix} 1 & 0 \\ 0 & -1 \end{bmatrix} \tag{1.60}$$

When we apply the X gate on the state $|0\rangle$ we find that $X|0\rangle = |1\rangle$ and similarly $X|1\rangle = |0\rangle$. When the Y gate acts on the state $|0\rangle$ it gives $Y|0\rangle = i|1\rangle$ and on the state $|1\rangle$, $Y|1\rangle = i|0\rangle$. The Z gate has this effect on the two states: $Z|0\rangle = |0\rangle$ and $Z|1\rangle = -|1\rangle$. However as stated above qubits take the form of a probability to be in either $|0\rangle$ or $|1\rangle$ state with their respective probabilities α and β. Our qubit is given by $|q\rangle = \alpha|0\rangle + \beta|1\rangle$. When we apply the X, Y and Z gates on $|q\rangle$ we get:

$$X|q\rangle = \begin{bmatrix} 0 & 1 \\ 1 & 0 \end{bmatrix} \begin{bmatrix} \alpha|0\rangle \\ \beta|1\rangle \end{bmatrix} = \beta|0\rangle + \alpha|1\rangle \tag{1.61}$$

$$Y|q\rangle = \begin{bmatrix} 0 & -i \\ i & 0 \end{bmatrix} \begin{bmatrix} \alpha|0\rangle \\ \beta|1\rangle \end{bmatrix} = -i\beta|0\rangle + i\alpha|1\rangle \tag{1.62}$$

$$Z|q\rangle = \begin{bmatrix} 1 & 0 \\ 0 & -1 \end{bmatrix} \begin{bmatrix} \alpha|0\rangle \\ \beta|1\rangle \end{bmatrix} = \alpha|0\rangle - \beta|1\rangle \tag{1.63}$$

The Hadamard gate is another gate widely used in quantum computing algorithms. Its transformation matrix is given by:

$$H = \frac{1}{\sqrt{2}} \begin{bmatrix} 1 & 1 \\ 1 & -1 \end{bmatrix} \tag{1.64}$$

When acting on a qubit which is in a defined state it transforms it into a mix of the two states with an equal probability for each state. For example $H|0\rangle = \frac{1}{\sqrt{2}}(|0\rangle + |1\rangle)$ and $H|1\rangle = \frac{1}{\sqrt{2}}(|0\rangle - |1\rangle)$. However applying the Hadamard gate a second time will produce the original state:

$$H\left(\frac{1}{\sqrt{2}}(|0\rangle + |1\rangle)\right) = |0\rangle \tag{1.65}$$

$$H\left(\frac{1}{\sqrt{2}}(|0\rangle - |1\rangle)\right) = |1\rangle \tag{1.66}$$

This can be seen easily if we multiply the Hadamard transformation matrix by itself. $HH = I$ where I is the identity matrix.

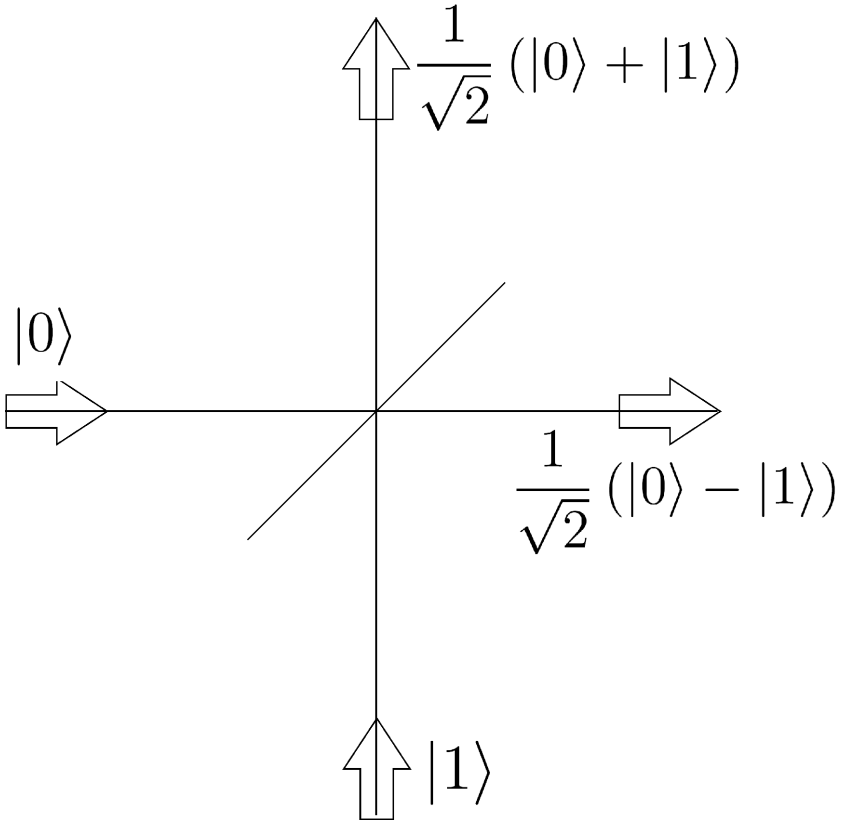

Figure 1.5: A four port 50/50 beam splitter, each input represents a different state. The outputs are a superposition of the input states with equal weighting.

$$HH = \frac{1}{\sqrt{2}\sqrt{2}} \begin{bmatrix} 1 & 1 \\ 1 & -1 \end{bmatrix} \begin{bmatrix} 1 & 1 \\ 1 & -1 \end{bmatrix} = \frac{1}{2} \begin{bmatrix} 2 & 0 \\ 0 & 2 \end{bmatrix} = \begin{bmatrix} 1 & 0 \\ 0 & 1 \end{bmatrix} = I \qquad (1.67)$$

The Hadamard gate is important in quantum computing as it is used in many quantum algorithms as an initial step to map n qubits initialised as the state $|0\rangle$ to a superposition of all 2^n orthogonal states with equal weighting. It is easy to see that a 50/50 beam splitter with two inputs performs the Hadamard transformation as the result from either of the output legs is a superposition of the two inputs with equal probability. Figure 1.5 shows how the input states are mapped to the output states in a four port 50/50 beam splitter.

The last gate I will introduce is the phase gate. This is an important gate to consider in quantum computing and also in quantum optics as it can change the phase of one input relative to the other allowing investigations into phase related interference of particles.

$$R_\phi = \begin{bmatrix} 1 & 0 \\ 0 & e^{i\phi} \end{bmatrix} \tag{1.68}$$

The action of a $PP'P$ barrier in graphene is described in Chapter 2.4.3 which can be represented by a phase gate as it imparts a phase change on charge carriers in one arm of the interferometer compared to the other arm.

Chapter 2

Theoretical Considerations

In order to interfere electrons from two paths it is necessary to create a device which offers two paths to the incoming electron. For the quantum Hall regime, quantum point contacts are used as beam splitters in order to partition a stream of incoming electrons into two paths which can either be detected and their incidence correlated or recombined before detection. In the ballistic regime the carving of a graphene sheet which is required to fabricate a useful quantum point contact would introduce many scattering sites and therefore reduce the coherence length of the electrons. (41) The coherence length must be larger than the dimensions of the device in order to preserve any phase information.

Here is presented a new method to partition the electrons in the ballistic regime using the angular transmission probability of the electrons in graphene as they pass through a PNP barrier. The PNP barrier acts as a Fabry-Perot cavity and thus the transmission probability through the barrier is dependent on the incident angle of the incoming electron. In the following sections tunnelling of electrons through PNP barriers will be discussed. The case of Klein tunnelling is of particular importance in graphene as the chiral nature of the system forbids back scattering of normal incidence electrons.

2.1 Quantum Point Contacts

A quantum point contact (QPC) is a constriction in the conducting material, either physical or via electric field confinement, connecting two electronic reservoirs. QPCs are usually fabricated in such a way that the effective constriction width of the channel as seen by the charged particle can be varied. The width of the constriction confines the momentum of the charged particle perpendicularly to its direction of motion and this defines the number and level of the energy modes of the charged particles which can traverse the constriction.

The first experimental evidence of the quantisation of conductance was shown by van Wees et al (42), the paper describes how they were able to create a constriction in the two dimensional electron gas (2DEG) made of GaAs by applying a negative voltage to a pair of top gates. Importantly the high mobility of the samples used meant that the mean free path was much larger than the dimensions of the device. By varying the voltage on the top gates and thus the effective width of the constriction, the number of available modes can be varied and as such the conductance in quantised.

The energy levels within a constriction on a QPC can be found using Equation 2.1.

$$E(n,k) = s\hbar v_f \sqrt{k_x^2 + \left(\frac{n\pi}{W}\right)^2} \tag{2.1}$$

Where $n = 1, 2, 3...$ is the quantum number of the mode, k_x is the wavevector in the direction of travel of the electron, $\hbar$ is the reduced Planck's constant, $v_f = 1 \times 10^6 ms^{-1}$ is the Fermi velocity in graphene, W is the width of the constriction and $s = \pm 1$ determines the polarity associated with holes and electrons.

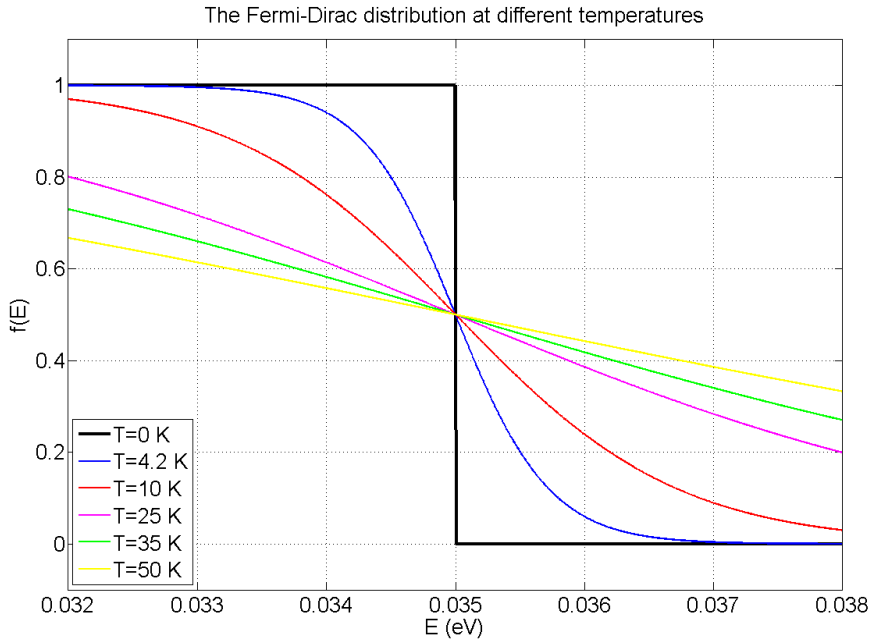

Figure 2.1: Fermi - Dirac energy function for a Fermi level of $0.035eV$ showing how the energy occupation levels change with different temperatures.

Electrons and holes in graphene obey Fermi - Dirac statistics and the distribution function of their energy which is given by Equation 2.2 is shown in Figure 2.1:

$$\overline{n_i} = \frac{1}{e^{(\epsilon_i - \mu)/kT} + 1} \tag{2.2}$$

Where ϵ_i is the energy of the single particle state i, μ is the total chemical potential, k is Boltzmann's constant and T is the temperature in degrees Kelvin (43). In graphene μ is at the Fermi level for $T = 0K$. By including this distribution function in the simulation for the QPCs conductance the temperature dependence of the visibility of the step function can be predicted as seen in Figure 2.2.

As it can be seen in Figure 2.2 the step function associated with the quantisation of conductance can easily be seen for temperatures below $50K$ however this simulation only takes into account the effects of the energy distribution and so a lower

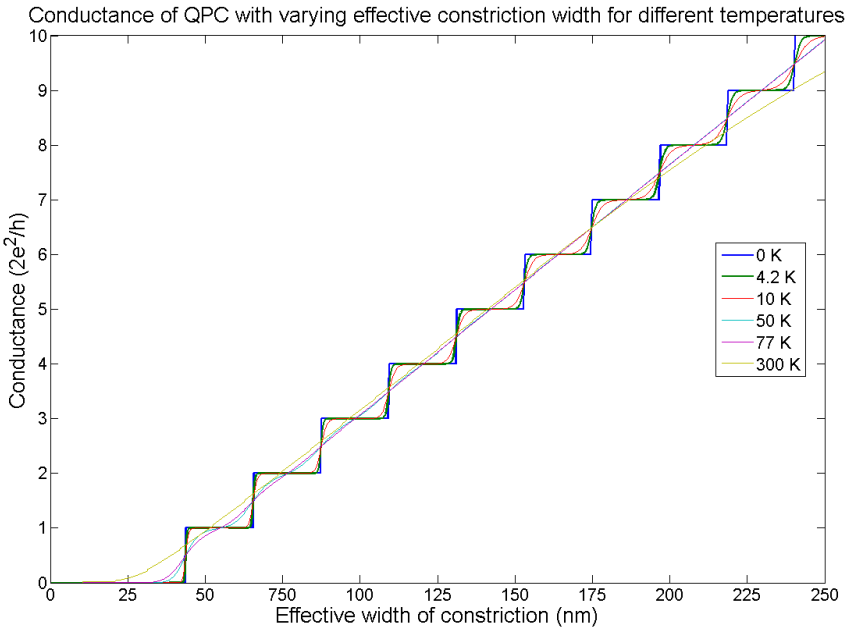

Figure 2.2: Conductance of a QPC at varying temperatures. Combining the step function quantisation with the Fermi-Dirac energy distribution at varying temperatures. At higher temperatures the spread of energy levels washes out the step function.

temperature for measurements is desirable. This indicates that a Liquid Helium cryostat is required in order to see these steps.

The charge carriers in graphene are considered to be part of a 2D massless relativistic system. They are considered this way as they can be described by the dirac like hamiltonian:

$$\hat{H}_0 = -i\hbar v_F \sigma \nabla \tag{2.3}$$

Where $\sigma = (\sigma_x, \sigma_y)$ are the Pauli matrices.

2.2 Klein Tunnelling

When massless relativistic particles are incident on a potential barrier on the order of the electron mass the transmission is nearly 100%. The reflection approaches 0%

as the potential barrier approaches infinity (40). A similar effect to this has been predicted for the electron in graphene as this can be considered as a 2D massless relativistic system (44). The scattering of electrons in the system is restricted by the allowed states available and due to the chiral nature of the system there are no states into which an electron can scatter in the backwards direction when it is in normal incidence with the barrier. If an electron were to try to backscatter it would reverse its wavevector: $\vec{k} -> -\vec{k}$, however due to the momentum vector and pseudospin vector being tied together it would also have to reverse its pseudospin vector: $\vec{\sigma} -> -\vec{\sigma}$ only a pseudospin flip scattering event could allow a change of pseudospin (14). Evidence for Klein tunnelling in graphene has been shown by Stander et al (45) and Gorbachev et al (46). The suppression of backscattering at barrier edges presents a limitation on the design of devices as, for example, a QPC in graphene cannot be simply made using top gates to cause a constriction such as is commonly used in AlGaAs systems. In the traditional system the top gate is used to deplete the areas under them of electron density and therefore suppress conduction through these regions. With monolayer graphene however a gap does not exist and also for a normal incidence the transmission remains very high and even for non-normal incidences the transmission probability is non zero and can be as much as 100%.

Van Duppen and Peeters predict the transmission for PN junctions using 1-4 layers of graphene (47). They show that for monolayer graphene the PN junction transmits perfectly at normal incident angle for all variations of step height. In contrast with bilayer there are two angles, either side of the normal, which are able to transmit which are dependent on the symmetry of the step height. This means that given a point like source, close to a linear symmetrical PN junction, the only transmission would occur at two distinct points equidistant from each other along the PN junction. Assuming purely ballistic transport then at all other parts of the PN junction the electrons could only arrive with wavevectors which

are not allowed to transmit and so will reflect.

2.3 Negative Refraction

It has been theorised that when electrons in graphene travel from a region of positive doping to a region of negative doping that the wavevector would change in such a way as to refract on the same side of the normal as the incoming angle (36). This would be a very useful effect for focusing the beam back to one detector and recombining previously separated paths. This effect can be explained by looking at the energy dispersion for the electron in each region to determine the relation of its group velocity to its wavevector and considering momentum conservation along the edge of the barrier.

The energy dispersion relation for an electron in the conduction band is:

$$\varepsilon_c(\boldsymbol{k_F}) = \hbar V_F \boldsymbol{k_F} \tag{2.4}$$

The group velocity is defined as:

$$\boldsymbol{V_{group}} = \frac{1}{\hbar}\frac{d\varepsilon(\boldsymbol{k_F})}{d\boldsymbol{k_F}} \tag{2.5}$$

Therefore the group velocity of an electron in the conduction band is:

$$\boldsymbol{V_c} = V_F\frac{\boldsymbol{k_F}}{k_F} \tag{2.6}$$

The energy dispersion relation for an electron in the valence band is:

$$\varepsilon_v(\boldsymbol{k_F}) = -\hbar V_F \boldsymbol{k_F} \tag{2.7}$$

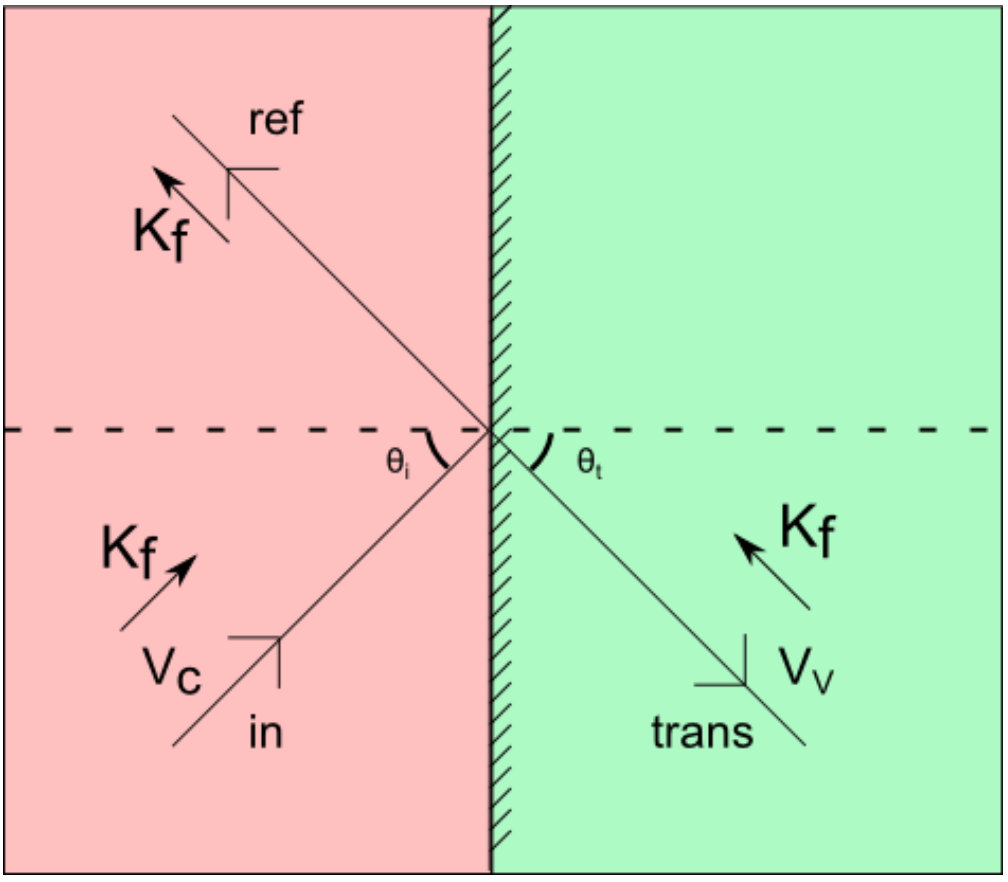

Figure 2.3: Schematic showing the wavevector and group velocity directions of the incoming, reflected and transmitted electron. The P doped region is shown in red and the N doped region is shown in green.

and similarly the group velocity of an electron in the valence band is:

$$\boldsymbol{V_v} = -V_F \frac{\boldsymbol{k_F}}{k_F} \tag{2.8}$$

Consider an electron approaching a PN junction with angle of incidence, ϕ, to the normal of the step. Its wavevector is given as $\boldsymbol{k_F} = (k_x, k_y) = E(cos(\phi), sin(\phi))$.

If it is initially in the conduction band its group velocity is $\boldsymbol{V_c} = V_F \frac{\boldsymbol{k_F}}{k_F}$. When it moves to the conduction band its group velocity is given by $\boldsymbol{V_v} = -V_F \frac{\boldsymbol{k_F}}{k_F}$ and now its group velocity is anti-parallel to its wavevector.

Due to conservation of momentum in the y direction (along the step edge) $k_y = k'_y$ this leads to negative refraction.

The wavevector of the electron in the valence band has components $\boldsymbol{k_F} = (k'_x, k_y)$. Where k'_x is proportional to $\frac{\varepsilon_f}{\varepsilon'_f} k_x$.

Thus a diverging beam on the left side of the PN junction will converge on the right. If it is a symmetric junction and $|\varepsilon_f| = |\varepsilon'_f|$ then the focus and the point source will be equidistant from the PN junction. (14)

2.4 PNP Barrier Transmission

2.4.1 Monolayer Graphene with a PNP Barrier

Katsnelson et al looked at the transmission of electrons through PNP barriers (44). Due to Klein tunnelling it is found that electrons with an incidence angle close to $\phi = 0$ have a 100% probability of transmission through the barrier as back scattering is prohibited. Referring to Figure 2.4, consider an electron with wavevector k_f, travelling at an angle ϕ towards a barrier of height, V_0 which has a thickness of D. The barrier is positioned so the left edge is at $x = 0$ and the right edge at $x = D$.

The components of the incoming wavevector in the x and y directions are labelled k_x and k_y. q is the wave vector under the gate within the barrier region and is defined as $q = (E - V_0)/\hbar v_f$. By conservation of momentum parallel to the barrier edge $q_y = k_y$ and so q_x is given by:

$$q_x = \sqrt{(E - V_0)^2 / \hbar^2 v_f^2 - k_y^2} \tag{2.9}$$

$$k_y = k_f \sin\phi \tag{2.10}$$

$$s = \mathrm{sgn}E \;\; \& \;\; s' = \mathrm{sgn}\left(E - V_0\right) \tag{2.11}$$

$$\theta = \tan^{-1}\left(k_y/q_x\right) \tag{2.12}$$

$$\Psi(x,y) = \begin{cases} \begin{pmatrix} 1 \\ se^{i\phi} \end{pmatrix} e^{ik_x x} e^{ik_y y} + r \begin{pmatrix} 1 \\ -se^{-i\phi} \end{pmatrix} e^{-ik_x x} e^{ik_y y}, & x < 0, \\ A \begin{pmatrix} 1 \\ s'e^{i\theta} \end{pmatrix} e^{iq_x x} e^{ik_y y} + B \begin{pmatrix} 1 \\ -s'e^{-i\theta} \end{pmatrix} e^{-iq_x x} e^{ik_y y}, & 0 < x < D, \\ t \begin{pmatrix} 1 \\ se^{i\phi} \end{pmatrix} e^{ik_x x} e^{ik_y y}, & x > D, \end{cases} \tag{2.13}$$

By asserting that the wavefunctions are continuous at the barriers edges, ie at $x = 0$ and $x = D$, we can solve for the reflection coefficient, r:

$$r = 2ie^{i\phi} \sin\left(q_x D\right) \times \frac{\sin\phi - ss'\sin\theta}{ss'\left[e^{-iq_x D}\cos\left(\phi+\theta\right) + e^{-iq_x D}\cos\left(\phi-\theta\right)\right] - 2i\sin\left(q_x D\right)} \tag{2.14}$$

We can see from Equation 2.14 that at normal incidence there is perfect transmission, however at angles $|\phi| > 0$ the transmission probability, T, is determined by:

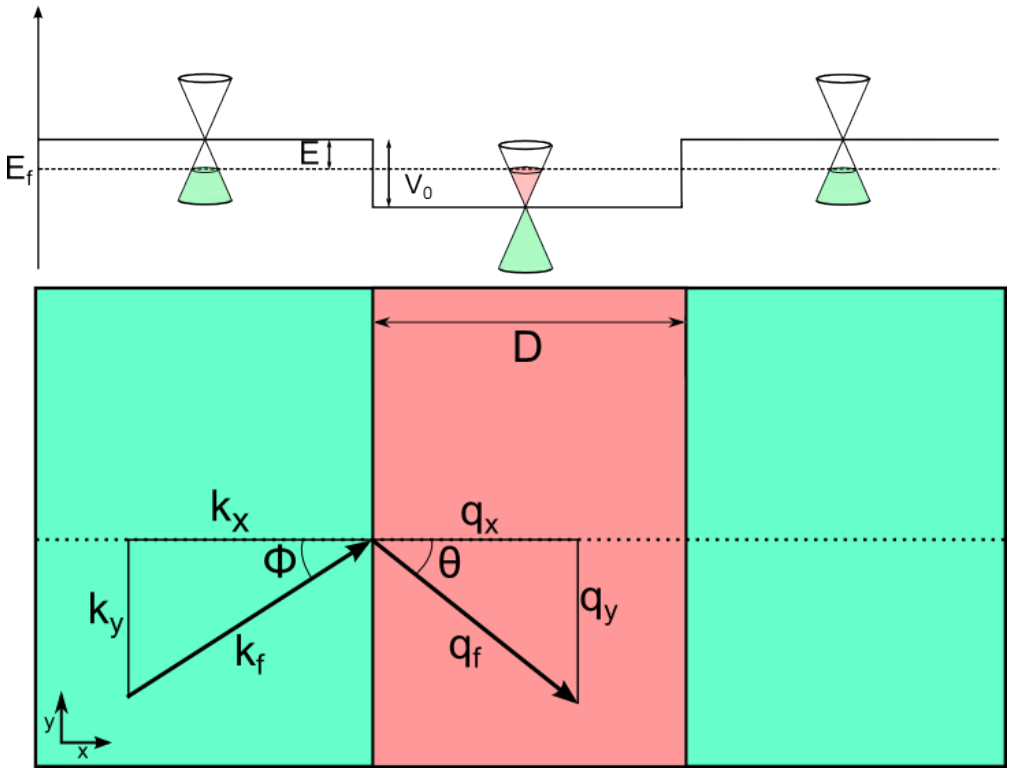

Figure 2.4: Diagram of wave vectors through PNP barrier of height V_0 and width D. The incoming electron approaches the barrier at an angle of ϕ to the normal of the barrier, after passing the first interface it travels at an angle of θ.

$$T = |t^2| = 1 - |r^2| \tag{2.15}$$

Figure 2.5 shows a plot of T, the transmission probability, using equations 2.15 & 2.14 as a function of incidence angle through a barrier with width $D = 100nm$ with two different barrier heights of 318 meV and 427 meV, which correspond to charge carrier densities of $1.5 \times 10^{12} cm^{-2}$ and $3.5 \times 10^{12} cm^{-2}$ respectively under the barrier. The charge carrier density in the areas either side of the barrier was fixed at $5 \times 10^{11} cm^{-2}$. Changing the barrier heights via the topgate potential varies the allowed transmission angles.

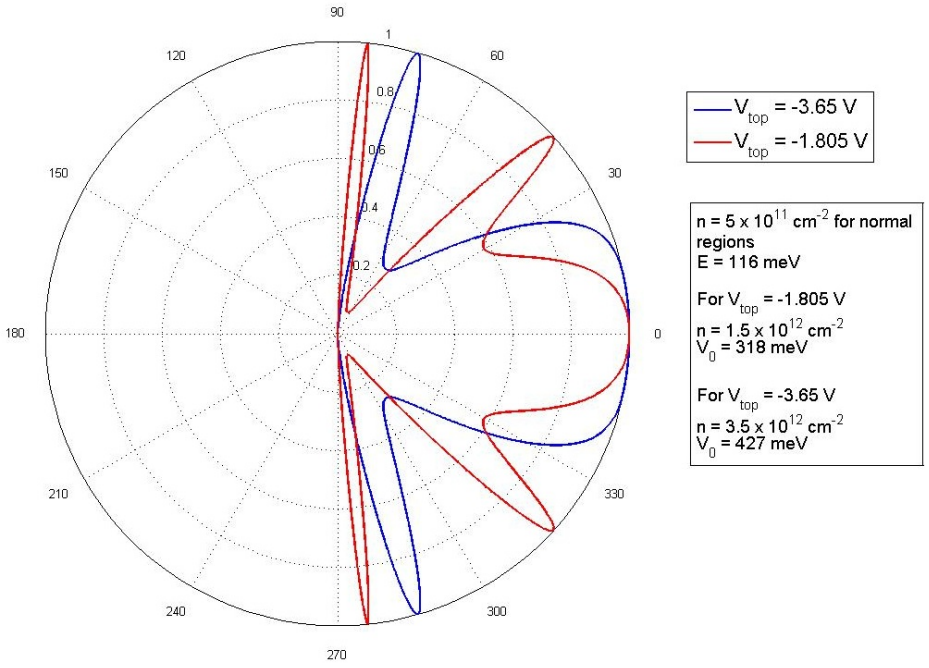

Figure 2.5: Transmission as a function of angle through a PNP barrier of width $100nm$, plotted for two different barrier heights. Note that the transmission for $\phi = 0$ remains at 100%.

2.4.2 Bi-layer Graphene with a PN Junction

(47) show that when a PN junction is formed in bi layer graphene the transmission probability for an electron is dependent on its angle of incidence with the barrier. The transmission T, is given by:

$$T = \left|\frac{E}{V_0}\right| \sin^2(2\phi) \tag{2.16}$$

Tudorovskiy et al and Katsnelson et al also agree that this analytical solution is appropriate when given that $V >> E$ (44) (48) .

Figure 2.6 shows the transmission of a PN junction in bilayer graphene as a function of incidence angle. This is a very useful result as it partitions the electrons into two separate directions. We can easily imagine creating a beam splitter from

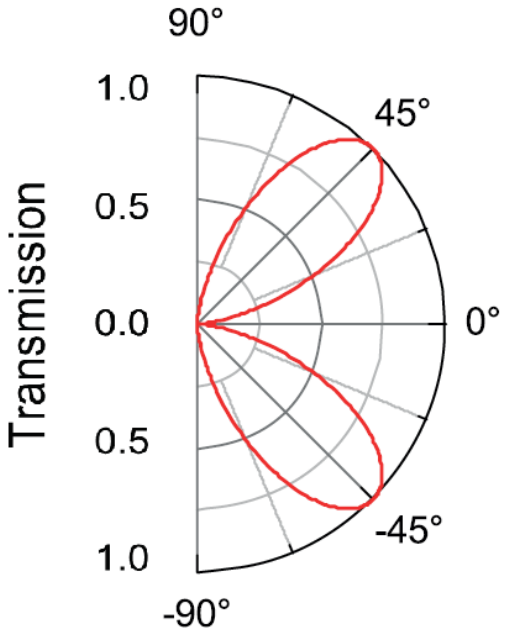

Figure 2.6: Transmission as a function of angle through a PN junction in bilayer graphene. (47)

a PN junction in bilayer graphene from this transmission.

2.4.3 PP'P or NN'N

In order to measure an interference of the two paths a method for controlling an additional phase on one or both of the paths is required. As the devices dimensions are fixed after fabrication the path length cannot be altered during measurements to add a phase shift, however the wavelength of the electrons is dependent on the wavevector on which control can be accessed via the top and bottom gates. To produce an additional phase whilst avoiding the introduction of further angular selection a top gate could be used which forms a barrier which does not cross the Dirac point. Such barriers are known as $PP'P$ or $NN'N$ junctions, depending on the band in which the electron is residing. In this case as the electron does not

change bands as it passes under or over the barrier, the relative sign of its group velocity to its wavevector does not change and therefore regular diffraction occurs.

For the electron in an N doped region the group velocity is given by:

$$\boldsymbol{V_N} = V_F \frac{\boldsymbol{k_N}}{k_N} \tag{2.17}$$

Where $\boldsymbol{k_N}$ is the wavevector of the electron in this N region. When the electron is under a gate which alters the potential energy to a different value N' but not a different sign then the group velocity is:

$$\boldsymbol{V_{N'}} = V_F \frac{\boldsymbol{k_{N'}}}{k_{N'}} \tag{2.18}$$

However the magnitude of the wavevector, and therefore the wavelength, will change as it is dependent on energy. In general the wavevector is related to the energy by:

$$E_f = \hbar V_F \boldsymbol{k_F} \tag{2.19}$$

This change in wavelength will lead to an additional phase for an electron passing through the barrier compared to a similar electron path without the barrier.

The additional phase shift can be found by considering the wavelength of the electron for the N and N' regions and comparing the two for a given $NN'N$ barrier width of $100nm$ as shown in Figure 2.7.

The wavelengths of the electron in the N and N' regions, λ_1 & λ_2 respectively, are given by:

$$\lambda_1 = 2\sqrt{\frac{\pi}{n_{bg}}} \tag{2.20}$$

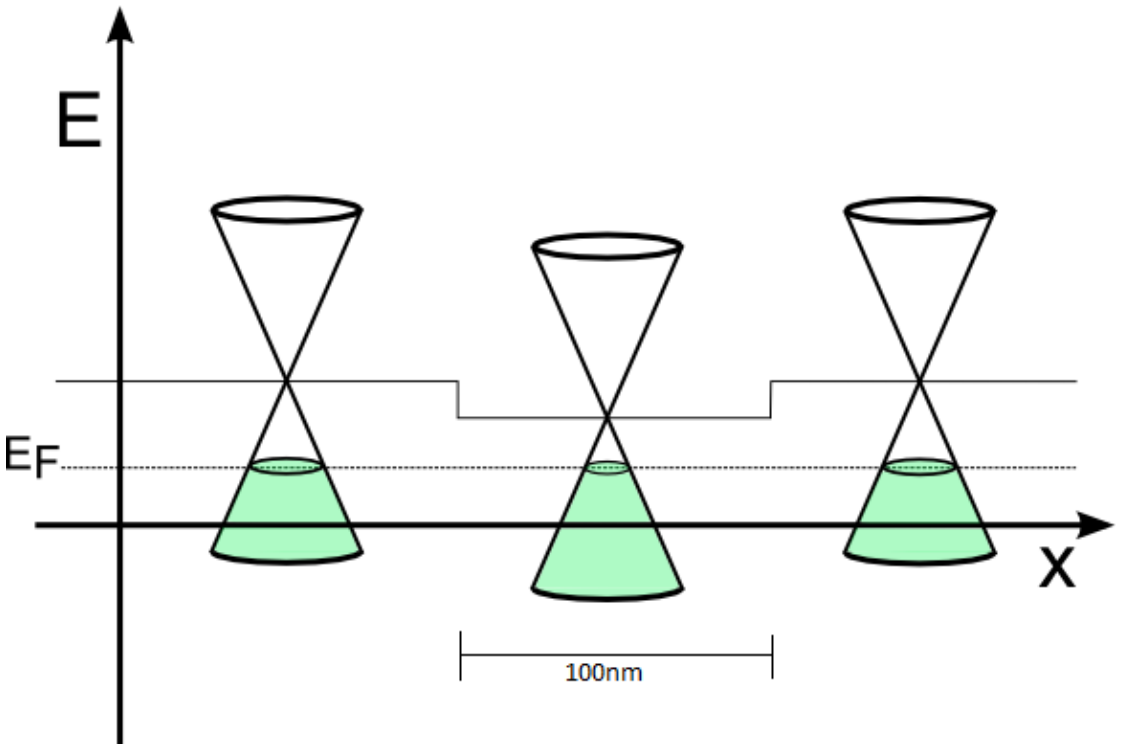

Figure 2.7: A 100nm wide NN'N barrier, note that the Fermi energy has the same sign throughout the system and it does not cross the Dirac point.

n_{bg} is the charge carrier density induced by the back gate which is found as:

$$n_{bg} = \frac{C_{bg}V_{bg}}{e} \tag{2.21}$$

Where C_{bg} is the capacitance of the back gate to the graphene flake, V_{bg} is the back gate voltage relative to the Dirac point and e is the charge of the electron. C_{bg} is calculated for the device using a parallel plate capacitance model:

$$C_{bg} = \frac{\epsilon_0\epsilon_r}{t_{bg}} \tag{2.22}$$

Where ϵ_0 is the vacuum permitivity, ϵ_r is the relative permitivity of the dielectric material and t_{bg} is the thickness of the dielectric material forming the backgate.

Now we can see how the wavelength of the electron is inversely related to the square root of the back gate voltage.

$$\lambda_1 = 2\sqrt{\frac{\pi e}{C_{bg}V_{bg}}} \tag{2.23}$$

For the electron in the N' region we must consider the capacitive contributions from both the top and bottom gates in the calculation of the charge carrier density. The charge carrier density induced by the top gate n_{tg} can be calculated using:

$$n_{tg} = \frac{C_{tg}V_{tg}}{e} \tag{2.24}$$

Where V_{tg} is the voltage on the top gate, e is the electron charge and C_{tg} is the capacitance of the topgate to the graphene flake, again modelled as a parallel plate capacitor:

$$C_{tg} = \frac{\epsilon_0\epsilon_r}{t_{tg}} \tag{2.25}$$

To find the wavelength, λ_2, of the electron under the topgate the contributions to the charge carrier density from both top and back gates must be taken into account:

$$\lambda_2 = 2\sqrt{\pi e\left(\frac{1}{C_{bg}V_{bg} + C_{tg}V_{tg}}\right)} \tag{2.26}$$

The additional phase, $\triangle\phi$, is therefore given by:

$$\triangle\,\phi = 2\pi d\left(\frac{1}{\lambda_1} - \frac{1}{\lambda_2}\right) \tag{2.27}$$

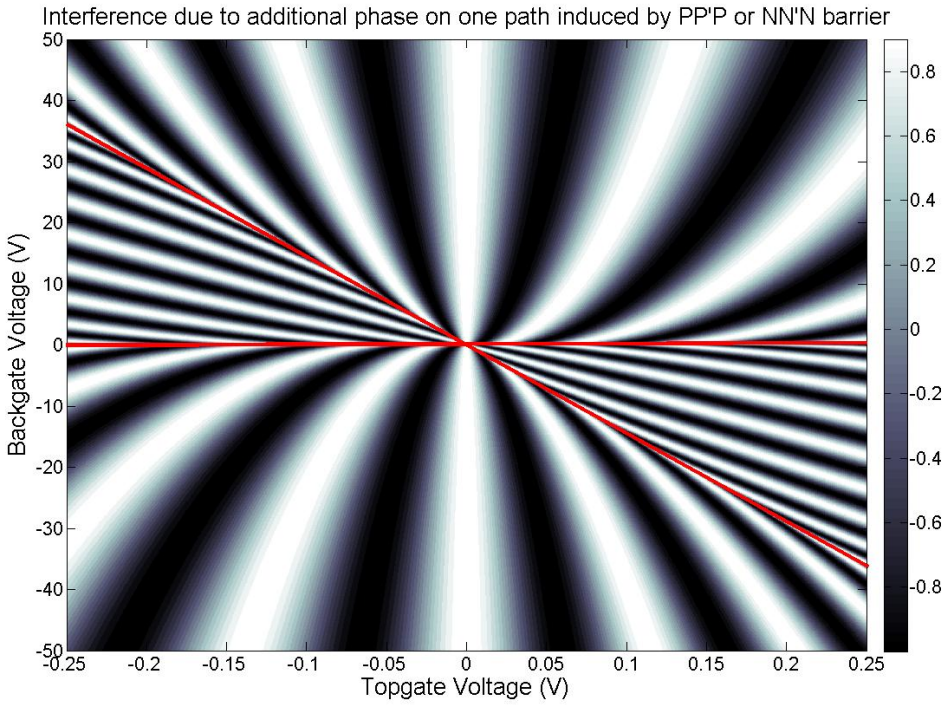

Figure 2.8: Expected interference pattern when varying the gate voltages. The width of the top gated barrier is set to $100nm$. The triangular areas bounded by the two red lines are regions of PNP or NPN operation whilst the areas above and below are regions of NN'N or PP'P operation.

Where d is the width of the topgate in the direction of electron travel. A simulation of this phase difference and the resulting interference has been completed and Figure 2.8 shows the interference due to $\triangle\phi$ as a function of the back gate and topgate voltages using a barrier width of $100nm$. This simulation shows that when using a barrier width of $100nm$ which is attainable with e-beam technology, the interference fringes appear with a separation which is well within the reach of the resolution of DC measuring equipment. As discussed in Chapter 3.8.2 an Agilent Parameter Analyser is used to take measurements. The two triangular regions which are bounded by the two red lines in Figure 2.8 are those that represent the area under the topgate passing through the Dirac point, i.e a PNP or NPN barrier which as stated earlier is to be avoided for the purpose of the additional phase.

2.5 The Split Path Lens Interferometer

Using the combination of the angle dependent transmission probability from equation 2.16 with negative refractive lensing as shown in Section 2.3 an interferometer with two spatially separated paths can be envisaged. A simulation of the Split Path Lens (SPL) Interferometer is shown Figure 2.9, the expected electron trajectories through a bilayer graphene PNP barrier are shown. The local top gate which forms the barrier is shown in red and the energy levels are set such that $\left|\frac{\varepsilon_f}{\varepsilon'_f}\right| = 1$ i.e a symmetric barrier. The electrons trajectories, shown in blue, negatively refract through the PNP barrier and are selectively transmitted through to the detector on the right. The reflected trajectories are omitted for clarity. $PP'P$ or $NN'N$ barriers can be added to each separated path on the right of the SPL interferometer to induce a phase shift as described in Subsection 2.4.3 or a phase shift can be induced by a magnetic field using the Aharonov-Bohm effect as described in Section 2.6.

2.6 Aharonov–Bohm Effect

When there is a magnetic flux enclosed by the possible paths of the electrons, an electron travelling along one path will receive a phase shift relative to the other path. This is known as the Aharonov-Bohm effect. The two paths in the split path lens interferometer proposed in Chapter 2.5 allow such a case to occur and this can be measured by measuring the conductance of the device whilst varying the magnetic field perpendicular to the device. The change in the phase of one path relative to the other, $\triangle\phi$, is given by:

$$\triangle \phi = \frac{e\boldsymbol{B} \cdot s}{\hbar} \tag{2.28}$$

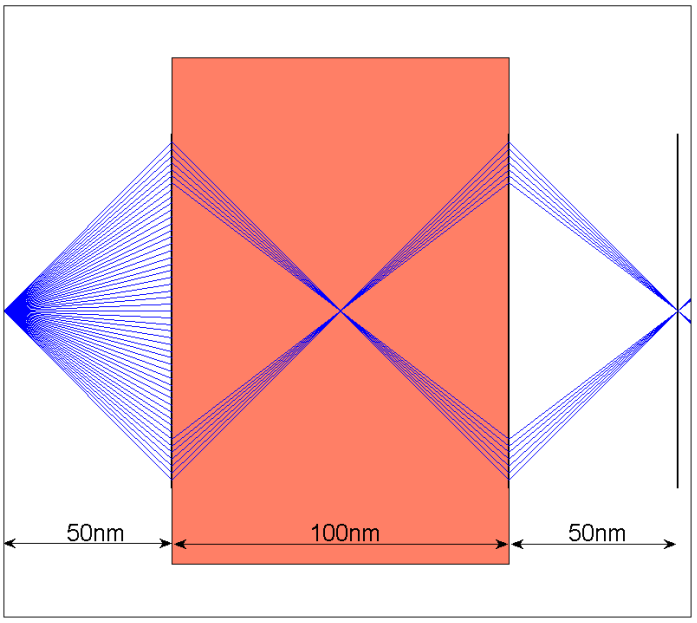

Figure 2.9: Electron trajectories through a PNP barrier with $\left|\frac{\varepsilon_f}{\varepsilon'_f}\right| = 1$ in bilayer graphene. The red section is the local top gated part which causes negative refraction. The electrons enter from a modelled point source on the left of the image, negatively refract through the barrier and the total transmission through the barrier is selective of incidence angle. Reflection trajectories are not shown for clarity.

Where B is the magnetic field enclosed in an area s.

The conductance is therefore expected to show a magnetic field dependent oscillation with a period set by $\triangle\phi = 2\pi$. I.e:

$$\triangle B = \frac{h}{e.s} \tag{2.29}$$

Device designs for the split path interferometer can vary and so then would the area which would be enclosed by the split path. A typical device would have $s \approx 1\mu m^2$ for which equation 2.29 gives an oscillation period of $\triangle B = 4.2mT$.

2.7 Practical Requirements & Device Constraints

For interference to be seen one requirement is that the coherence length of the electrons is longer than the critical device dimensions. An experimentally measurable variable is the mean free path which is related to the mobility as:

$$\mu = \frac{l_m e}{V_f m_e m^*} \tag{2.30}$$

To achieve a mean free path $l_m = 2\mu m$ it is required to have a device with mobility $\mu > 120,000 cm^2 V^{-1} s^{-1}$. This has been shown to be achievable with graphene samples by using a hBN substrate (49). Wang et al have shown that by stacking up the hBN and graphene first to encapsulate the graphene layer and then using 1-dimensional contacts for the devices they were able to achieve mean free paths which were only limited by the device length (33). A maximum of $l_m = 16\mu m$ was shown to be possible.

Graphene and hBN flakes can regularly be exfoliated with dimensions $> 10\mu m$ and the e-beam lithography places a lower limit on the feature sizes of the devices of $> 100nm$.

Other practical requirements on the device to achieve interference are that the ohmic contacts are sufficiently connected to the graphene flake such that there is not a prohibitively high contact resistance. Previous samples have shown that using standard cleaning procedures between the e-beam and evaporation steps is sufficient to produce samples with a resistivity of $1k\Omega$ which is in line with reported values. (50)

The local top gates and back gate should be electrically isolated from the graphene sheet so that no conduction occurs from the gates to the flake under measurement. For the back gate this is achieved via the SiO_2 dielectric and hBN substrate under

the graphene. Leakage of current from the backgate through to the device has been seen in some of my samples and the implications and a proposed solution are discussed in Section 3.6. Similarly the top gates are electrically isolated from the graphene flake by the thin few layer hBN flake on top of the graphene flake.

In order to achieve the highest mobility in the devices measurements take place at low temperatures; $\sim 4K$ using a Helium cryostat. This low temperature is required to inhibit phonon modes within the graphene flake to reduce electron-phonon scattering. The cryostat, described in Section 3.8, contains a superconducting magnet which can provide a magnetic field perpendicular to the plane of the device up to 10T. It is possible to control the field value by steps of 0.1 gauss which is sufficient to measure the Aharonov-Bohm oscillations which are expected to have a periodicity of 42 gauss as calculated in Section 2.6.

2.8 Gate Capacitance

A PN - Junction is formed by two areas of the graphene flake under opposing potential. This is realised experimentally by using top and back gates. Figure 2.10 shows a cut through schematic of the layers required to produce the potential landscape required for PNP graphene devices. The backgate is isolated from the graphene flake by the SiO_2 and hBN insulating layers. The top gate is isolated from the graphene flake by the top layer of hBN. The SiO_2 layer is $290nm$ thick and typically the hBN flakes for the top dielectric are two or three layers which is on the order of $1-2nm$. As the top dielectric of hBN is two orders of magnitude thinner than the combined SiO_2 and hBN layers forming the back dielectric the topgate has a much greater influence on the potential for the parts of the graphene between both gates and therefore can allow for PN or PNP junctions to be created.

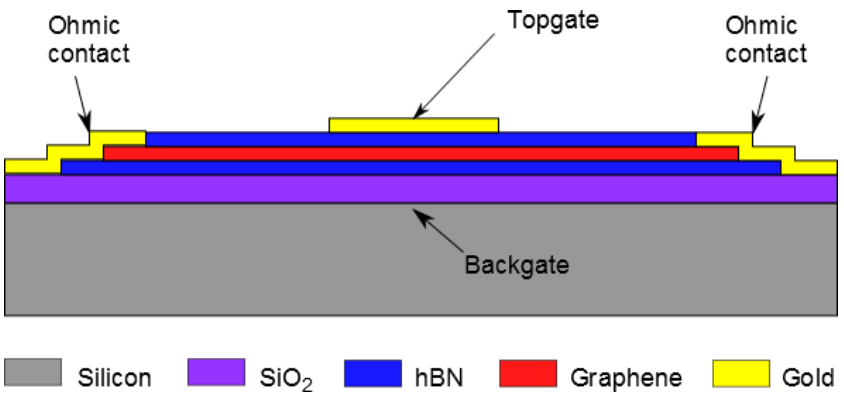

Figure 2.10: A cut through schematic diagram showing the layers which are used to construct PNP devices. A highly doped Silicon substrate is coated with $290nm$ of SiO_2, on top of which is placed the subsequent layers of hBN and graphene.

The gates can be modelled as parallel plate capacitors and the capacitance contribution from each of the dielectric layers to the graphene flake found as:

$$C_{SiO_2} = \epsilon\epsilon_{r_{SiO_2}}/d_{SiO_2} \tag{2.31}$$

$$C_{hBN}^{back} = \epsilon\epsilon_{r_{hBN}}/d_{hBN}^{back} \tag{2.32}$$

$$C_{hBN}^{top} = \epsilon\epsilon_{r_{hBN}}/d_{hBN}^{top} \tag{2.33}$$

With $\epsilon = 8.854\times10^{-12}Fm^{-1}$, $\epsilon_{r_{SiO_2}} = 3.9$, $\epsilon_{r_{hBN}} = 4$, $d_{SiO_2} = 290nm$, $d_{hBN}^{top} \approx 1nm$ and $d_{hBN}^{back} \approx 10nm$

Then the total gate capacitances are:

$$C_{hBN}^{back} = 3.54 \times 10^{-3}F \tag{2.34}$$

$$C_{SiO_2} = 1.19 \times 10^{-4} F \tag{2.35}$$

$$\frac{1}{C_{total}^{back}} = \frac{1}{C_{SiO_2}} + \frac{1}{C_{hBN}^{back}} \tag{2.36}$$

$$C_{total}^{top} = 3.54 \times 10^{-2} F \tag{2.37}$$

$$C_{total}^{back} = 1.15 \times 10^{-4} F \tag{2.38}$$

(31) and (51) for the $\epsilon_{r_{hBN}} = 4$ value.

So the top gate is coupled 300 times more strongly than the back gate which allows for local regions defined by the top gates with different electrostatic doping than the bulk of the graphene flake which is influenced only by the backgate.

2.9 Electron Wavelength

The parallel plate capacitance, C of a system with t thickness dielectric is:

$$C = \frac{\varepsilon_0 \varepsilon_r}{t} \tag{2.39}$$

Where ε_0 is the permittivity of free space and ε_r is the relative permittivity of the dielectric.

The charge carrier density, n, induced by a backgate voltage, V_{bg} is given by:

$$n = \frac{CV_{bg}}{e} \tag{2.40}$$

Where e is the charge of an electron. The wavevector, k, is related to the charge carrier density in monolayer graphene as:

$$k = \sqrt{\pi n} \tag{2.41}$$

The de Broglie wavelength λ_{dB} associated with this wavevector is given by:

$$\lambda_{dB} = \frac{2\pi}{k} \tag{2.42}$$

Combining the above equations we can find a relation between the backgate voltage, V_{bg} and the de Broglie wavelength:

$$\lambda_{dB} = \sqrt{\frac{4\pi et}{\varepsilon_0 \varepsilon_r V_{bg}}} \tag{2.43}$$

For the specific case of a graphene system which has a backgate dielectric consisting of a thickness, $t = 290nm$ of SiO_2 which has a relative permittivity, $\varepsilon_r = 3.9$ and using the values for the permittivity of free space, $\varepsilon_0 = 8.85 \times 10^{-12} Fm^{-1}$ and the electron charge, $e = 1.6 \times 10^{-19} C$ we find that the relationship reduces to:

$$\lambda_{dB} = \frac{129nmV^{0.5}}{\sqrt{V_{bg}}} \tag{2.44}$$

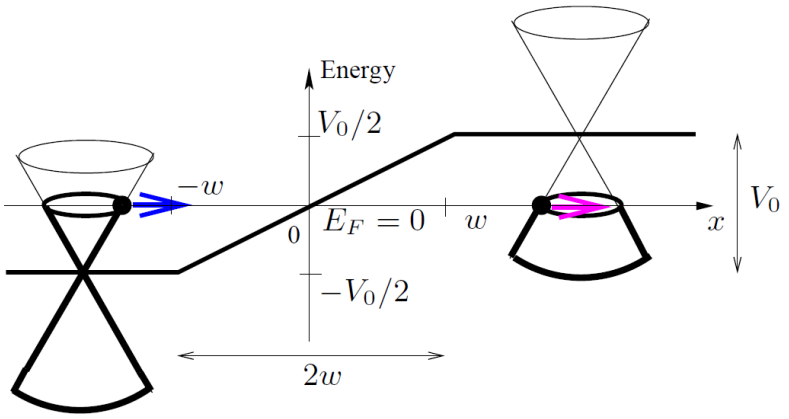

Figure 2.11: A smooth PN junction with potential height V_0 and width $2w$. (14)

2.10 Edge Sharpness

As Klein tunnelling is reliant on the potential barrier being tall and sharp when compared to the electron mass it is important to analyse the edges which will be created in the potential landscape of the graphene devices. Allain and Fuchs found that a PN junction with a smooth edge will have a collimating effect on the incident electrons as it only allows the transmission of electrons which are close to normal incidence with the junction (14). They define a junction as sharp if $k_f w < 1$ where the width of the slope is 2 w as illustrated in Figure 2.11 so the width of the slope of the junction should be on the order of the electron wavelength.

Chapter 3

Experimental Methods

3.1 Sample Preparation

3.1.1 Sample Design

3.1.2 Chip Fabrication

Exfoliation of graphene flakes leads to a random distribution of flakes of various sizes and thickness's and in random positions. In order to select a monolayer flake $300nm$ SiO_2 is used as the substrate as this makes the graphene flakes visible under an optical microscope. A grid of markers on the chips before exfoliation is necessary to document locations of flakes for ease of locating them at a later time and also imperative for the alignment of the metal contacts.

Chips were fabricated from $4''$ wafers of Silicon coated with $300nm$ SiO_2 bought from IDB technologies LTD. Each wafer produced 20 chips each $15mm$ x $15mm$ in size with a usable area of $5mm$ x $5mm$. The size of $15mm$ x $15mm$ is chosen as the smallest size which can be used in the JEOL JBX-9300FS electron beam

lithography system and the Carl Zeiss Orion helium ion microscope. The $5mm$ x $5mm$ size of usable area is the largest size chip which will fit into the chip holders which fit in the liquid helium cryostat.

The fabrication of chips from the wafers involved a two step lift off technique. This is because the wire bonding step which comes much later after sample fabrication requires a very thick layer of metal on which to bond. If too thin a layer is used the bonder can puncture the metal and SiO_2 layers which causes back gate leakage. However when patterning the contacts from the graphene flake to the bonding pads if there is too high a step then this can cause discontinuation of the connection. Thus the first pattern includes the grids of markers used to locate graphene, a series of tabs which will protrude from under the bonding pads and some alignment markers used to align the photomask as all of these require a smaller thickness. Then a second pattern which is on a photomask contains the bonding pads and thick lines separating the 20 chips which are visible to the naked eye; these are used to align the dicer when cutting the wafer into the chips.

The first step is to spin coat the wafers in a double layer MMA/PMMA e-beam resist. A pattern was exposed onto the resist using a JEOL JBX-9300FS electron beam lithography system. This first pattern consisted of the grid of alignment markers for each chip and some larger alignment markers to be used to align the photomask of the second pattern to the first pattern. This was developed using a 1:1 ratio mix of IPA:MIBK for 90 seconds. Figures 3.1 (a) and (b) show parts of the exposed and developed pattern.

The next stage is the evaporation of metals onto the patterned resist, this consisted of a 5nm layer of Chrome followed by a 70nm layer of Gold. Figure 3.2 (a) shows the same wafer after the metal films have been evaporated.

The sacrificial layer of resist is removed using acetone to leave the grids of gold markers on the wafer. Figure 3.2 (b) shows this in progress. Figures 3.3 (a) and

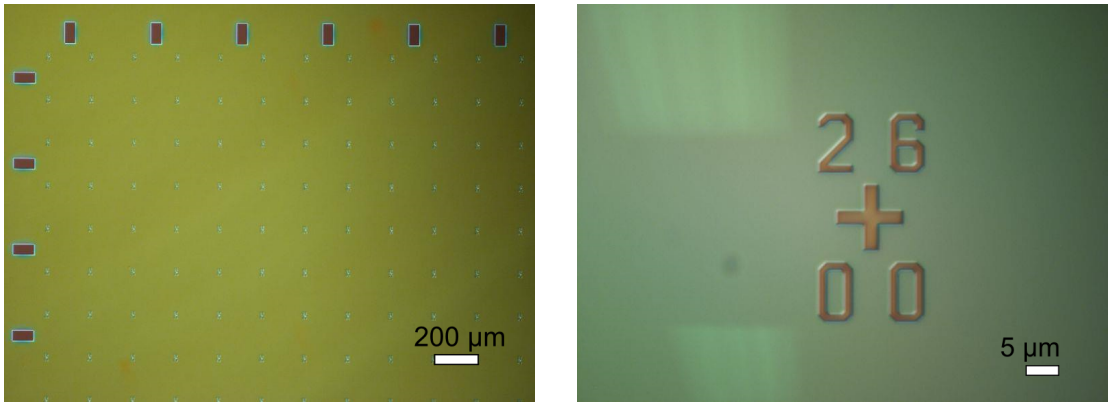

(a) (b)

Figure 3.1: (a) Optical micrograph of the grid of markers patterned into the MMA/PMMA resist. Larger tabs can be seen around the edge of the grid. (b) Optical micrograph of a single alignment marker patterned into the MMA/PMMA resist. The dimensions of the crosses are $10\mu m$ x $10\mu m$ and are $2\mu m$ thick, the numbers use $1\mu m$ thick lines.

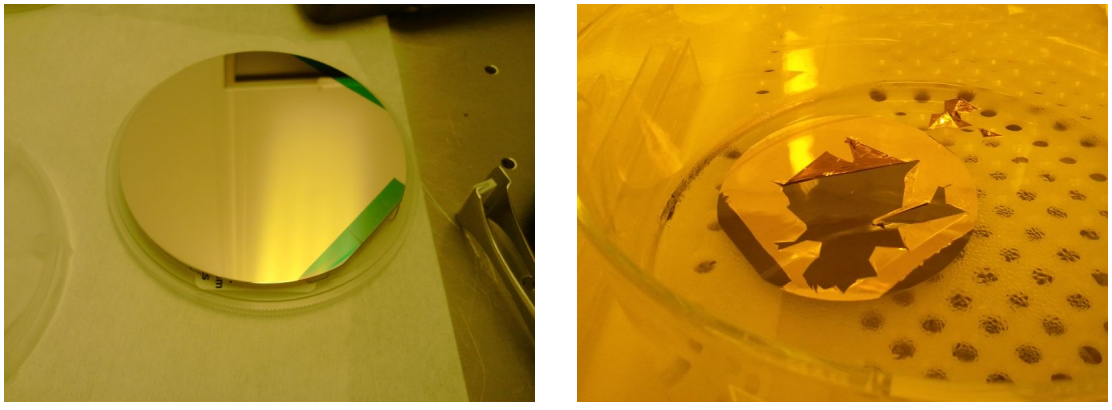

(a) (b)

Figure 3.2: (a) The wafer is coated in $5nm$ of Chrome and then $70nm$ of Gold. (b) The wafer part way through the lift off process; the PMMA layer under the metal is dissolved by the acetone and any metal which is on the PMMA is removed leaving metal only in the areas in which the pattern was developed in the PMMA.

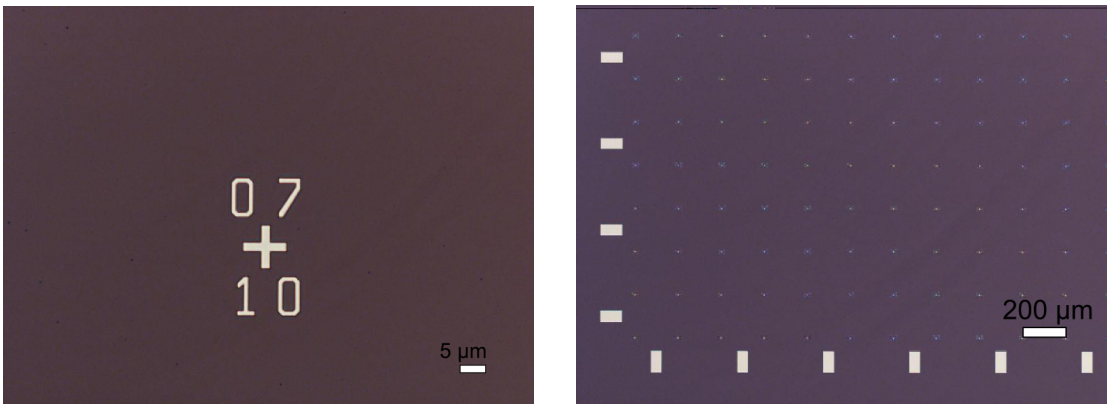

(a) (b)

Figure 3.3: (a) Magnified Optical Micrograph of a gold alignment marker after the lift off process. (b) Optical Micrograph of the grid of gold alignment markers and tabs surrounding the grid.

(b) show the resulting gold markers after lift off.

Next the wafer is spin coated with a layer of negative photo resist AZ2070 and placed into an EVG 620 T single side mask aligner and the mask is aligned to the alignment markers on the wafer. The pattern is exposed with UV light for 5 seconds and then developed in AZ726 developer for 120 seconds. Figure 3.4 (a) shows the wafer after this photo mask pattern has been exposed and developed.

A second metal evaporation step is then made, this time with 10nm Chrome and 500nm Gold and it is again put in acetone to lift off the sacrificial layer. Figure 3.4 (b) shows the wafer after this final lift off process, twenty chips were produced from each wafer.

The wafer is now ready to be diced into chips. It is stuck down to the blue dicing tape with the patterned side up and the dicer is aligned to cut along the lines of gold which separate the chips as patterned by the photomask, Figure 3.5 shows a single chip after dicing.

Once all of the chips are diced the whole wafer of chips is carefully transferred to a second piece of blue dicing tape, this time with the patterned side down. It is

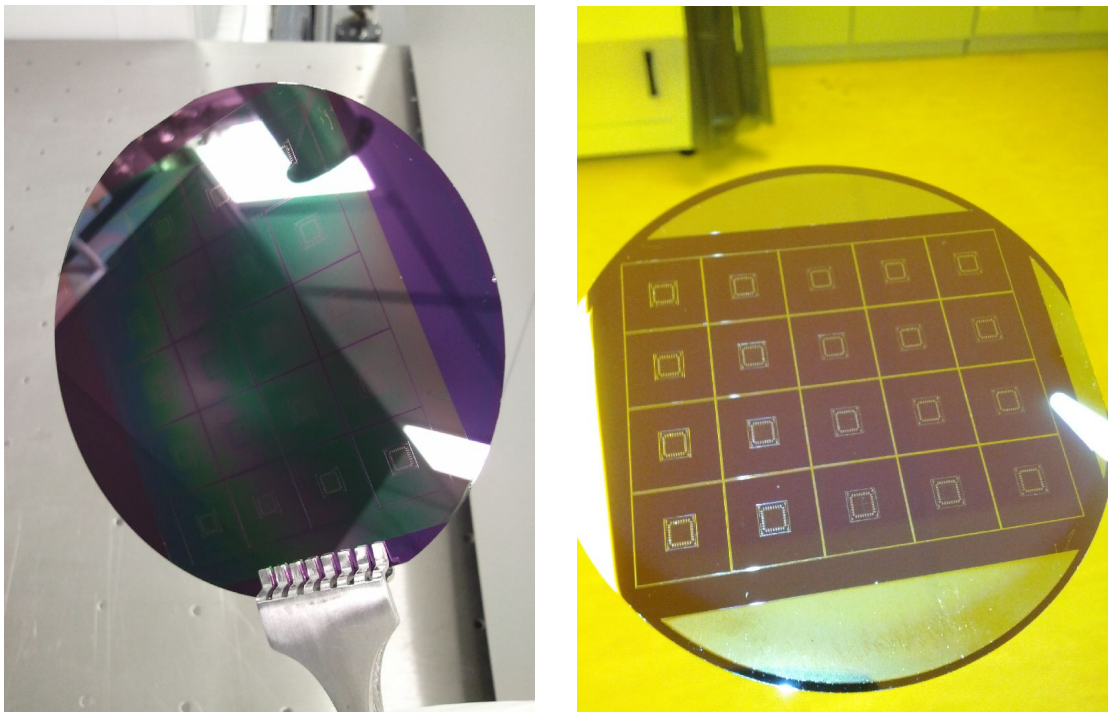

(a) (b)

Figure 3.4: (a) Image of the pattern from the photolithographic mask exposed and developed in the negative AZ2070 resist. (b) Image of the same wafer after metal evaporation and lift off processes.

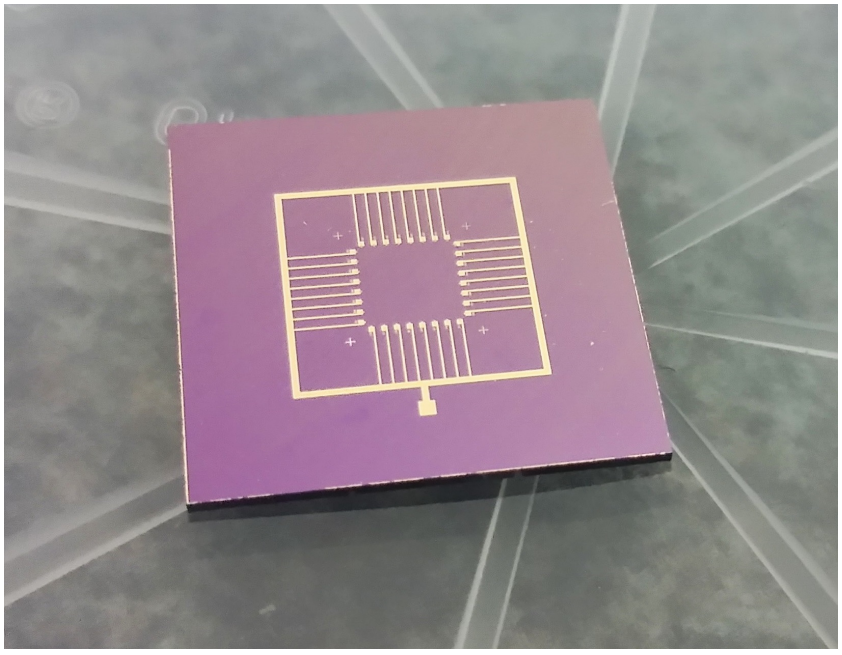

Figure 3.5: A single chip after the wafer was diced. The earthing ring and ESD via can be seen.

placed back in the dicer and the machine is programmed to only cut one third of the thickness of the wafer. The wafer is aligned in the dicer such that cuts can be made $5mm$ from each of the cuts in the previous run. This leaves some grooves on the backside of each chip which enable a much easier and more controlled method to break the chips down to the $5mm$ x $5mm$ size required to fit into the chip holders.

3.1.3 Example Device Design

Figure 3.6 (a) shows an example of a design for the lithography steps in fabricating a graphene PN junction device. The graphene flake is shown in grey after it has been etched into the desired shape. Ohmic contacts are shown in purple. Figure 3.6 (b) shows the locations of the top gates with a larger top gate covering half of the graphene flake which will be used to create the PN junction. It is expected that electrons entering the device from the ohmic contact on the right, labelled A, will have a divergent flow and a current should be measurable through all three ohmic contacts on the left labelled C, D and E. When the topgate is used to produce a symmetric PN junction, negative refraction will occur causing the beam to converge and increase the current through the central contact D whilst the current through C and E is reduced.

Figure 3.7 shows a schematic for a second device which uses the angular dependant transmission of a PNP junction to create a beam splitter. In the schematic the direction of current flow is shown in green, the ohmic contact in purple and the top gates forming PNP barriers are red. Following the path of an electron from input I_1 the electron first encounters PNP barrier formed by topgate A. This gate is tuned to allow only a narrow band of incident angles centred around 45° to transmit. All electrons with these incident angles are transmitted and all other electrons are reflected thus collimating the beam. The reflected electrons are

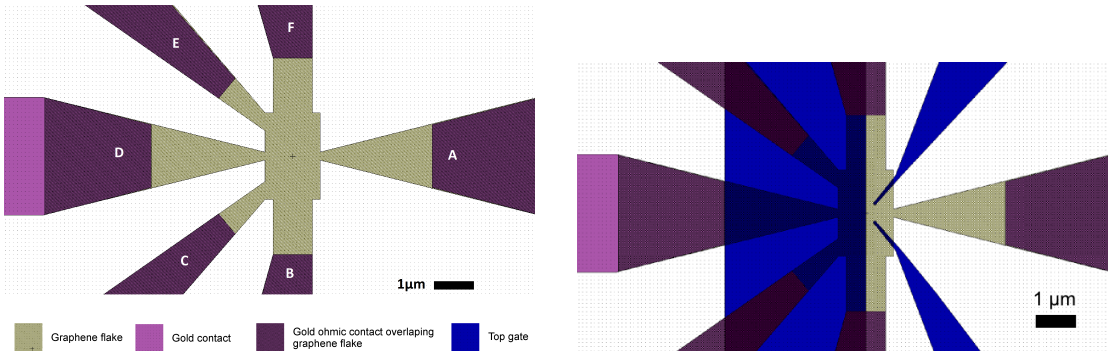

(a) (b)

Figure 3.6: (a) Example of the design of a device. Note that the graphene flake is shown after carving to define this shape. Natural graphene flakes tend to have more square or trapezoidal shapes. (b) as (a) but including the top gates. The larger top gate on the left forms the PN junction whilst the smaller finger like gates on the right are used to introduce a phase shift to each of the electron paths.

collected by the earth connections. Next the transmitted electrons reach the PNP barrier set by topgate B. This barrier is tuned to allow a 50% transmission and 50% reflection and acts a beam splitter for the electrons injected from either input I_1 or I_2. Barriers created by gates D and E are tuned to have as close to 100% reflection as possible to reflect the beams towards the last PNP barrier which is formed by gate F. This is set to also be a $50:50$ beam splitter.

In this configuration the device can be used as a Mach-Zender interferometer if just one of the inputs is used, or a Hong-Ou-Mandel experiment can be performed if just one of the beam splitters is used making this a very versatile device.

3.2 Layer Process

In order to minimise the number of scattering sites within the graphene devices a thick and flat layer of hBN is used as a substrate. The earlier samples were produced by stacking flakes of hBN and graphene using what is called the wet transfer technique. Graphene flakes are transferred on top of a hBN flake using an

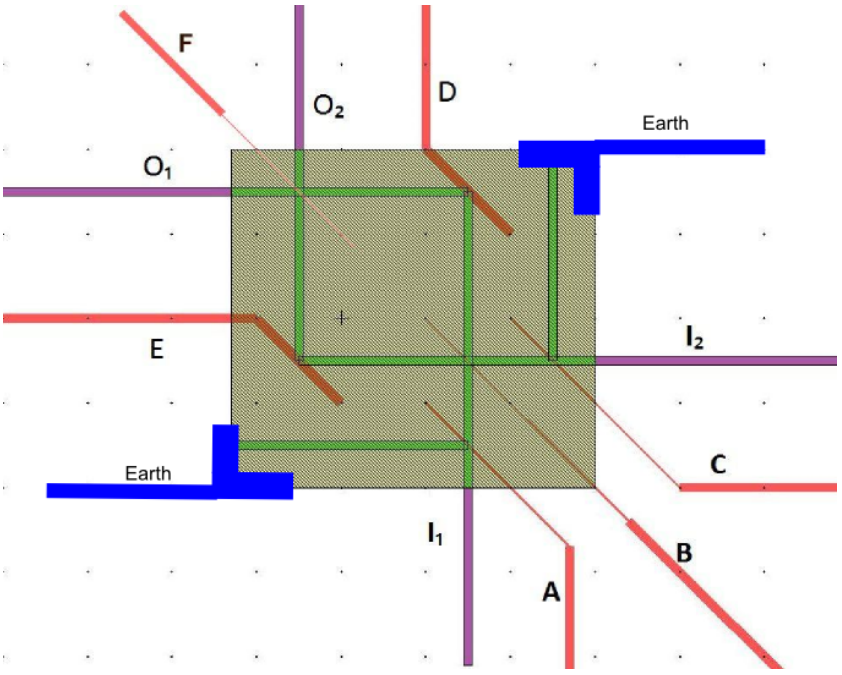

Figure 3.7: Device using thin top gates as 50/50 beam splitters and mirrors. Purple = Ohmic contacts, red = topgates, green = electron path and grey = graphene flake. Each topgate is tuned to produce the required reflectivity.

isolated thin film of PMMA as a carrier. This PMMA layer is then dissolved using acetone and the flake is then patterned using a combination of ebeam lithography and oxygen plasma ashing. It is contacted using ebeam lithography and metal evaporation and then a thin layer of hBN is transferred on top of the contacted device to provide a top dielectric for a topgate. The topgate is then fabricated using again ebeam lithography and metal evaporation. Figure 3.8 shows a microscope image of a trilayer graphene flake attached to a thin layer of free standing PMMA in both transmission (a) and reflection (b) modes.

Image analysis is used to identify the number of layers present. Figure 3.9 (a) shows a crop of Figure 3.8 (a) which was used to perform histogram analysis as shown in Figure 3.9 (b). It has been shown that graphene layers each have an optical absorption of 2.3% (52). By analysing the histogram of pixel intensities and comparing the peaks formed by the area with no graphene to the area with

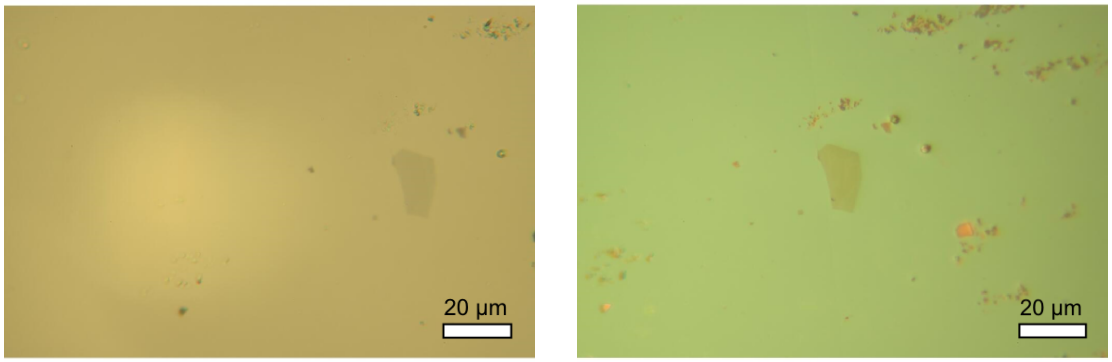

(a) (b)

Figure 3.8: (a) Transmission optical microscope image of the trilayer graphene flake on the PMMA support (b) Reflection microscope image of the same flake.

graphene we can get a fast accurate measure of the absorption of the graphene flake under examination. Figure 3.9 (b) shows the histogram which has been scaled in the x-axis for the background transmission to give a transmission of 93.1% for the flake or 6.9% opacity. This would be evidence of three layers each giving 2.3% opacity.

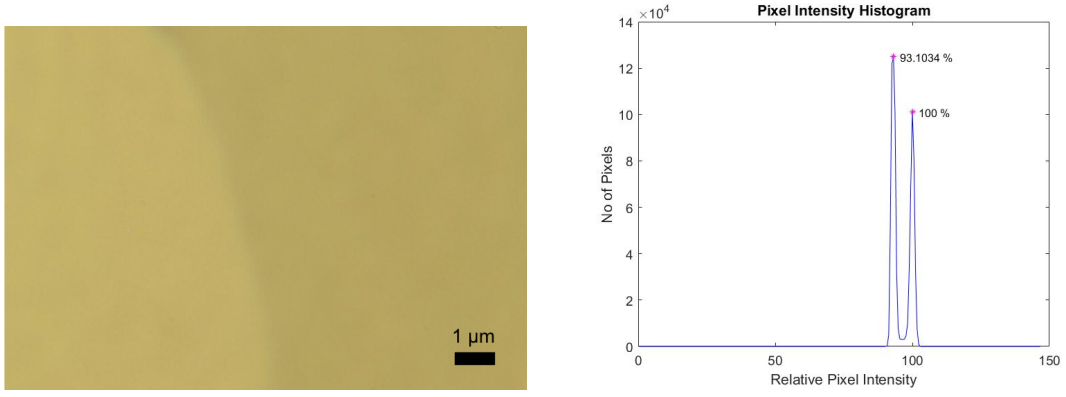

(a) (b)

Figure 3.9: (a) A section of the microscope image in Figure 3.8(a) used for layer identification. (b) Histogram for image (a).

A micromanipulator stage allows for an extra set of XYZ degrees of movement under a microscope to position the graphene flake on top of the hBN flake with a position accuracy of $\pm 1 \mu m$. Once a flake of graphene has been identified and

transferred onto the hBN base flake, it is checked for flatness using an AFM. Any bubbles which are found are removed by annealing the sample in a furnace with a flow of Ar/H_2 as described in Section 3.3. Figures 3.14 (a) & (b) show this process for another flake. Figure 3.10 (a) shows a microscope image of the hBN flake in yellow with the graphene flake on top of it in orange/red. A set of four marker crosses can be seen; these are used for alignment purposes throughout all e-beam procedures.

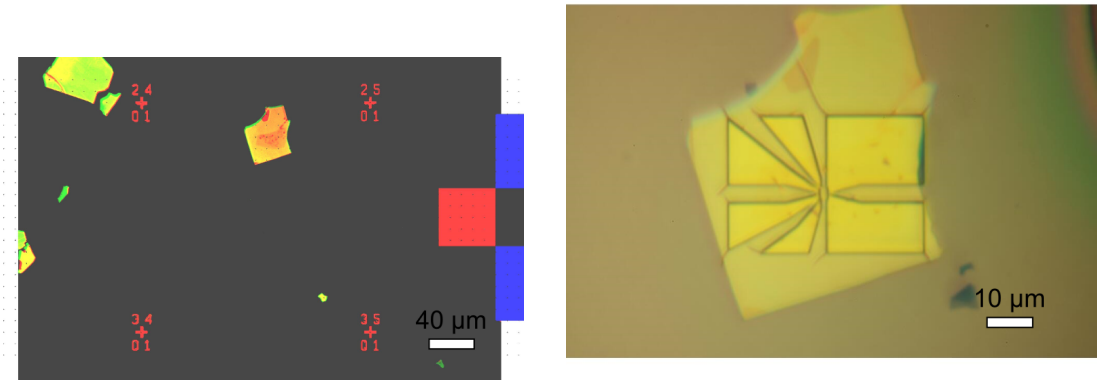

(a) (b)

Figure 3.10: (a) Enhanced contrast microscope image of a trilayer graphene flake on top of a multi layer hBN flake (b) Microscope image of e-beam pattern for plasma etching of the graphene flake.

A combination of e-beam lithography and oxygen plasma is used to etch isolation lines between the positions where ohmic contacts will be placed. Figure 3.10 (b) shows the region of PMMA which has been removed on top of the graphene flake allowing the oxygen plasma to etch away the pattern. With regular contrast the graphene flake is very difficult to see. Figure 3.11 (a) shows an enhanced contrast microscope image of the flake after plasma ashing. It clearly shows the new shape of the graphene flake in red on the yellow hBN flake.

Next e-beam lithography and evaporation is used to place the gold ohmic contacts on the graphene flake which are connected to wirebond pads ready for connection to a chip holder. Figure 3.11 (b) shows the e-beam pattern and Figure 3.12 (a) shows the gold contacts after the lift off process. Next a thin layer of hBN is

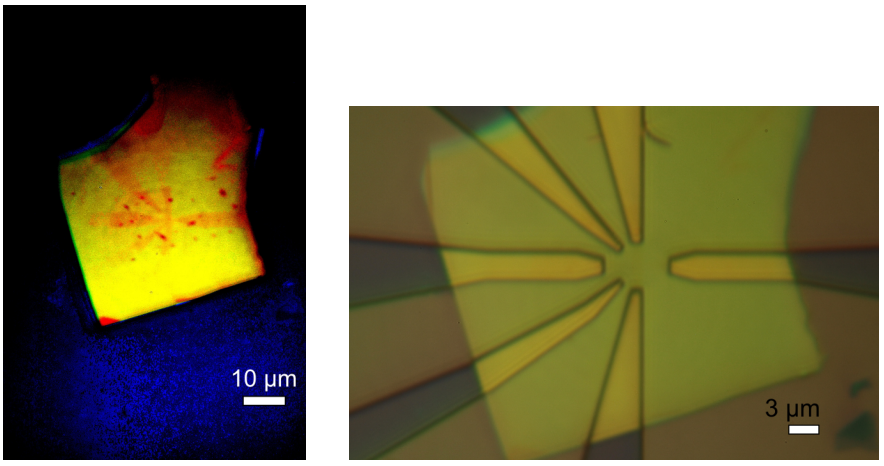

(a) (b)

Figure 3.11: (a) Enhanced contrast microscope image of a trilayer graphene flake on top of a multi layer hBN flake after carving (b) Microscope image of e-beam pattern for ohmic contacts.

identified and transferred on top of the device as shown in Figure 3.12 (b); the black line follows the edge of the hBN flake. This acts as a top layer dielectric onto which the top gates can be placed again using e-beam lithography and gold evaporation. Figure 3.13 shows the finished device with the inset showing a magnified image of the centre of the device.

Unfortunately it was not possible to make any electrical measurements of this device as the entire structure was snapped in half during a subsequent step necessary to fit the device into a sample holder for connection to the cryostat. For the subsequent batch of chips the pre-dicing depth was increased from $160\mu m$ to $210\mu m$ to ensure that the sample would snap correctly along the pre-designated lines.

Section 3.3 describes the resulting bubbles in the layers which were found by using this method of fabrication. Later a new method was found known as the dry transfer technique which did not result in bubbles at the interface of the layers. This is thought to demonstrate that the surfaces are atomically flat and clean as the bubbles are attributed to contamination on the surfaces.

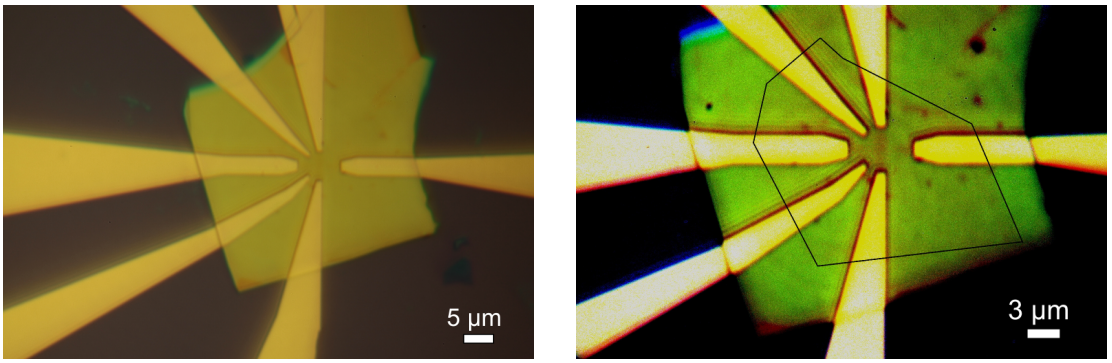

(a) (b)

Figure 3.12: (a) Microscope image of ohmic contacts after lift off (b) Enhanced contrast microscope image of hBN flake on top of graphene device. The black line indicates the edge of the top layer of hBN.

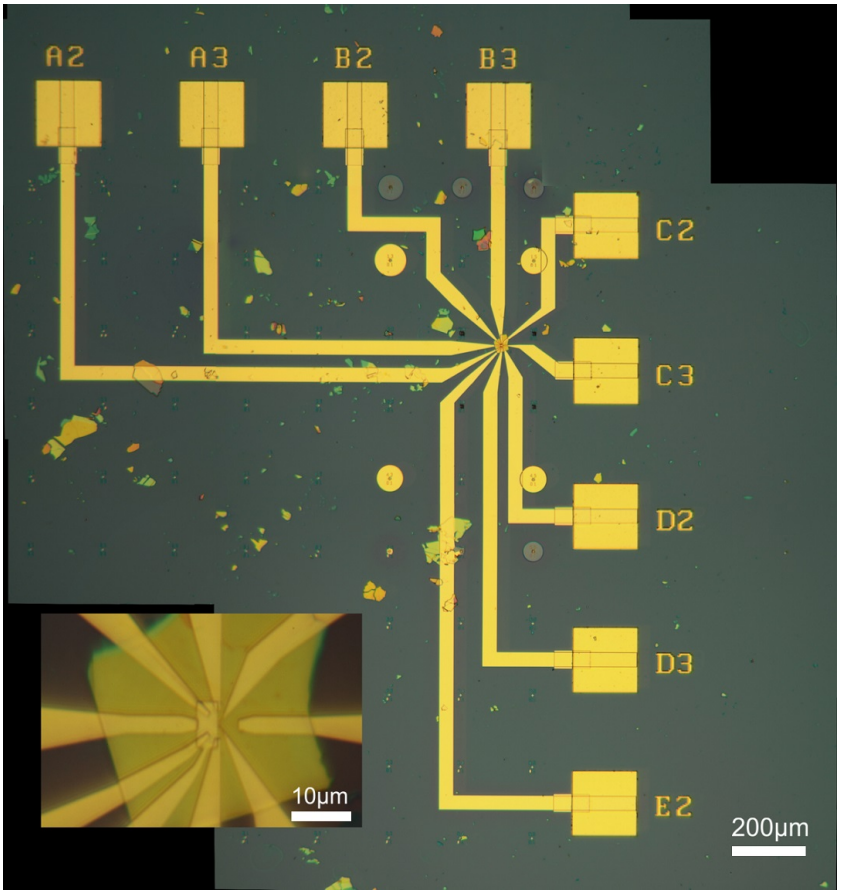

Figure 3.13: The finished sample including all ohmic and top gate connections. Inset - Magnified image of the centre of the device showing the top gate structure.

3.3 Bubbles and Their Removal

Bubbles under graphene flakes were reported by Stolyarova et al (38). Taychatanapat et al (53) made a point to carve away sections of graphene which had bubbles to leave just flat parts of graphene attached to the hBN surface. Bubbles seem to be more of a problem as we move to graphene on hBN flakes as they are not as pronounced or visible on an optical microscope when using SiO_2 as the substrate for the graphene flake. This may be because of the increased surface roughness of SiO_2 compared to hBN; a rougher surface gives more chance for there to be a gap through which gases can escape. Where as for graphene on hBN the surface is so flat that a good seal is formed between the graphene and hBN layers. Figure 3.14(a) shows an AFM image of a single layer of graphene on top of a hBN surface. Bubbles ranging in size from 100nm to 2μm can be seen with connecting tunnels between them.

The bubbles are a potential source of scattering sites for the charge carriers and thus a method to either avoid their creation or to facilitate their removal must be found. Any scattering sites within the area to be used for the device would alter the paths of the electrons and reduce the mobility accordingly. Possible ideas for prevention include performing the transfer in a vacuum, in an atmosphere of gas molecules which could permeate the graphene flake or applying a suitable tension to the flake during transfer in order to avoid the trapping of gas beneath the flake. Graphene is impermeable to all gases (25) and performing the transfer inside a vacuum presents many practical issues. However a method to remove the bubbles has been found involving heating the sample in a tube furnace to 250°C in an atmosphere of H_2 / Ar. Figure 3.14(b) shows the same area of the same flake as in 3.14(a) after being annealed. Clearly there is a reduction in bubbles and an increase in usable flat sections of the graphene flake. This makes the selection of a suitable area of graphene much easier however it does not remove the bubbles

completely and a better solution to the problem would be to remove the process by which the bubbles are formed as in the dry transfer method described in the next chapter.

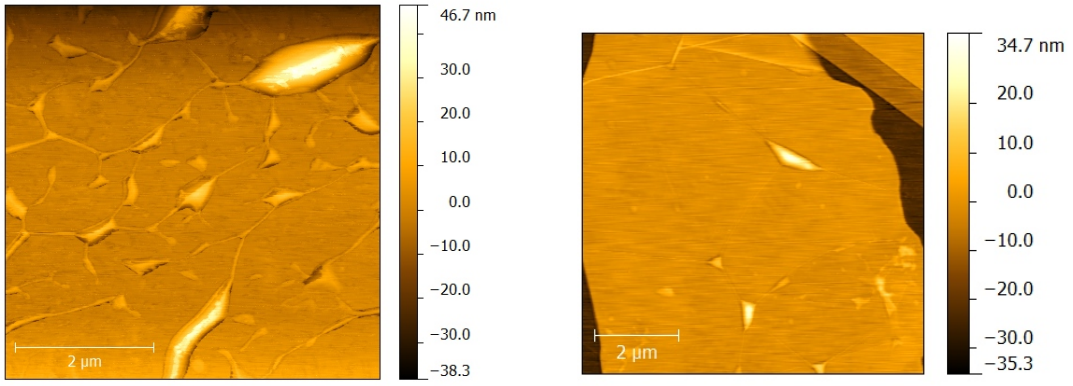

(a) (b)

Figure 3.14: (a) AFM image of graphene flake on top of BN. Many bubbles and wrinkles between the atomic layers can be seen with no clear path from left to right (b) AFM image of same area after annealing in H_2 / Ar at 250C. Much fewer bubbles remain with small wrinkles connecting them.

3.4 Dry Transfer Method and 1-Dimensional Contacts

Wang et al demonstrated a technique for creating the hBN-graphene-hBN stacks which avoids the surface contamination which is present in the previously described methods (33). It is thought that the contamination on the graphene surface of small parts of PMMA cause the bubbles between the layers. This method produces stacks which do not contain bubbles between their layers as it involves stacking the layers up to form the sandwich without any resist processes in between. The breakthrough in their paper comes in the one dimensional contacts formed by etching the stack and contacting the edge of the graphene flake which is exposed. This allows the stack to be formed first, the graphene flake encapsulated between the two hBN flakes and then the contamination producing steps of shaping and

contacting the flake can be completed. Previous stacks were encapsulated with the top layer of hBN after the shaping and contacting of the graphene flake which would often leave trace amounts of PMMA or other residues on the graphene surface which resulted in the bubbles reported. This method of stacking, etching and contacting the edges was used in the final five samples made.

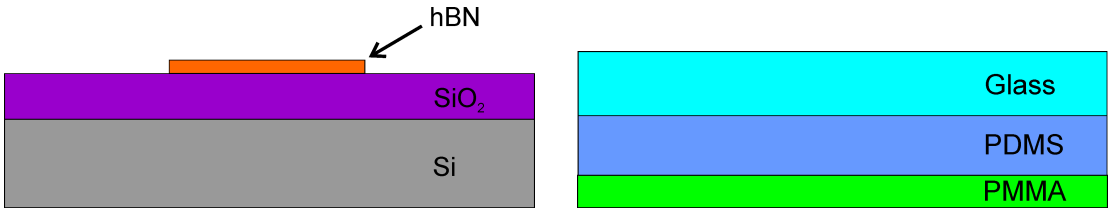

(a) (b)

Figure 3.15: (a) The few layer hBN flake is exfoliated onto the SiO_2 surface. This will become the top of the sandwich. (b) A glass slide is prepared with $1\mu m$ PDMS and $500nm$ PMMA.

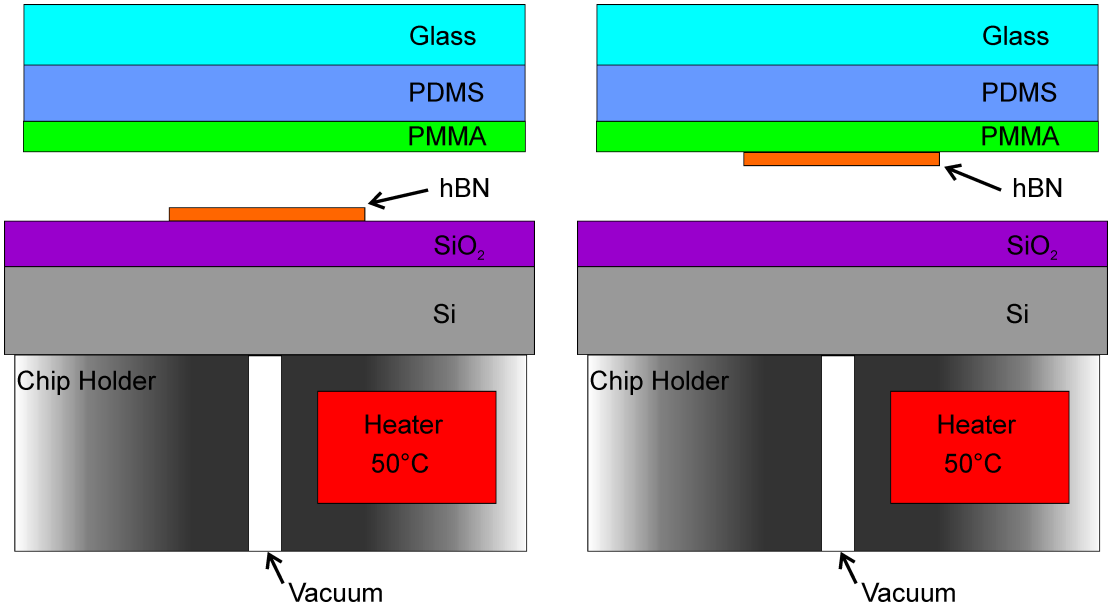

(a) (b)

Figure 3.16: (a) The chip with hBN flake is placed on the chip holder on the microscope, held in place with a vacuum applied through a channel in the chip holder. The glass slide is clamped in the micro manipulator above it, PMMA side down. (b) With the heating element set to $50°C$ the slide is brought into contact with the hBN flake and then lifted.

The transfer process involves several steps as follows:

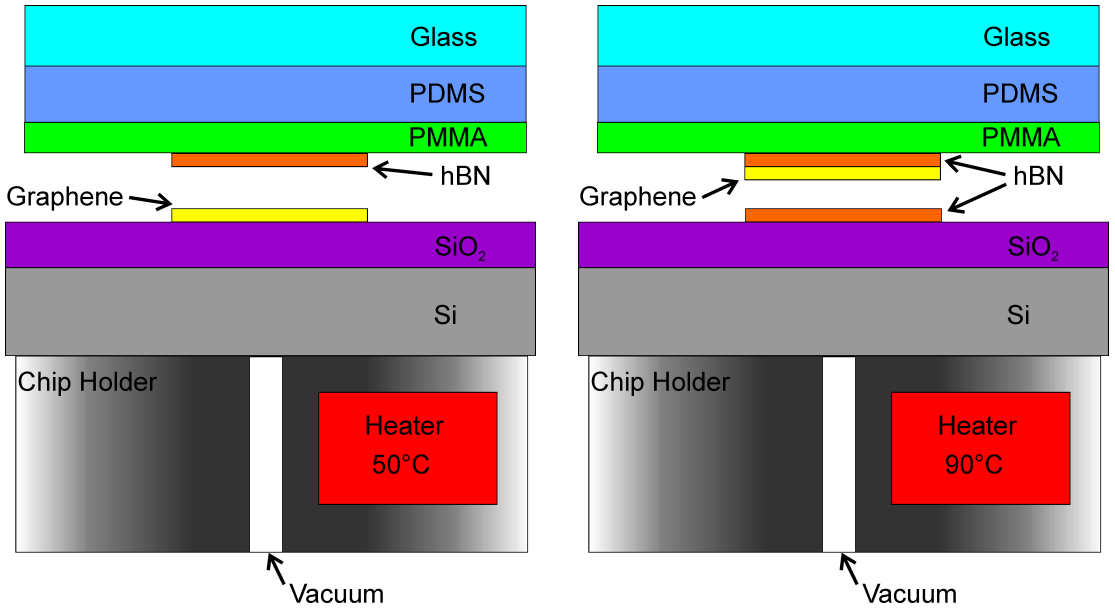

Figure 3.17: (a) A new chip with an identified graphene flake is placed on the chip holder and the two flakes are aligned. (b) The contacting process is repeated and the graphene flake is lifted from the SiO_2 surface to the hBN surface, the last chip with another hBN flake is placed on the chip holder.

- Exfoliate and identify graphene flakes and hBN flakes on separate 300nm SiO_2 chips. Figure 3.15(a).
- Prepare microscope slides with a 1mm thick layer of PDMS and then spin coat with $\sim 500nm$ PMMA. Figure 3.15(b).
- Place the chip containing the hBN flake onto the transfer microscope stage and turn on the vacuum to hold it in place. Figure 3.16(a).
- Locate the prepared transfer slide into the clamp on the microscope with the PMMA layer facing down towards the chip.
- Apply heat to the chip via the heater wrapped around the stage post, heat to 50°C.
- Focus the microscope on the chip and find the preselected hBN flake.

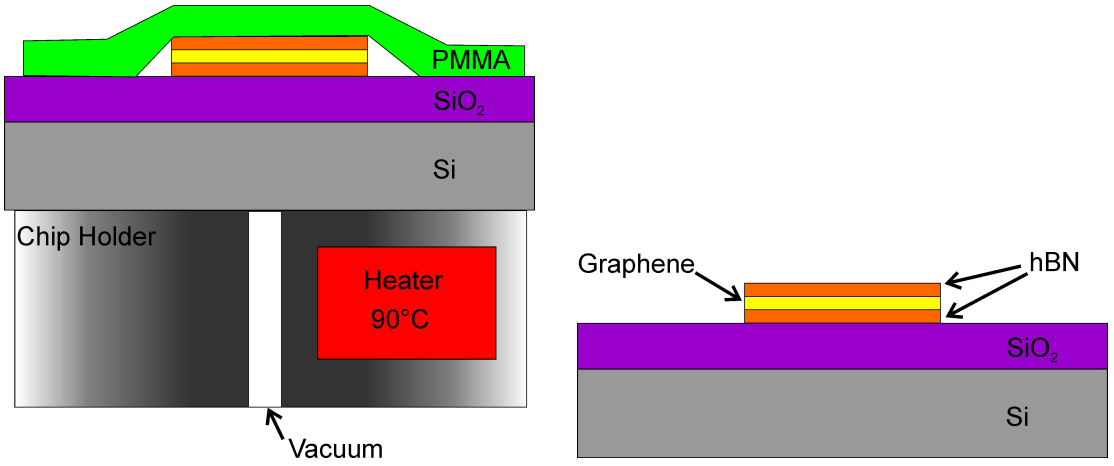

(a) (b)

Figure 3.18: (a) As the stack is aligned and contacted with the last hBN flake the heating element is set to $90°C$ and the slide is raised to separate the PMMA from the PDMS. (b) The PMMA is removed by dissolving in acetone, the graphene surfaces are protected by the hBN sandwich.

- Lower the transfer slide down towards the chip until contact is made and apply a small amount of pressure.

- Slowly raise the transfer slide up and watch the hBN flake, it should now be stuck to the PMMA of the transfer slide and removed from the SiO_2 chip. Figure 3.16(b).

- Replace the SiO_2 chip with the one with a preselected graphene flake. Figure 3.17(a).

- Locate the graphene flake and also the hBN flake, position the chip using the XY adjustment so that the two flakes are aligned. By moving the whole stage up and down the focus can be changed from the chip to the transfer slide.

- Slowly lower the transfer slide down towards the chip, stopping to check the alignment of the two flakes before contact is made.

- When alignment of the flakes is satisfactory lower the transfer slide by the last few μm to make contact and apply a small amount of pressure.

- Slowly raise the transfer slide, again watching the flakes to see that the graphene flake is lifted with the hBN flake. Figure 3.17(b).
- This stack can now be transferred to a preselected hBN flake on a prepared sample chip which includes grid markers, bond pads and earthing ring.
- The stack is dropped rather than picked up at the last step by raising the temperature of the chip to 90°C. This also separates the PMMA layer from the PDMS layer. Figure 3.18(a).
- The PMMA can then be removed using acetone and isopropanol leaving the hBN-graphene-hBN sandwich on the chip with the graphene surface protected from any contamination by the encapsulation from the hBN flakes. Figure 3.18(b).

Images are then taken of the stack which are used to design the carving and gold deposition areas. Care must be taken to avoid the gold from contacting areas of unprotected graphene or edges after carving which are not intended to be contacted electrically. The flake is etched to expose the edge of the graphene flake between the hBN layers and then chrome and gold is deposited so as to contact that edge thus forming a 1 dimensional contact.

3.5 Wire Bonding

As the intended electrical measurements are to be taken at low temperatures the chip must be wire bonded to a chip holder in order that the device can be connected from the cryostat to the Parameter analyser.

The chips are glued into place on a chip holder using silver paint which is known to work at cryogenic temperatures and forms the contact for the back gate. The

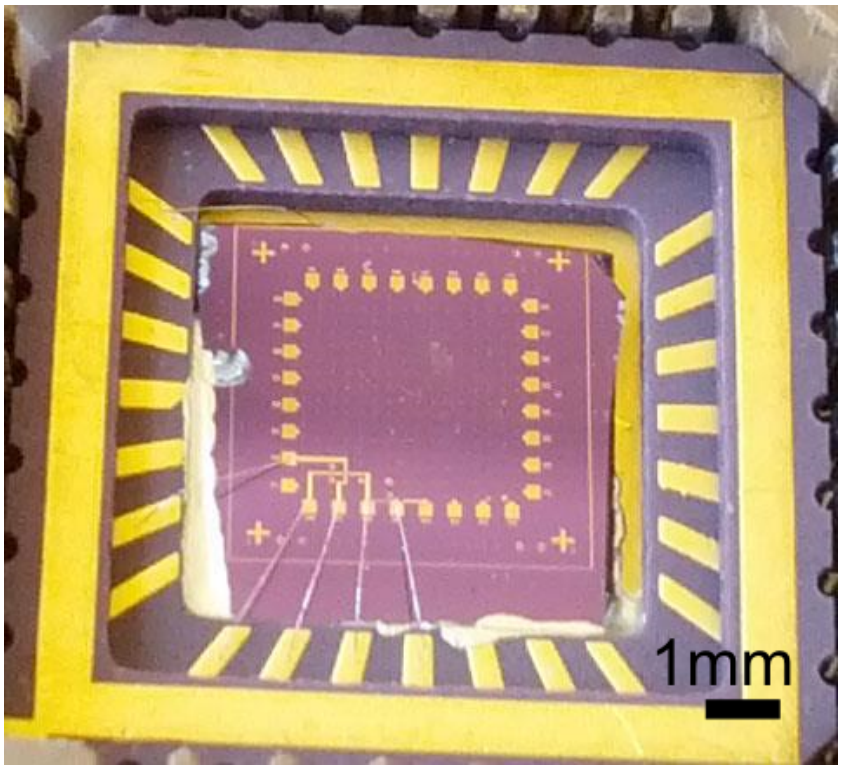

Figure 3.19: A sample which has been wire bonded to a chip holder. The chip is secured to the chip holder with silver paste. 5 bond pads are connected on this sample and one wire is connected to the baseplate of the chip holder to form the backgate.

wire bonder used was a wedge bonder type which functions by using a crushing force and piezo activated sonication to bond the silver bond wire to the gold contact pads. Figure 3.19 shows a sample which has been bonded into a sample holder, shown is one of the earlier chips which does not include the earthing ring as described in Section 3.6. In the image the gold contact lines fabricated through lithography connecting the pads to the graphene flake can be seen. Five silver wires are each bonded between the pads on the chip to the nearest pads on the chip holder. Also at the top of the image a sixth wire can be seen to bond between the gold under the chip to another pad on the chip holder, this facilitates the application of a back gate voltage.

There were two issues found with using the wire bonder. Firstly it was found that many devices were damaged at the wire bonding process, wherein a reasonable

resistance was measured before the bonding and an open circuit was measured after the bonding. Further investigation of the affected devices after bonding using a scanning electron microscope indicated that the graphene flakes had broken between the metal contacts and that the metal contacts in the region of contact had melted due to heat. A logical explanation for the damage is electrostatic discharge through the device. Subsequently an anti static wrist band was used for all future wire bondings and great care was taken to ensure that tweezers were grounded before contact with the chip and that all parts of the bonder were earthed correctly. These steps significantly reduced the occurrence of electrostatic damage to the samples.

Secondly when bonding the large pads on the chips to the pads on the chip holder it was found that some of the pads on the earlier chips would break and disconnect from the chip surface. It is thought that this issue is caused by the conditions of the evaporation of the gold in the pads, newer chips were fabricated by ensuring that evaporation is made swiftly after the pattern is developed in order that no contaminants are able to adsorb onto the SiO_2 surface before the gold is evaporated.

3.6 Backgate Leakage

In order for the required measurements to be taken the backgate connection must be isolated from all other connections on the device. This allows a field to be applied from the back of the device without a current flow to disturb the other measurement. The backgate is realised by using highly doped Silicon wafers with a $290nm$ thick SiO_2 top layer to isolate the graphene device and its required connections from the backside. The backgate voltage can then be applied directly

to the highly doped Silicon which will then capacitively couple to the graphene device through the SiO_2 layer.

A leak of charge transferring from the backgate through to the other parts of the device would obviously cause a problem with the electrical measurements.

During any electrical measurements on the graphene devices the current leakage through the backgate was monitored. It was found on many of the devices fabricated that leakage occurred. It was found that the resistance between the backgate and the wirebonded contacts was as low as 200Ω. To put this value into perspective, for a fully isolated connection the resistance can be as much as $1G\Omega$ and the resistance of some basic graphene devices fabricated by David Hempston from source to drain was $2 - 3k\Omega$.

The possible sources of a current leak from the backgate are:

- a short circuit contact within the wiring of the cryostat insert.
- a short circuit contact between wirebond wires on the chip.
- a break down of the dielectric function of the insulating SiO_2.

The wiring of the cryostat insert was checked for resistance between the relevant contacts and found to be satisfactory. A visual inspection of the chips after wirebonding was performed for each chip to ensure that none of the wires contacted each other. This left the break down of the SiO_2 layer. Many of the steps in the fabrication have the potential to cause damage to the insulating layer through two methods of failure. Either from the sonication used during wirebinding or from an electrostatic discharge through the dielectric. A chip from the same fabrication batch as the failed samples was used to test the wirebonding process. 21 of the 28 bond pads were wirebonded using varying settings on the wirebonder including those used on previous samples. The resistance was then measured between each

bond pad and the backgate to check for any damage of the insulating layer. All resistances measured above $1G\Omega$ revealing that the wirebonder is not the source of the damage.

Electrostatic discharge (ESD) through the dielectric can result from a build up of charge on the isolated device. Although an ESD wrist strap was used when handling the device for wirebonding and for insertion into the cryostat it is not practical to wear ESD wrist strap protection at all times whilst handling the device, especially as it has to be transported from building to building between process steps. A design was required for the chips which enabled all of the contacts to be short circuited together and to the backgate until measurements were to be made. This allows all parts of the device to be at the same potential at all times and thus prevent a build up of charge.

The chip design includes connection lines between each wirebond pad and an earth ring, which each cross over the boundary at which the chip will be cleaved before measurements. Thus enabling the connections to be broken at the last step. Also the earth ring includes a connection to the backgate facilitated by etching a section of the SiO_2 through to the Silicon thus creating a relatively low resistance contact to the backgate which stops the build up of charge and subsequent fast discharge through the dielectric which causes damage. The resistance of the partially etched SiO_2 was measured to be in the range of $1M\Omega$ which is in line with standard specifications for ESD protection as it allows the charge to dissipate slowly thus causing less damage to the device. Figure 3.20 shows the chip design including the earth ring in green and the etched "via" through to the backgate in black. The grey lines show the cleaving lines which leave a $5mm$ square chip to fit into the chip holder for wirebonding and which intersect the connections from the bond pads to the earth ring.

Devices which were made using this new design of chip did not suffer from backgate

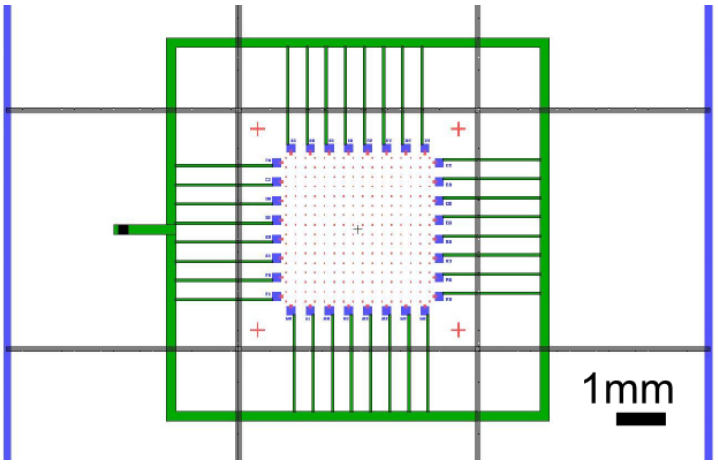

Figure 3.20: An image of the design for the chips including ESD protection. The blue wirebond pads and red alignment markers are the same as the previous chips. The earth ring is shown in green with the black square to the right of the image representing the via connection to the highly doped Silicon backgate. Grey lines show where the chip is cleaved immediately prior to electrical measurements.

leakage. Although other methods of failure were present such as physical damage during the chip cleaving process before wirebonding as happened to the device depicted in Figure 3.13. Another method of failure was non-conductive ohmic contacts which is thought to occur when the resist is not fully removed during the development stage before metal evaporation. In the early stages of the PhD there were also issues with incomplete lift-off of the sacrificial metals which was due to sub-optimal resist spinning and e-beam settings causing the metal to stick to the walls of the resist. With experience more optimised settings were use with a dual layer resist and appropriate e-beam settings to produce an overhang in the patterned resist to aid in the removal of the sacrificial metals.

3.7 He Ion Carving

Earlier samples were made into shapes which would facilitate the fabrication of a QPC within the graphene flake. This was made by carving a small constriction

in the graphene leaving two isolated side gates which could be used to influence the transport through the constriction. Simulations of the devices indicated that the constriction would need to be on the order of $\sim 10nm$ which is smaller than is possible with the standard carving techniques using e-beam patterning and plasma ash carving. Instead a new technique was used which involves the helium ion microscope, with the beam at a high enough dose the helium ions remove the carbon atoms in the graphene and by moving the beam a pattern can be carved into the graphene flake with a minimum feature size of $\sim 1nm$. Once a flake of graphene had been identified it was electrically contacted using standard e-beam lithography and lift off techniques. The quality of the electrical contacts was checked using a simple DC I-V measurement to determine its resistance. If the resistance was satisfactory, i.e. below 3kΩ, then a structure was carved between the contacts to form the QPC. The Carl Zeiss Orion is a He ion scanning microscope designed to image feature sizes beyond the capabilities of the scanning electron microscope. The larger mass of the He ions when compared to electrons means that the He ions have a smaller de Broglie wavelength and therefore are able to resolve smaller objects. It has been shown that bombardment of a high dose of He ions on to graphene flakes will carve through the graphene (54) (55). Graphene flakes have been carved using the He ion beam using the pattern shown in Figures 3.21 (a) and (b). In the image the source-drain contacts are on the left and right and the side gates are on the top and bottom.

3.8 Low Temperature Measurement Setup

A liquid helium cryostat is used to make low temperature electrical measurements of the devices. Figure 3.22 shows the cryostat and the various electrical connections and gas connections. The cryostat is capable of sustaining sample temperatures

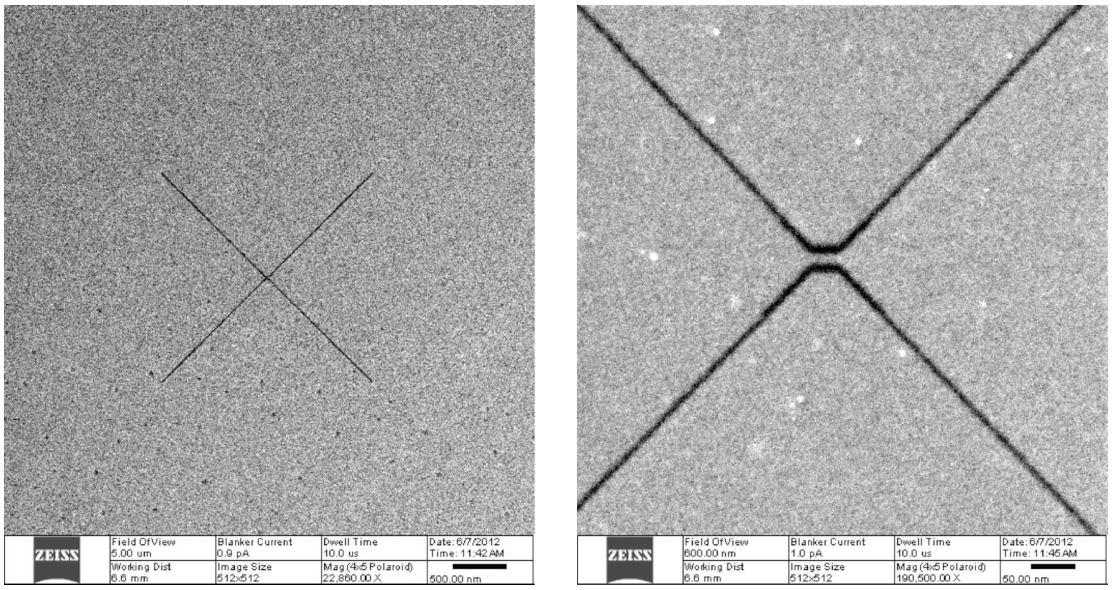

(a) (b)

Figure 3.21: Structure carved into SiO_2 surface to test that the dimensions of the pattern were correct. The constriction was intended to be $\approx$ 10nm and was measured to be $\approx$ 8nm.

from 300K to 4.2K which is achieved by evaporating liquid helium over the sample space and the use of a heater connected to PID control to stabilise the cooling effect. The cryostat also includes a superconducting magnet which is capable of a maximum field of 10T in either direction perpendicular to the sample plane and can be set to increments of 0.1 gauss.

3.8.1 Cryostat Cool Down

The cool down of the cryostat is a time consuming process which involves many critical steps in preparing the many cryogenic and vacuum spaces internal to the cryostat. Within the cryostat there are many separate concentric volumes of space including, starting at the outer layer, an outer vacuum space, a liquid nitrogen space, a liquid helium space, a further vacuum space which separates the most inner sample space from the liquid helium space. The superconducting magnet sits within the liquid helium space and so when fully operational is cooled to 4.2K.

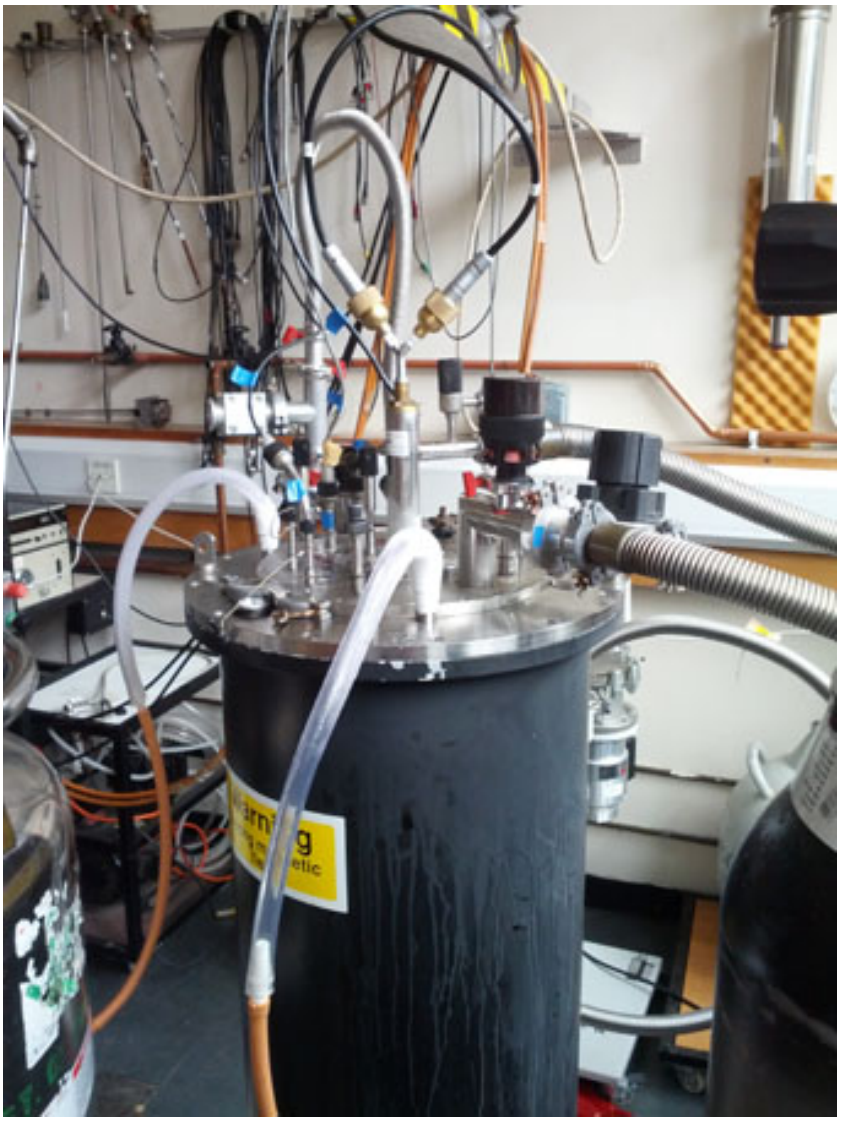

Figure 3.22: The liquid helium cryostat used for low temperature measurements. Temperatures of between 300K and 4.2K are achieved via the combination of the evaporation of liquid helium and a resistive heater in the sample space. Also included is a superconducting magnet capable of 10T in steps of 0.1 gauss.

The outer and inner vacuum spaces are evacuated using a turbo pump down to 10^{-6} mbar and it is essential that this pressure is reached before any cooling work commences. The first stage of cool down involves filling the liquid helium space with liquid nitrogen to pre cool the space and the large mass of the magnet down to 77K. This pre cooling is done using liquid nitrogen because it is much cheaper than liquid helium and also nitrogen has a much larger cooling power per litre

than helium due to its larger latent heat of evaporation. The temperature of the magnet is monitored via its resistance which declines rapidly as it is cooled down. Once the helium space and magnet are cooled to 77K the nitrogen is transferred into the nitrogen space by use of a back pressure applied from a nitrogen gas cylinder. This nitrogen space is then topped up to full and this space is kept full for the duration of the use of the cryostat. This is important as the nitrogen acts as a radiation barrier to the liquid helium. Without the nitrogen surrounding the it the liquid helium would evaporate very rapidly.

With the helium space at 77K it is now required to completely remove all liquid and gas nitrogen from the space as any remaining nitrogen would freeze as soon as liquid helium is introduced to the system and would lock up essential valves in the cryostat. This nitrogen removal is achieved by a careful procedure which involves filling the space with helium gas and pumping the space down to the 100 mbar range, this process is repeated many times achieving lower and lower base vacuums until it is better than 1 mbar. Once the space is cleared of nitrogen and contains only helium gas the transfer of liquid helium can commence. A special double walled vacuum protected transfer line is used so that the liquid helium does not evaporate as it is being transferred from the dewar to the cryostat. A small back pressure is applied via a helium gas cylinder to aid the transfer. The resistance of the magnet is monitored as the liquid helium is transferred, as the magnet cools down to 4.2K the resistance falls to 0.1Ω. Once the resistance of the magnet shows that the main mass of the magnet has cooled to 4.2K the rate of the transfer of liquid helium is increased by applying slightly more back pressure. The helium level meter is then monitored as the liquid helium level rises up to make contact with the long sensor. The level meter works by measuring the resistance of a straight 1m long superconducting wire which extends down into the helium space. As the level of the cryogenic liquid rises it submerges more of the superconducting wire and therefore more of the wires length has no measurable resistance and the

remaining resistive length decreases therefore decreasing the measured resistance. Once full the transfer is stopped by removing the back pressure, the transfer line is removed and all access holes are plugged.

The helium space is connected to a return line for two reasons, 1) the liquid evaporates producing a large volume of gas at all times, if the space was sealed the pressure would increase to explosive levels 2) the gas is very expensive and we are lucky in our department to have the facility of a liquefier to recycle the gas back into liquid helium thus it is collected via the return line back to the liquefiers gas store.

3.8.2 Cryostat Use

Once the filling is completed and the cryostat is full of liquid helium and nitrogen it is now possible to set up the cooling of the sample space. This is achieved by using a vacuum pump on the sample space and opening the needle valve which separates the sample space from the liquid helium. This allows some liquid through to the sample space which immediately evaporates. The rate at which the liquid helium is evaporated over the sample affects the cooling power of the system. To achieve a constant temperature on the sample this cooling rate is controlled by balancing the low pressure of the sample space via some valves by the pump, the amount that the needle valve is opened and also the power supplied to a heating element inside the sample space which is connected to a PID controller.

An Agilent 4155C Parameter Analyser is used to take electrical measurements which is capable of applying DC voltages of $\pm 100V$ in steps of $100\mu V$ and recording DC currents with a resolution of $100fA$. The temperature controllers, Parameter Analyser, magnet power supply and liquid helium level units are all controlled and data recorded using a Labview program. This enables sweeps to be automated

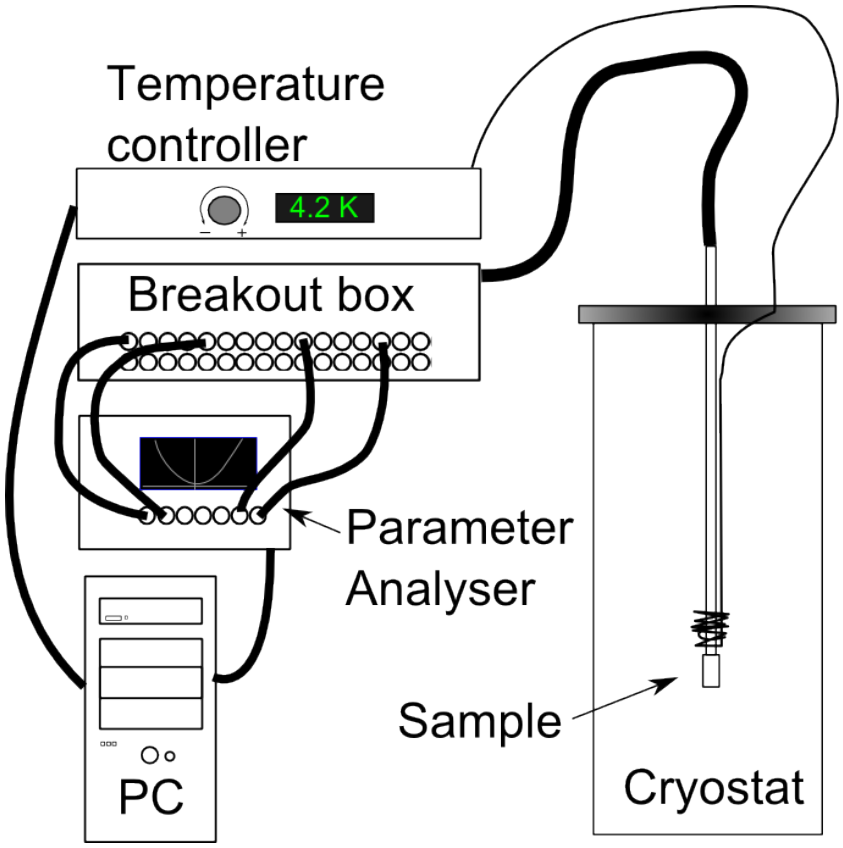

Figure 3.23: A schematic of the equipment used when taking low temperature measurements.

with steps in the source-drain voltage, gate voltages and magnetic field whilst the temperature and helium level are monitored. Figures 3.23 and 3.24 show how these pieces of equipment are interconnected. A breakout box allows electrical connections to be made to the many different contact pads at the sample chip, which gives the necessary flexibility in arranging a measurement.

3.9 Graphene on hBN

A device was made with a flake of graphene on top of a flake of hBN. Two gold contacts were fabricated on the graphene with a gap between them of $2\mu m$. Figure 3.25 shows an optical micrograph of the device.

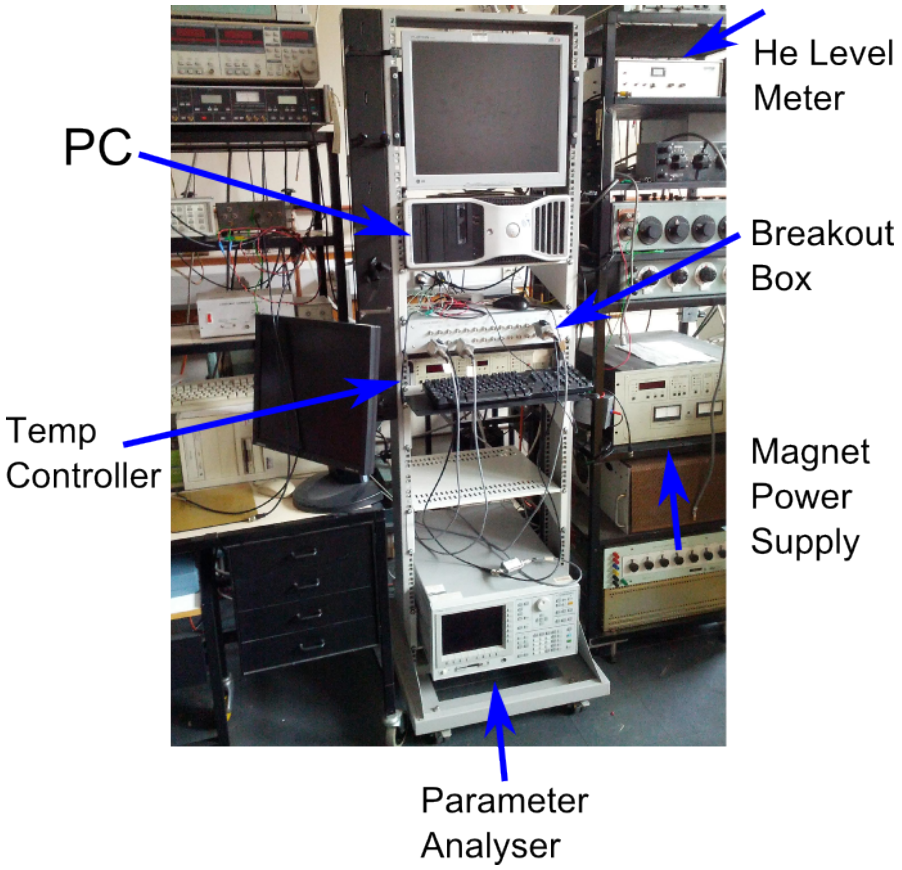

Figure 3.24: A photograph of the equipment used when taking low temperature measurements.

Figure 3.26 shows the results of successive back gate voltage sweeps on the device using a probestation to contact to the gold pads. These measurements were performed at room temperature and pressure. It can be seen that initially the charge neutrality point is close to $0V$ indicating little overall doping, however with successive sweeps of the back gate the CNP moves more negative away from $0V$ and as it does so the gradient of the slope decreases. This indicates that the charge carrier mobility is decreasing with successive sweeps. These measurements were taken one after another, approximately 1 minute between sweeps in the order dictated by the arrow in the figure. It is unclear at this time what the exact cause of this effect is although it is hypothesised that some contaminants on the surface of the graphene were evaporated or burned from the surface. However as this measurement was performed in air the device may have started to oxidise.

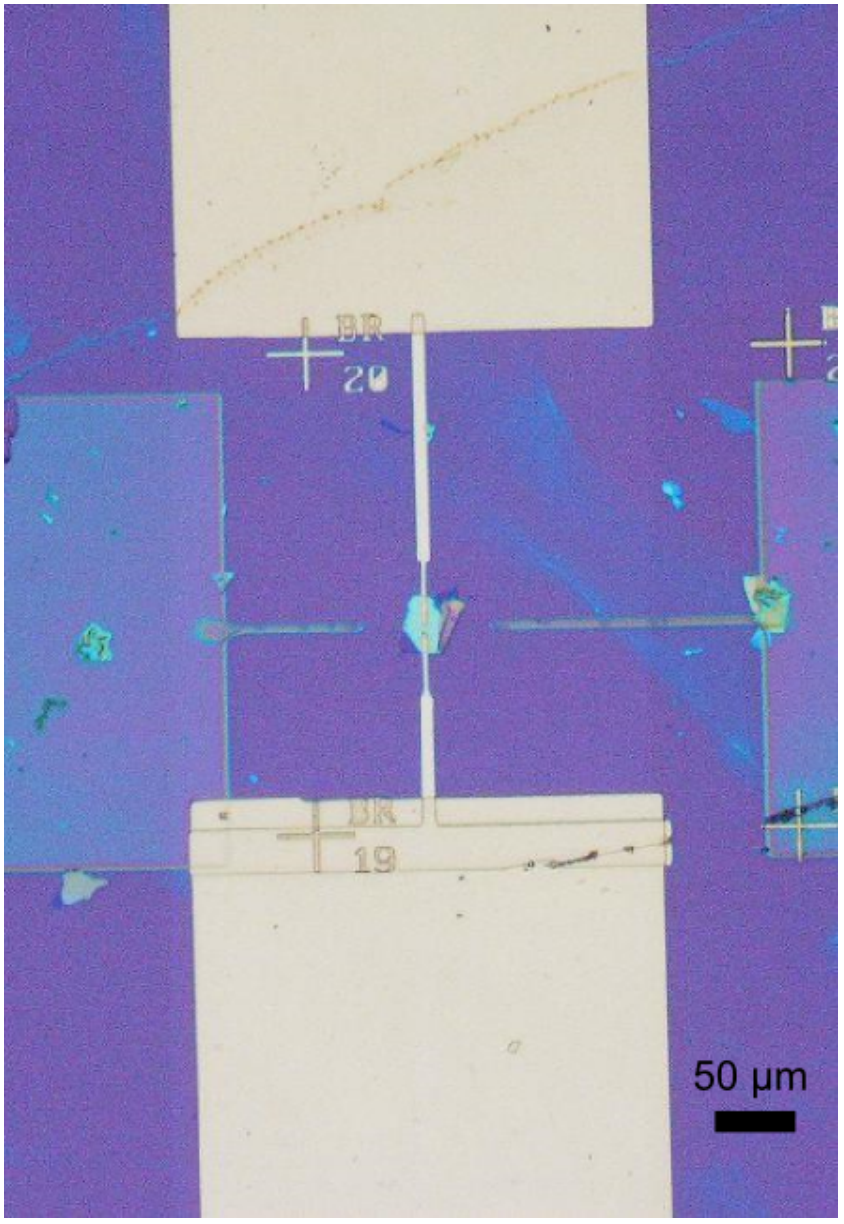

Figure 3.25: Sample 1T: graphene flake on hBN flake with two metal contacts. This was an early attempt at graphene flake transfer and electrical contacts, as such contamination from previous attempts at patterning of PMMA can be seen.

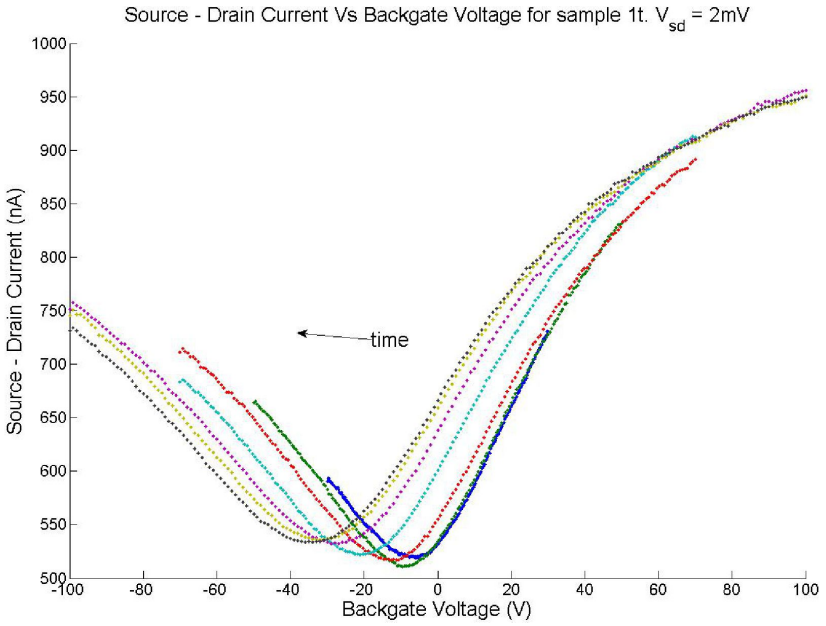

Figure 3.26: Source-Drain current for sample 1T as measured with a varying back gate voltage. Source-Drain voltage was set to $2mV$. Measurements were taken in succession, 1 minute apart, the order of which is given by the arrow. T = 298K & B = 0T

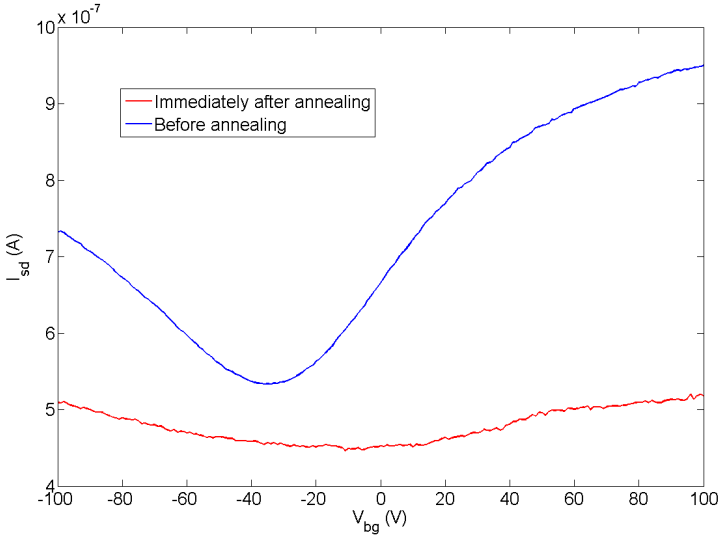

Figure 3.27: Source-Drain current for sample 1T as measured with a varying back gate voltage before and after annealing. Source-Drain voltage was set to $2mV$. T = 298K & B = 0T

The device was then annealed in a carbon nanotube furnace in a mixture of argon and hydrogen gases at 300 °C for 1 hour. After cooling to below 60 °C the device was removed from the furnace and was again measured on the probe station, Figure 3.27 shows the results of this measurement. As can be seen the current is significantly reduced after annealing as is the the gradient of the slopes indicating an increase in scattering. The annealing was performed as it was reported that this would improve the conduction of the sample, possibly due to removal of surface contaminants and also a slight relaxing of the graphene lattice with respect to the hBN lattice. However the post annealed device performed much worse that pre annealed. There are two possible explanations to this; firstly it could be that the temperature during the anneal process was too high which damaged the crystalline structure of the graphene flake. Secondly it could be that the device was hotter than the 60 °C shown on the furnace temperature gauge when it was removed and when exposed to the oxygen in the air would have oxidised the carbon (56).

3.9.1 QPC and Test Sample in Cryostat

The sample shown in Figure 3.28 and another one prepared in the same manner and subsequently carved using the pattern shown in Figure 3.21 were tested at low temperatures. Due to complications in the set up of the liquid helium cryostat these measurements were taken with the samples dipped into a dewar of liquid helium. The samples were wire bonded and the chip holder inserted into the cryostat dipstick. The dipstick was slowly lowered into the liquid helium dewar and thus the samples were in direct contact with the cryogenic liquid at $4.2K$ as measured on the temperature sensor fitted to the dipstick.

A series of back gate sweeps were performed using two opposite contacts as a source and drain with various source-drain voltages. Figure 3.29 shows eight of

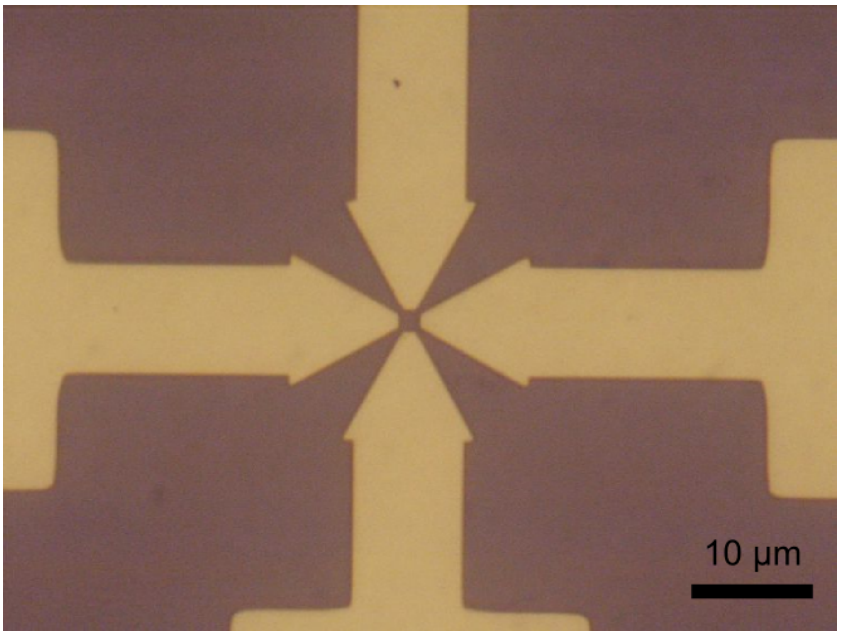

Figure 3.28: Optical micrograph of a graphene flake on SiO_2 contacted with gold. The gap between two opposite contacts is $2\mu m$.

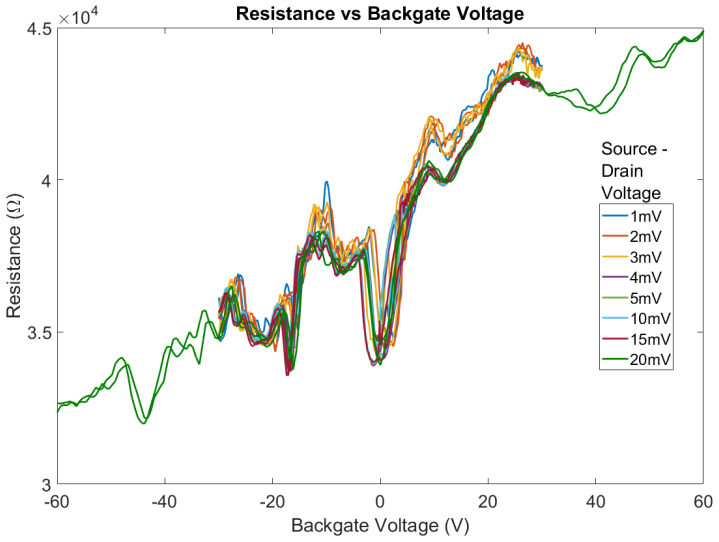

Figure 3.29: Source-Drain current vs back gate voltage sweeps for sample shown in 3.28.

these sweeps, converted into the resistance of the sample as this normalises the differing source-drain currents caused by the various source-drain voltages.

The expected outcome of this measurement would be one single peak at the charge

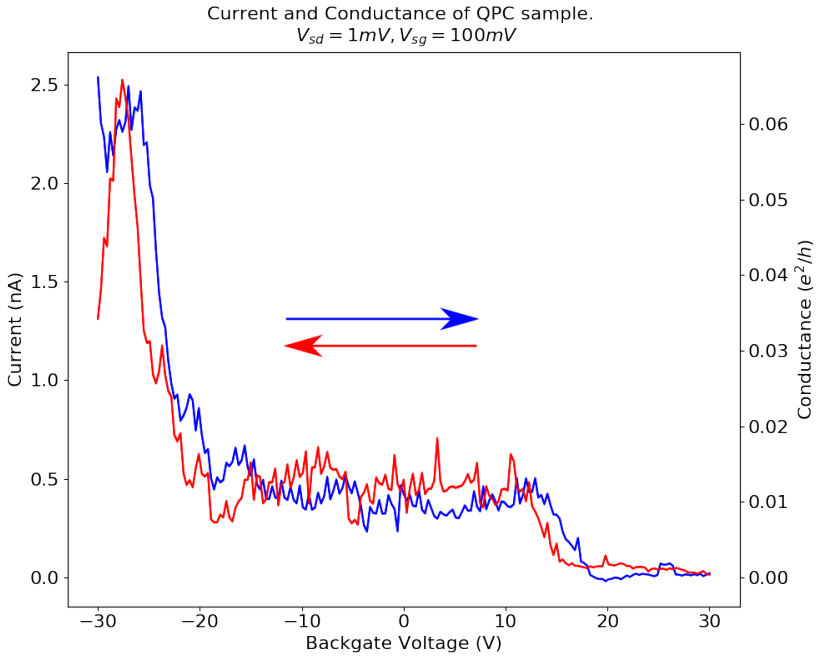

Figure 3.30: Source-Drain current vs back gate voltage sweep for the QPC sample. $V_{sd} = 1mV$, $V_{sg} = -100mV$.

neutrality point, however that was not the case. The peaks in the graph are clearly repeated with each scan and so should not be considered as noise. Possible explanations for these peaks include contamination frozen to the surface by the direct contact with liquid helium, phonon resonances, sub band resonances, ballistic oscillations or universal conduction fluctuations (57) (34).

Universal conductance fluctuations are a manifestation of coherence of the electron wavefunction through the device; they occur when the phase coherence length l_ϕ is greater than the mean free path l_m. If there was contamination frozen on to the surface of the device it would give the device a random static potential landscape, which could potentially decrease the mean free path whilst the phase relaxation length remains unaffected. As described in Section 1.4 this could lead to phase coherent transport which would support a hypothesis of universal conductance fluctuations.

The QPC sample was also measured in the liquid helium dip and an interesting

plot is shown in Figure 3.30. In this measurement the source-drain voltage was set to $1mV$, the side gate voltage was set to $-100mV$ and the back gate voltage was swept from $-30V$ to $30V$ and back to $-30V$. The coloured arrows indicate the direction of the sweeps. The left-hand axis shows the source drain current in nA units. A clear plateau is seen at $0.5nA$, with further plateaus at $1nA$ and $2.5nA$ seen at the negative extreme of the back gate voltage.

The right-hand axis of Figure 3.30 shows the conductance of the QPC with varying back gate voltage. The data from Figure 3.30 has been rescaled into units of e^2/h including a deduction of $3.5k\Omega$ for contact resistance so that it can be compared to theory. Each mode through the QPC should contribute $2e^2/h$ however it can be seen that the conductance of the sample is much smaller than expected. This could be caused by low quality contacts or is possibly an unwanted side effect of having liquid helium in direct contact with the sample.

3.10 "S" Samples

In the following sections a selection of samples which were fabricated and tested will be presented. These samples were all fabricated using the dry transfer technique as described in Section 3.4. The design of the contacts and carving is unique to each sample to fit with the size and shape of the flakes of graphene making the best use of the areas of flake available. Also an evolution of design can be seen, with changes made to the carving design to maximise the contact edge lengths.

3.10.1 S7

Figure 3.31(a) shows the overall ebeam design used in fabricating sample S7. The blue squares are the bond pads which are prepared on the chips before the sample

is fabricated. The alignment markers which are spaced in a 200μm x 200μm grid are shown in red. The areas designated for Cr/Au lift off are shown in purple; this includes both the ohmic contacts and the top gate as these can be evaporated and lifted off at the same time when the dry transfer technique is used. In the centre the carving is shown in green. The shape and design of the carved section must be carefully considered and is different compared to a sample which uses 2d contacts. Where an area of metal lift off covers an edge which is carved an ohmic contact will be made and only at these edges are the 1d contacts made. The edges between the purple lift off areas and the green carving area in the centre of Figure 3.31(b) are the ohmic contacts. The top gate does not intersect any area of carving and thus should not contact the graphene flake directly.

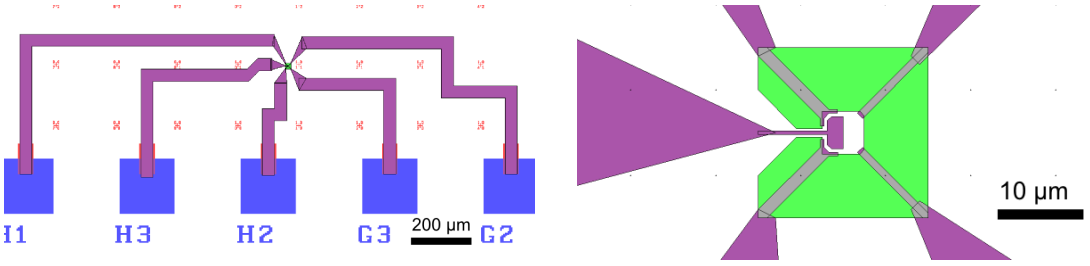

(a) (b)

Figure 3.31: (a) The full design of the ebeam pattern for sample S7 (b) The centre of the design for sample S7.

Sample S7 was designed with the intention of measuring the reflection and transmission coefficients for electrons which traverse a PN junction with the variation of the height of the junction. A PN junction is formed at the edge of the top gate by applying opposing electric fields to the back and top gates. Figure 3.32 shows an SEM image of the device with the ohmic contacts labelled from 1 to 4. Electrons are injected into the system from the contact labelled 1 and are incident on the PN junction with an angle of 45°.

Unfortunately the connects of sample S7 measured as open circuit and so the experiment could not be performed.

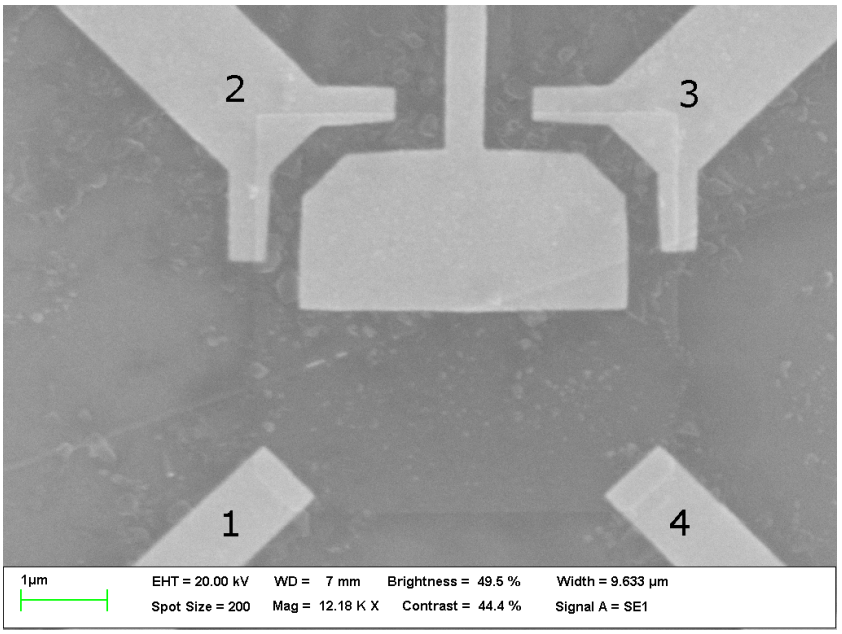

Figure 3.32: SEM image of the centre of sample S7.

3.10.2 S9

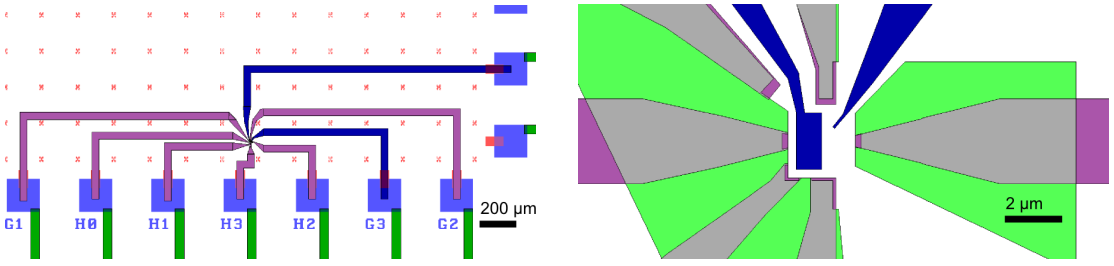

(a) (b)

Figure 3.33: (a) The full design of the ebeam pattern for sample S9 (b) The centre of the design for sample S9.

Sample S9 was designed in a way which would allow a simple measure of lensing from the PN junction. Figures 3.33(a) and (b) show the ebeam pattern used to fabricate this sample. The planned operation of the sample is as follows, with reference to the contact labels on Figure 3.34. Electrons are injected from contact 6, initially with the top gates TG1 and TG2 set to zero potential. In this operation and assuming ballistic transport the electrons can be detected as a current flowing into contacts 1, 2, 3, 4 & 5. With the main top gate, TG1, set to a potential such

that a symmetric PN junction is formed lensing should occur which will change the directions of the electrons as they pass through the PN junction. With the absence of scattering there should then be no path available for electrons to reach contacts 2 and 4 and thus the current through these contacts should be decreased. In addition the diverted electrons will now be directed to contact 3 and so the current through this contact should increase accordingly.

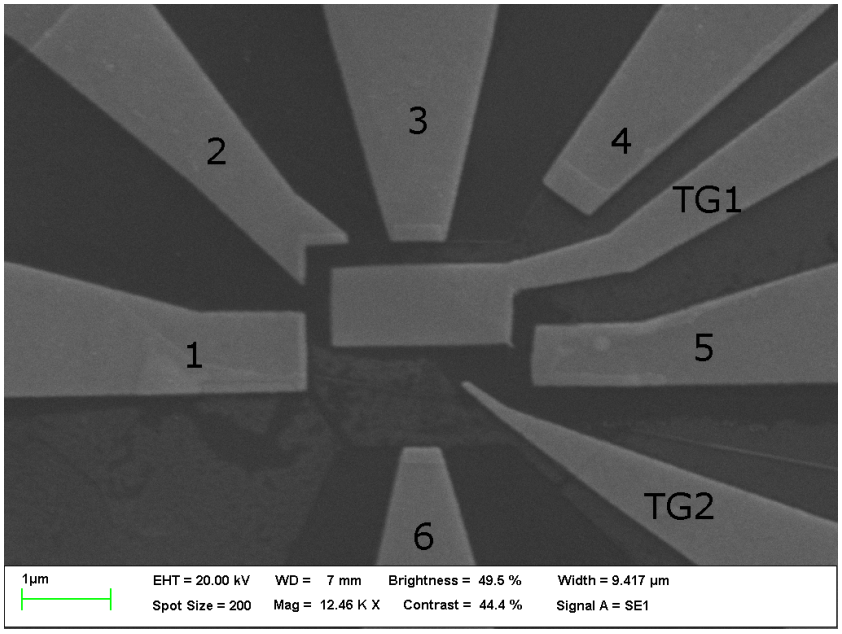

Figure 3.34: SEM image of the centre of sample S9.

Unfortunately during initial testing of the device only contact 1 and 4 were showing continuity. Contacts 2, 3, 4 & 6 each measured high resistances and were presumed not contacted ohmically. Backgate sweeps whilst applying a constant source drain voltage across contacts 1 & 4 were performed which demonstrate that these are indeed ohmic contacts onto the graphene layer. Figure 3.35 shows one of the backgate sweeps taken at room temperature using a constant source-drain voltage of 4mV.

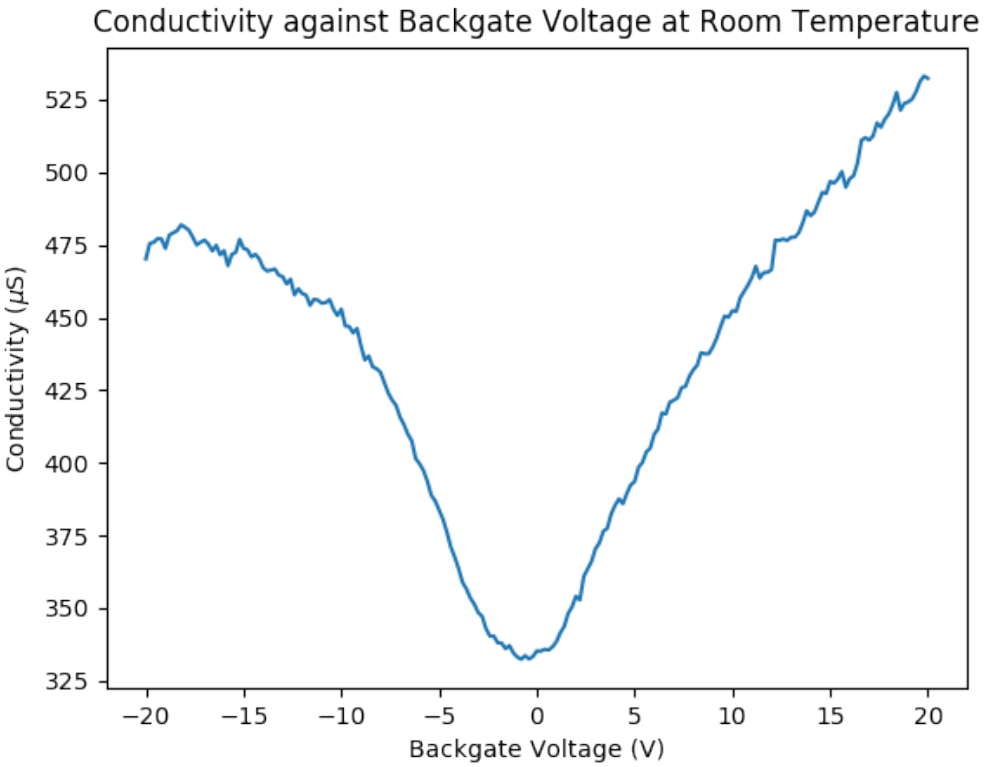

Figure 3.35: Conductivity of S9 between contacts 1 & 4 with back gate voltages. T = 298K & B = 0T.

This measurement can also be expressed as resistivity as is shown in Figure 3.36 by using Equations 1.51 and 1.52. Using Equation 1.54 and 1.53 the mobility and charge carrier density can be calculated as shown in Figure 3.37. This enables us to extract the mobility of $25,000 cm^2 V^{-1} s^{-1}$ at a charge carrier density of $1 \times 10^{11} cm^{-2}$ which gives a room temperature mean free path of $340 nm$ using Equation 1.50.

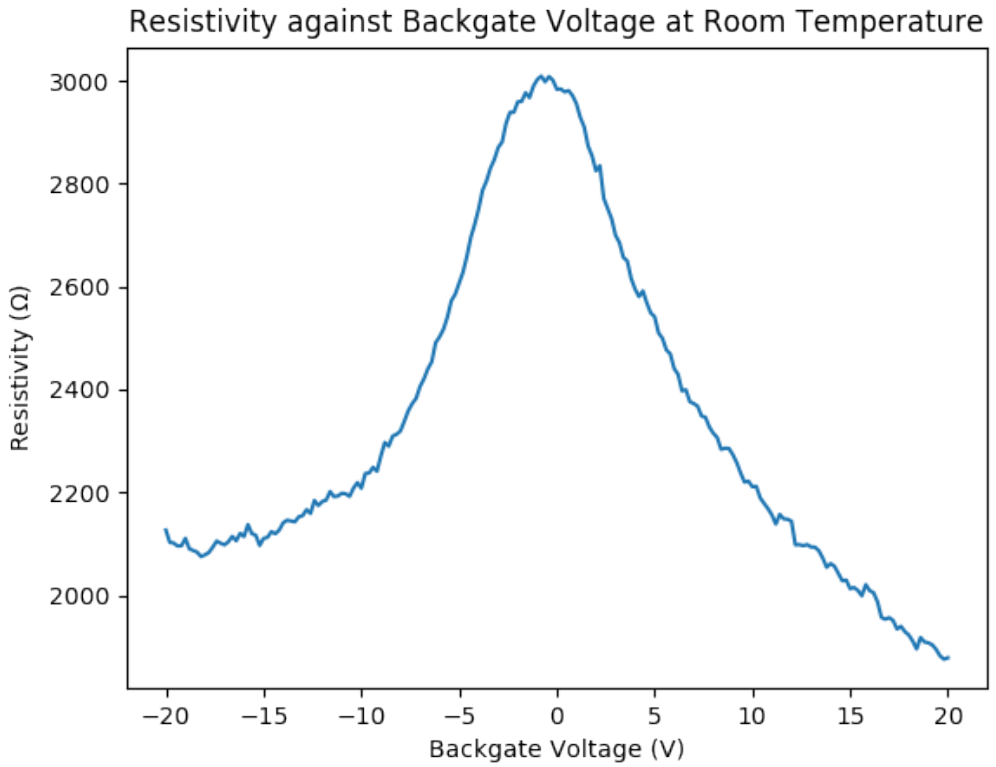

Figure 3.36: Resistivity of S9 between contacts 1 & 4 with back gate voltages. T = 298K & B = 0T.

Many sweeps were taken using these two ohmic contacts whilst varying both the back gate and top gate and also these were performed at varying magnetic fields. As this was not an intended mode for measurements with this device it is unfortunate that the paths of the electrons, and thus the readings, are rather complex.

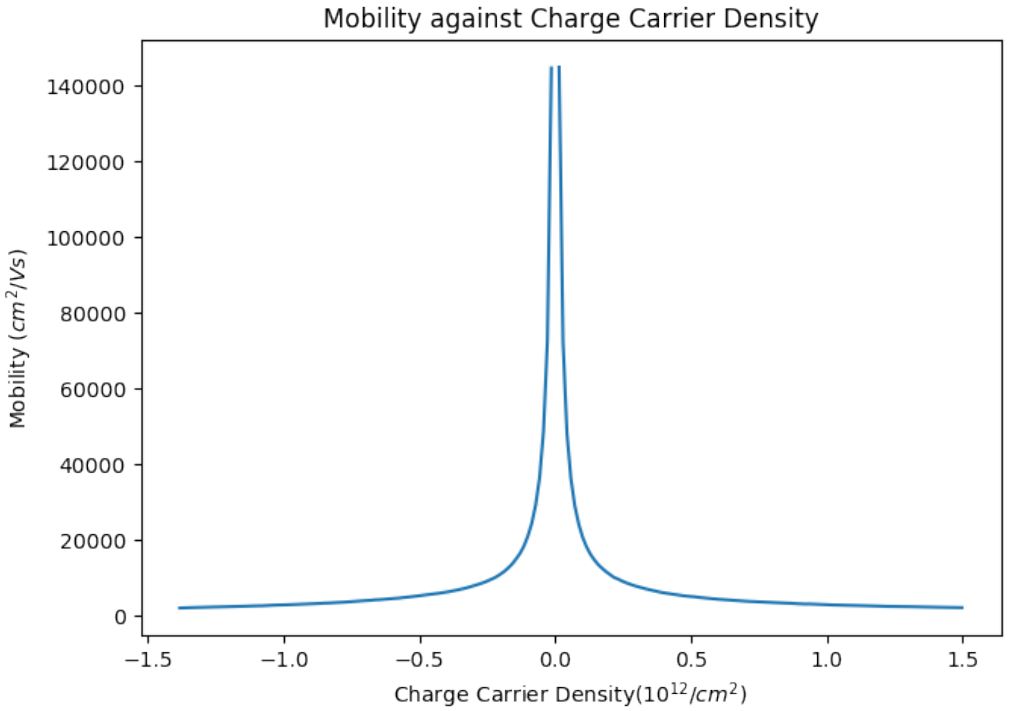

Figure 3.37: Mobility of S9 between contacts 1 & 4 with back gate voltages. T = 298K & B = 0T.

Figure 3.38 shows the conductance of Sample S9 between contacts 1 & 4 by applying a constant source voltage of 8mV on contact 4 and keeping contact 1 at ground. The top gate was swept between -5V and +5V in steps of 0.1V, the back gate was then stepped after each top gate sweep, from -20V to +20V in steps of 1V. It should be noted that the slight dip in at $V_{bg} = -4V$ is most likely a measurement error due to some fluctuations in the conditions of the sample during the measurement. This could be because of some extra potential forming locally briefly from some contamination in the sample chamber, or perhaps more likely because of some trapped charge within the measurement system which has caused interference with the measured values. However the horizontal line which can be seen at $V_{tg} = -1.1V$ is systematic across all of the scans and likely corresponds to the Dirac point of the area under the top gate. It is not varied by the back

gate over this range of V_{bg} which would agree with the theory given in Chapter 2.8 as the topgate is able to influence the energy 300 times more strongly than the back gate. The slope of the main valley is -0.24 which is the Dirac point for an area which is coupled 4 times more strongly to the top gate than to the back gate. This is most likely the small area of graphene surrounding the top gate where the charge carriers can travel from contact 4 to contact 1 going near contacts 2 and 3. In this area the electric potential is controlled by both the backgate and the topgate.

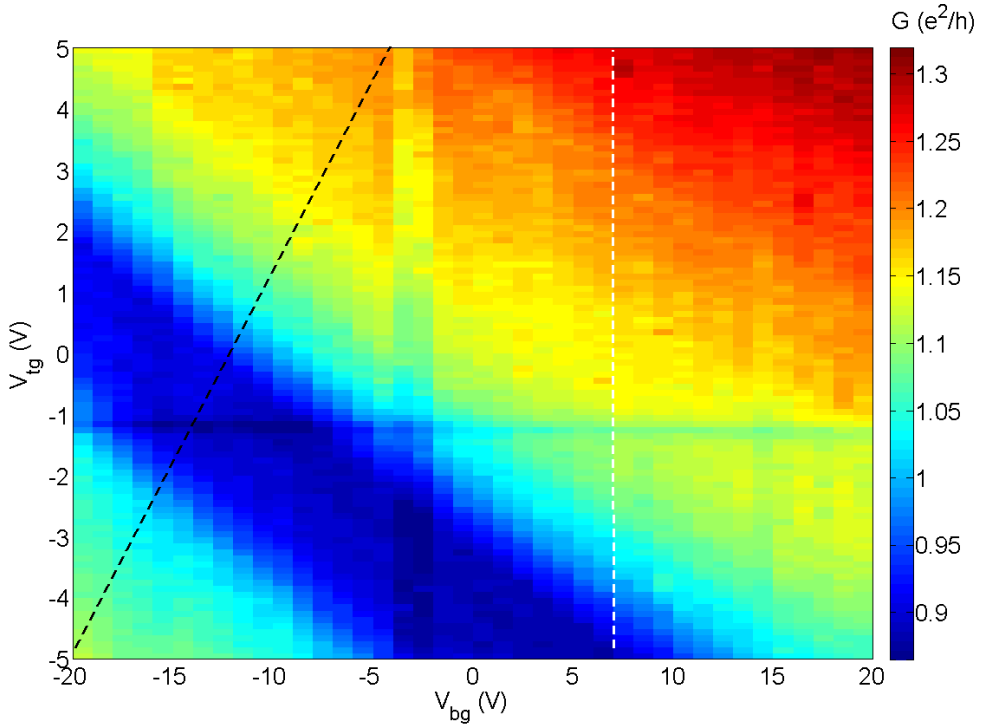

Figure 3.38: Conductance of S9 between contacts 1 & 4 with sweeping top and back gate voltages. T = 4K & B = 0T.

Figure 3.39 is a plot following the black dashed line of Figure 3.38, this shows the conductance as a function of backgate voltage for this area around the topgate.

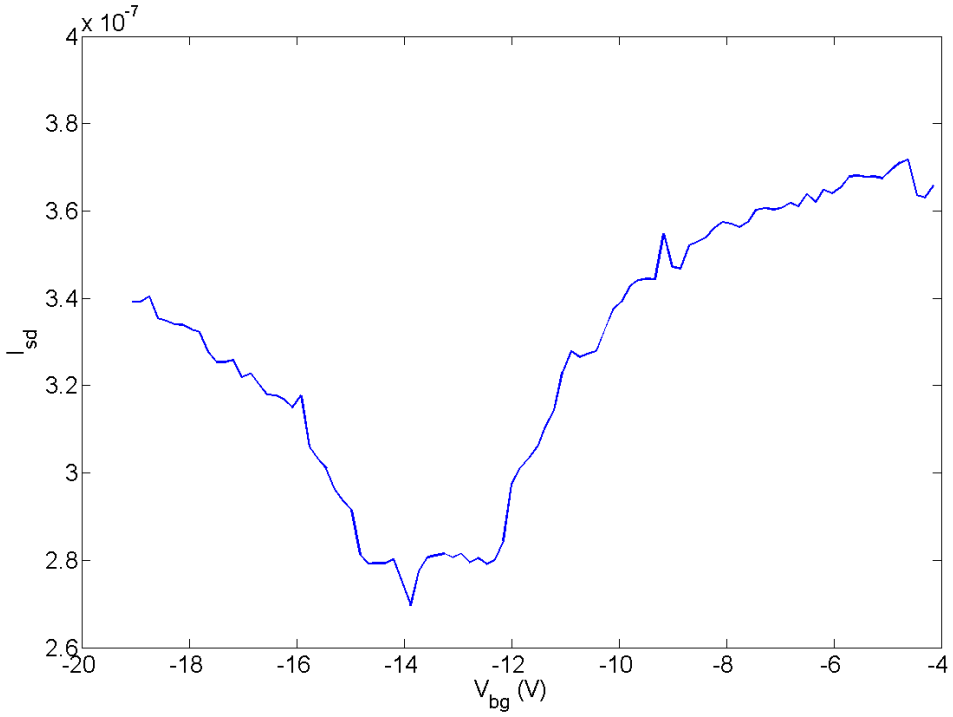

Figure 3.39: Conductance of S9 following the black dashed line of Figure 3.38.

Figure 3.40 shows a plot following the white dashed line in Figure 3.38. Notice that the dip at $V_{tg} \approx -1.2V$ is much more shallow that the dip on Figure 3.39. This tells us that a bulk of the transport is dominated by charge carriers travelling around the topgated area and not underneath it and demonstrates a clear difference with this device to many reported PNP graphene devices. Most reported devices include a PNP barrier which traverses the whole graphene sheet between the source and drain contacts and so any charge carriers which are detected must have travelled under the gated area. In this device there is clearly a path around the gate which charge carriers can use and so the influence of the topgate on the area underneath it will not be as clearly seen.

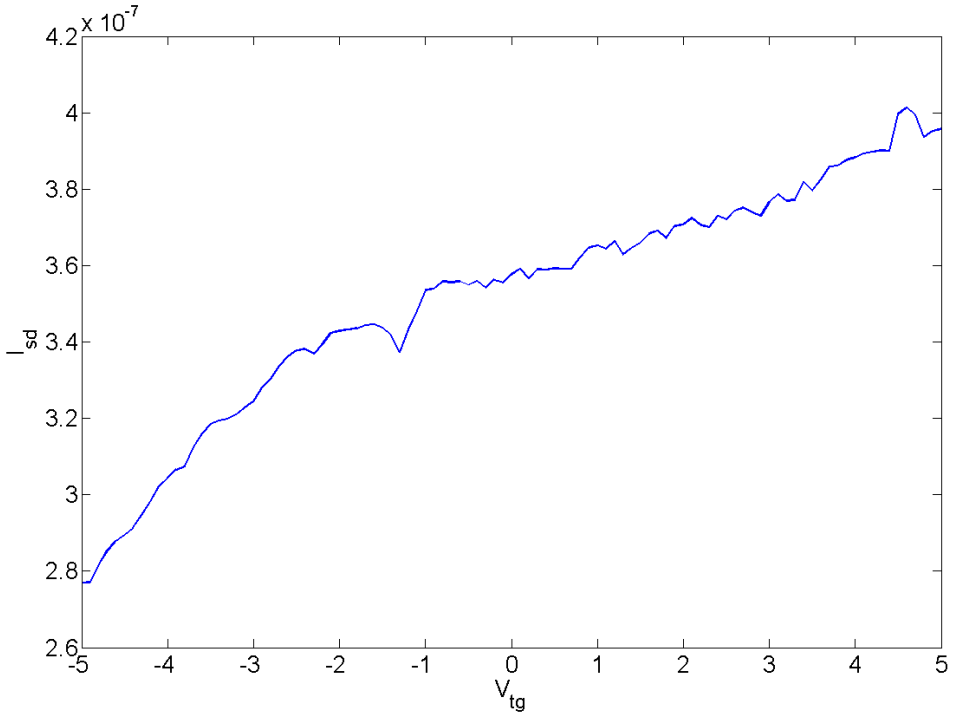

Figure 3.40: Conductance of S9 following the white dashed line of Figure 3.38.

Figure 3.41 shows a sweep with the same parameters as Figure 3.38 but with a magnetic field of 3T. Clearly the conduction is suppressed significantly compared to the case without the magnetic field. For negative values of topgate voltage the conduction is almost entirely suppressed. With the topgate fixed to a negative voltage it is only at very high positive values of the back gate at which we start to see some conductance. The slope in the upper left quadrant is -0.25 which again is the Dirac point of an area which is capacitively coupled 4 times more strongly to the top gate than the back gate. Again there is a deep valley at $V_{tg} = -1.1$ which looks constant with backgate and is therefore the Dirac point for an area of the graphene flake which is considerably better coupled to the top gate than the back gate, I.E the area of graphene under the topgate.

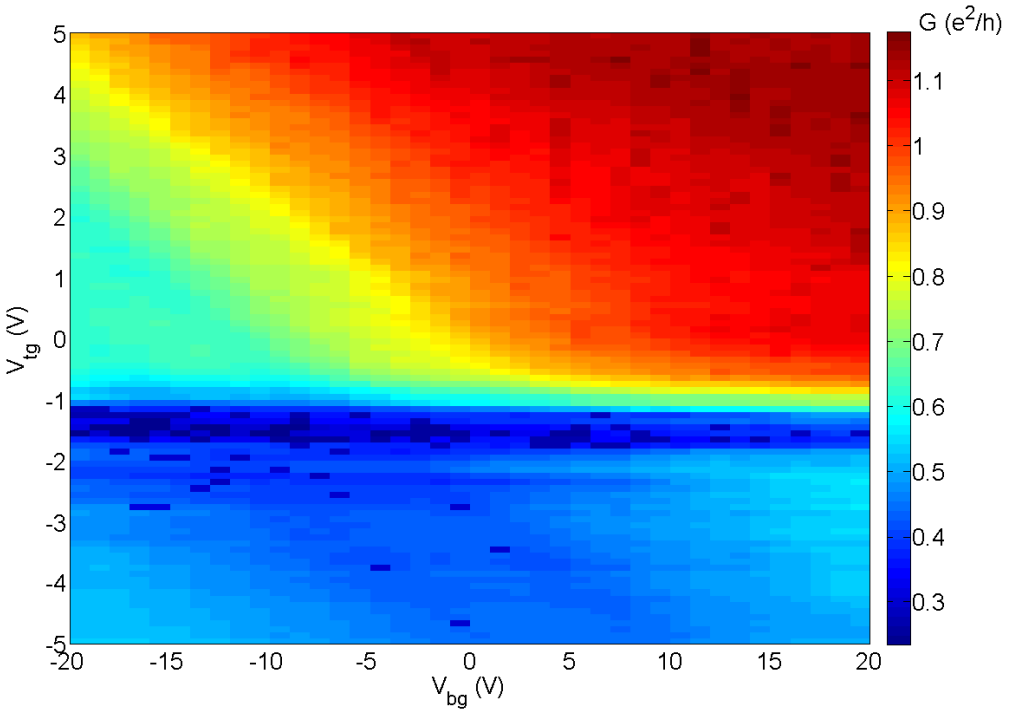

Figure 3.41: Conductance of S9 between contacts 1 & 4 with sweeping top and back gate voltages. T = 4K & B = 3T.

Figure 3.42 shows slices of the data in Figure 3.41 along constant topgate values between 5V and 0V whilst sweeping the backgate. There are three visible plateaus at $G = 0.62, 0.74$ & $0.88\, e^2/h$. These same plateaus are visible in Figure 3.43 which slices the data along lines of constant backgate voltage. We could expect to see the plateaus as quantised conductance arising from the filling of Landau levels. For bilayer graphene we would expect to see the plateaus in the conductivity as:

$$G = 4\frac{e^2}{h}|\nu| \tag{3.1}$$

Where $\nu = -3, -2, -1, 1, 2, 3$.

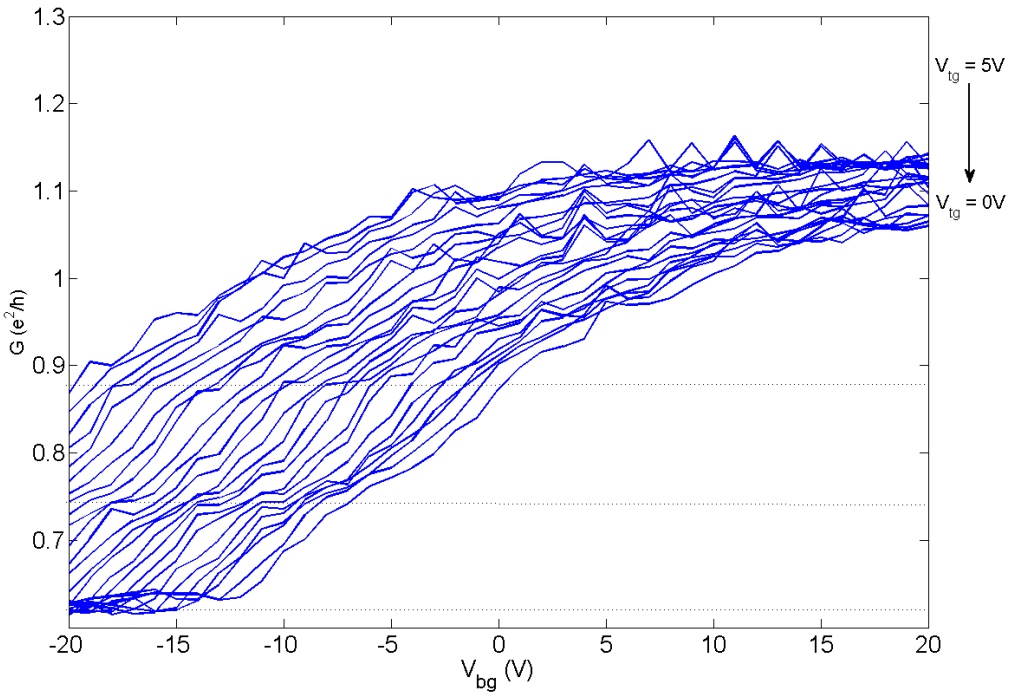

Figure 3.42: Conductance of S9 between contacts 1 & 4 with sweeping top gate voltages for topgate voltages $V_{tg} = 5$ to $0V$. T = 4K & B = 3T.

The plateaus in the data do not match up quantitatively as there are fitting parameters which should be taken into account before the conductance can be compared with the theoretical predictions. The contact resistance, R_0 affects the conductance as:

$$G = \frac{1}{R - R_0} \tag{3.2}$$

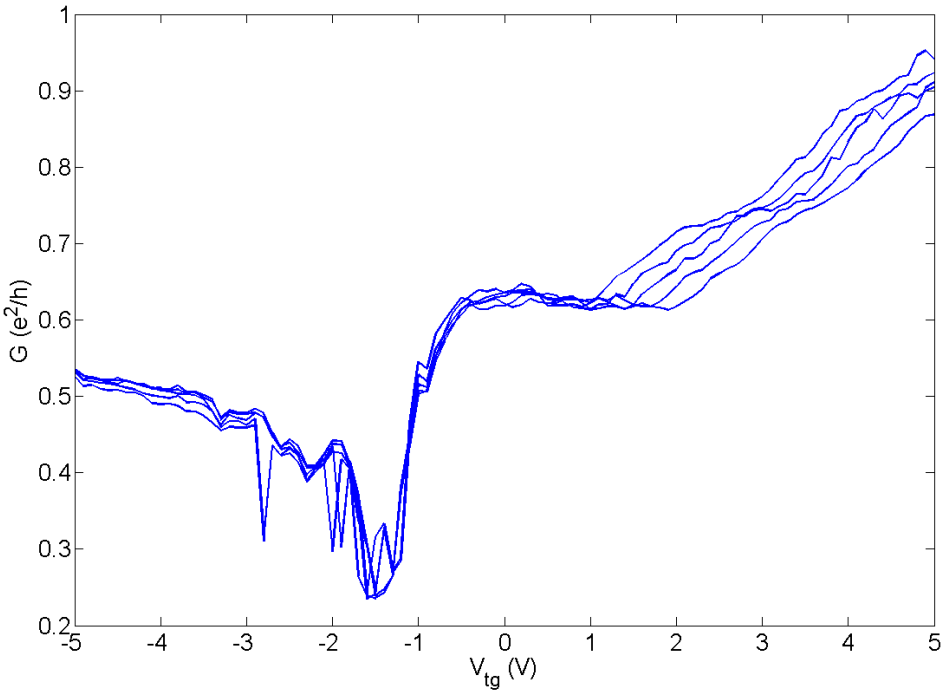

Figure 3.43: Conductance of S9 between contacts 1 & 4 with sweeping top gate voltages for backgate voltages $V_{bg} = -20$ to $-15V$. T = 4K & B = 3T.

However the usual method to remove the contact resistance is to use four connections so as measure the current with two connections and the voltage with the other two. This removes the contributions to the resistance from the connection, including the ohmic contacts on the graphene edge. As this device only had two connections that method is not possible.

Also the data should be normalised by the dimensions of the device, the width w and length l relate the conductance, G to the conductivity, σ by:

$$G = \frac{w\sigma}{l} \tag{3.3}$$

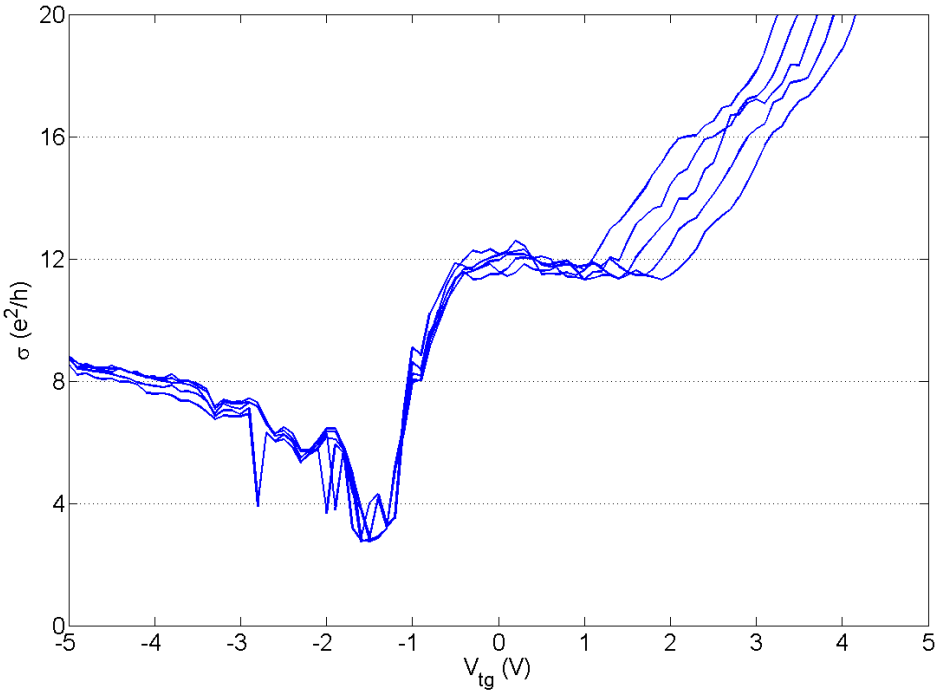

Figure 3.44: Conductance of S9 between contacts 1 & 4 with sweeping top gate voltages for backgate voltages $V_{bg} = -20$ to $-15V$. T = 4K & B = 3T.

By looking at the electron microscope image of the device in Figure 3.34 we could make an approximation of the ratio w/l as ≈ 0.5 however there are likely to be configurations of the potential landscape which will confine the conduction to the area around the top gate. In that case the w/l could easily drop to ≈ 0.05 and so it is not clear which value should be used.

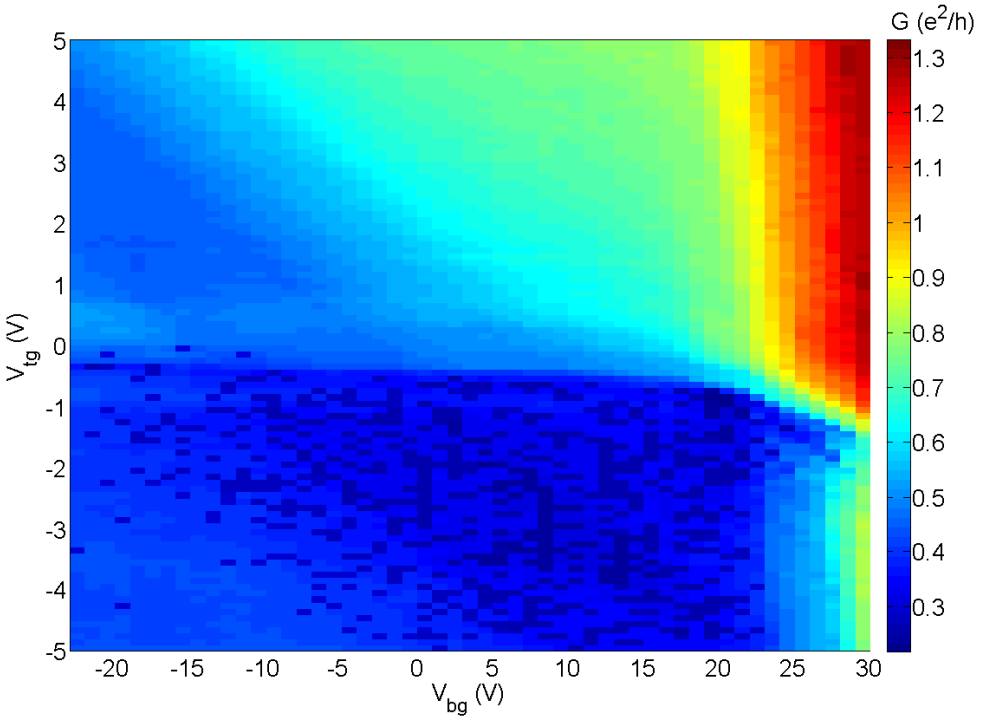

Figure 3.45: Conductance of S9 between contacts 1 & 4 with sweeping top and back gate voltages. Larger sweep values on the backgate than Figure 3.41. T = 4K & B = 3T.

Figure 3.44 shows the same data from Figure 3.43 but rescaled using the above formulas and the fitting parameters of contact resistance $R_0 = 20.4k\Omega$ and $w/l = 0.1053$. These parameters do allow for the conductance plateaus to occur at $\approx 4e^2/h$ gaps, however it would put the first conductance plateau at $\sigma = 12e^2/h$ which doesn't fit with theory.

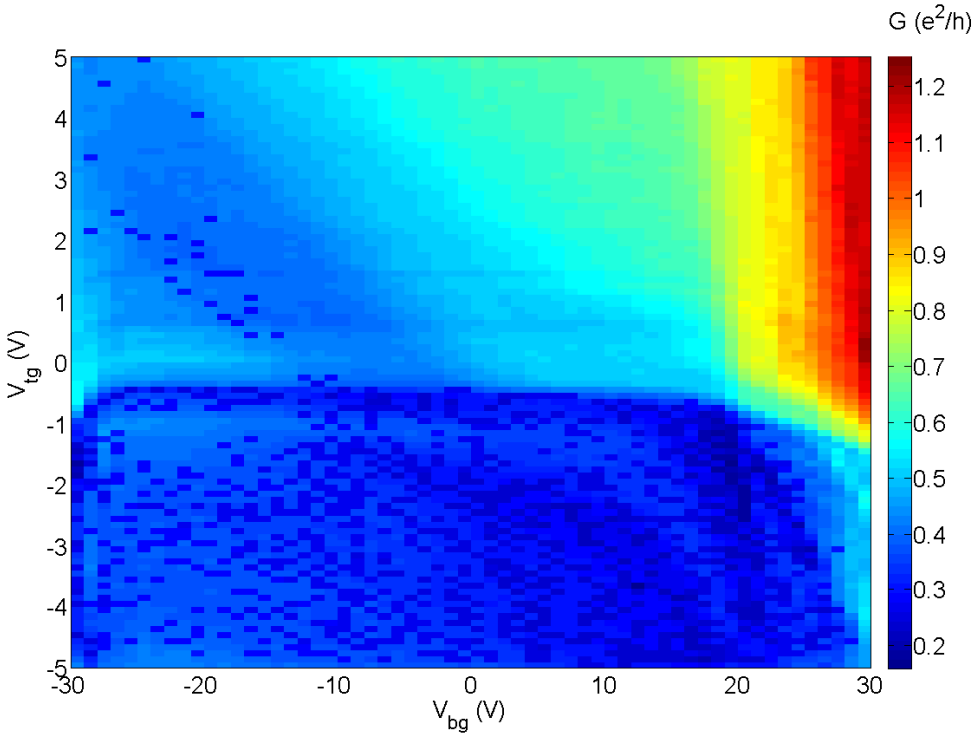

Figure 3.46: Conductance of S9 between contacts 1 & 4 with sweeping top and back gate voltages. T = 4K & B = 5T.

Figure 3.45 shows a sweep as Figure 3.41 but extending the parameters to look further into the energy map. Again the slope in the upper left quadrant is -0.25 and there is suppression of conductance for negative values of V_{tg}. At the larger values of positive V_{bg} the influence of the backgate gets much more pronounced and the edge of suppressed conduction moves towards the more negative V_{tg}.

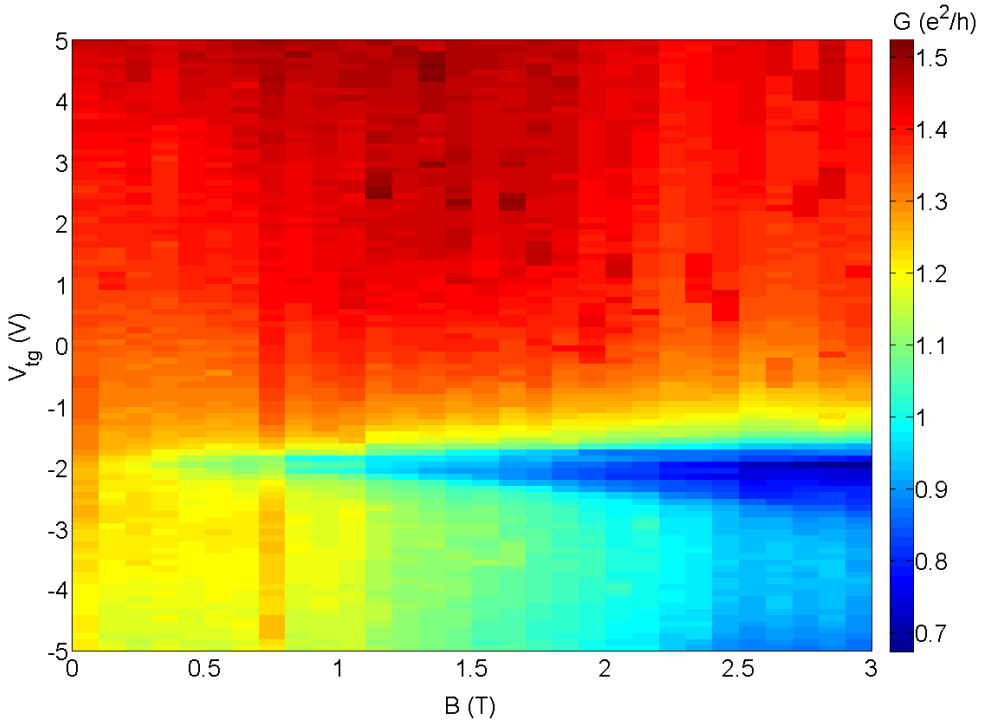

Figure 3.47: Conductance of S9 between contacts 1 & 4 with sweeping top gate voltage and magnetic field. V_{bg} = 20V. T = 4K.

For a higher field value of $5T$ Figure 3.46 shows that overall there is not much change from $3T$, but there are two small conductance suppressions which occur at constant values of V_{tg} of $0.5V$ and $1.4V$. It should be noted that the scans were performed by keeping the backgate voltage constant and sweeping the topgate and then subsequently stepping the backgate. It is expected that there be line noise in the direction of the sweeps as small changes in the device and its environment occur during the lengthy scans. However these features are in the direction of the steps meaning that it is a representation of the physics in the device. As the feature is not affected by the V_{bg}, it should be assumed that it is a feature of the area under the top gate. We can deduce from Figure 3.38 that the Dirac point for the area under the topgate is at $V_{tg} = -1.1V$, these suppression features therefore occur at a voltage $\Delta V_{tg} = 1.6V$ and $2.5V$.

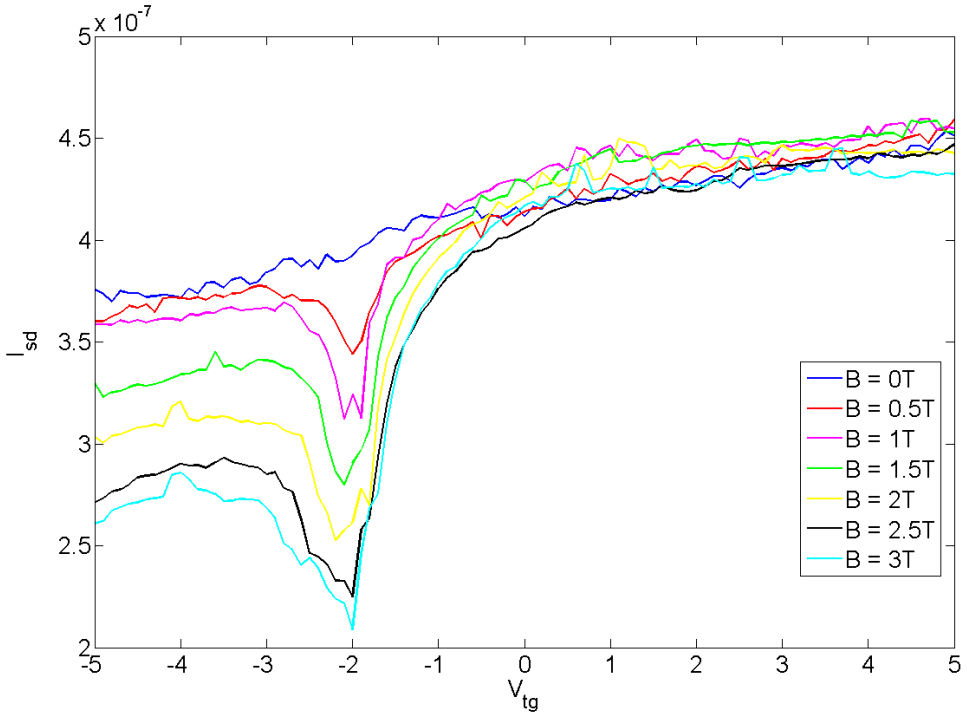

Figure 3.48: Conductance of S9 between contacts 1 & 4 with sweeping top gate voltage and magnetic field. Vertical slices through the data from Figure 3.47. V_{bg} = 20V. T = 4K.

Figure 3.47 shows the conductance of the sample between contacts 1 and 4 whilst keeping a constant backgate of 20V. The topgate was swept between -5V and 5V in steps of 0.1V and the magnetic field was swept between 0 and 3T in 0.1T steps. It shows the development of the general conduction suppression with negative top-gate voltages as the field increases. Also we can see the specific dip in conduction at $V_{tg} = -2V$. Figure 3.48 shows slices of constant magnetic field through this data and highlights the progression of the insulating region around $V_{tg} = -2V$ as the magnetic field is increased to $B = 3T$. It also shows that the conductance of the device for $V_{tg} > 0V$ is not dependant on the magnetic field, which is expected as a $PP'P$ barrier is formed which should not impede the transport of electrons across its edges.

3.10.3 S11

Figure 3.49 shows the design of sample S11 and the corresponding SEM image of the device after fabrication is shown in Figure 3.50. With reference to the labels for the contacts given in Figure 3.51 the intended function of the device was to look for reflection at the PN junction by injecting electrons into the device at contact 1 and monitoring the current at all other contacts whilst varying the top gate via contact 9. It is expected that with the topgate floating the majority of the electrons injected at contact 1 would be measured at contact 5. As the top gate is swept the PN junction is formed and electrons incident on the PN junction either reflect or transmit depending on their incidence angle for a given junction height.

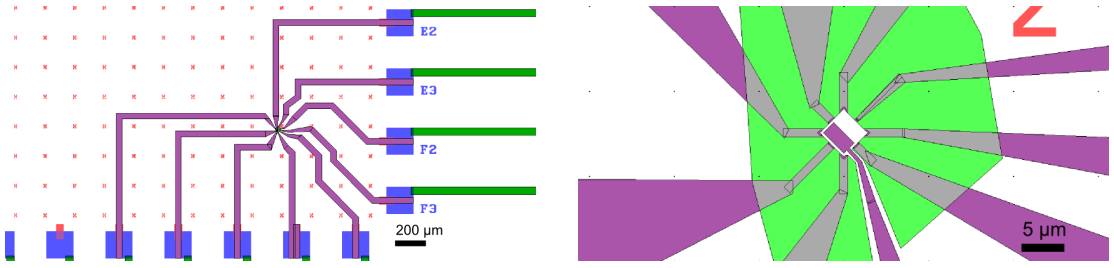

(a) (b)

Figure 3.49: (a) The full design of the ebeam pattern for sample S11 (b) The centre of the design for sample S11.

The angle of peak reflectance would vary with the PN junction height and it should be possible to tune the reflectance so that roughly 50% of incident electrons are transmitted to contact 5 and 50% of them are reflected to contact 3. The symmetry allows some redundancy in contacts in case one or two do not work.

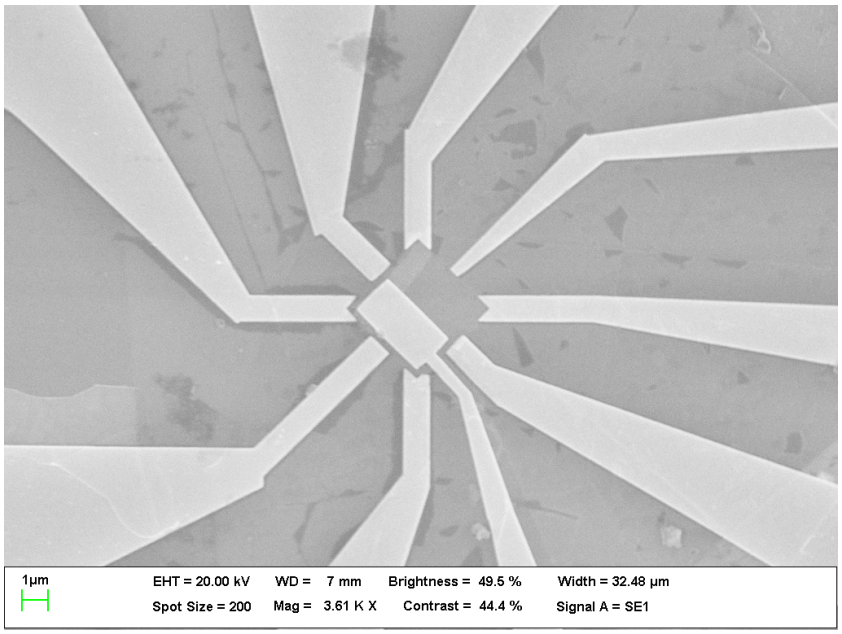

Figure 3.50: SEM image of the centre of sample S11.

Unfortunately the contacts on this device were not conductive. When measured in the cryostat the resistance between any pair of contacts was $> 50M\Omega$. Of course all contacts were then rechecked on the microscope and the measurement system was checked with known working samples to rule out any other causes for non-continuity. It is thought that the an extra step in the preparation of the edges before the metal contacts are formed is required. The graphene edge there is not forming a good contact with the Chrome/Gold which is most likely down to the chemical termination of the edge. This is controlled by the conditions present when the device is carved in the ICP plasma. Wang et al found that the contact certainly changed by O_2 plasma treatment after carving (33), however further investigation is required to find the best recipe to improve the electrical contacts.

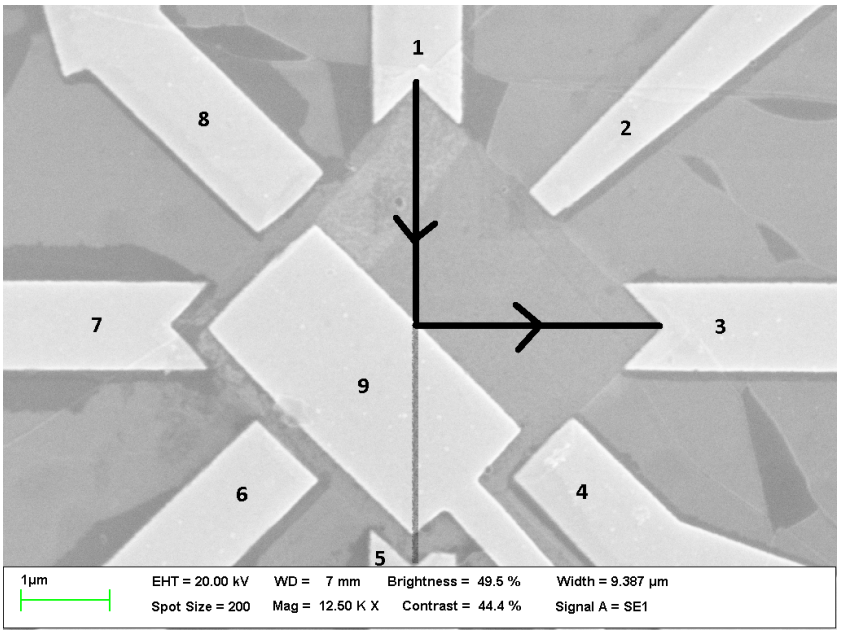

Figure 3.51: Higher magnification SEM image of the centre of sample S11.

Chapter 4

Conclusions

It has been shown how the pursuit of quantum optics of electrons in graphene could be a window into quantum computing, and along the way many interesting phenomena can be explored as the unique configuration of condensed matter allows analogues to other areas of physics which are otherwise difficult to attain in the lab such as:

- Relativistic physics via Klein tunnelling.
- Metamaterials via negative refraction.
- Quantum optics via electron interference.

Through the combination of these phenomena a device was planned which could explore the strange world of quantum mechanics and bring to light a means to produce a physical representation of the theorised effects.

The issues surrounding placing graphene flakes on hBN flakes were investigated, with bubbles between the graphene-hBN interface found to hinder device fabrication. A method of annealing was found to reduce the bubble size to allow

devices to be fabricated in the remaining flat graphene areas. A newer method was adopted for later devices by using the dry transfer technique to encapsulate the graphene flakes with hBN without the dissolving of polymer layers next to the graphene. By avoiding the resulting polymer contamination from dissolving the cleaner surfaces of the graphene and hBN layers allow for a better continuous adhesion without bubbles appearing. Contacts to the graphene flake were subsequently one dimensional as the graphene was contacted with metal on the edge of the 2D sheet.

Graphene devices were produced using the most current techniques of fabrication to optimise their electrical performance. Etching of the hBN-graphene-hBN sandwich allowed one dimensional contacts to be made along the edge of the graphene along with carefully placed topgates to control the potential landscape of the devices in order to create PNP barriers for the dual purpose of lensing and path splitting. Although every care was taken in the fabrication of the devices, consistently making ohmic contacts is still proving very difficult. Perhaps oxygen plasma treatment or some other process is required to improve the electrical contact between the graphene edge and the chrome gold contacts. In spite of this issue electrical measurements on the device with the usable contacts show evidence of the quantisation of conductance via Landau levels and the device shows clear PNP style conductance. The devices mobility was measured to be $25,000 cm^2 V^{-1} s^{-1}$ at room temperature which gives a mean free path of 340 nm. The liquid helium cryostat was then used to cool devices down to a temperature of $4.2K$ and the included superconducting magnet was used to apply fields up to $8T$. Labview code was written to arrange the control of data recording from the various pieces of equipment required for the electrical readings of the devices. With a $0T$ field and sweeping of both top and bottom gates two lines of minima appear in the conductance, one for a region which is dominated by the influence of the topgate at $V_{tg} = -1.1V$ and another which is influenced by both top and bottom gates.

These correspond to the region under the top gate and the region around it. A suppression of the conductance was found with increasing magnetic field for values of topgate $\approx -2V$. Under the influence of a magnetic field three plateaus in the conductance are found at $G = 0.62,\ 0.74\ \&\ 0.88\ e^2/h$. It was found that with increasing magnetic field strength a suppression of conduction occurs for values of top gate $V_{tg} = -2V$, whilst the area of parameter space which represents a $PP'P$ barrier forming shows no dependance on the magnetic field strength.

Through the process of fabricating graphene devices it was found that graphene is easily susceptible to ESD, it is advised that future experimentalists keep this in mind when planning their chip fabrication. An example of a design for a chip which protects the device from ESD is shown in Figure 3.20 and it was found to be successful in its implementation.

A side gated nanoribbon in graphene was produced by using a He ion microscope to selectively remove the carbon atoms in the graphene flake. The nanoribbon had a width of 8 nm. This nanoribbon showed a quantised conduction as a function of the backgate voltage, although not with the clear step function as is possible for QPC devices made from GaAs. This shows that a QPC cannot be made in single layer graphene devices by using side gates to control the constriction width as in previous 2DEG devices. This is due to the semimetal classification of graphene as no insulating regions can be induced by the gates, only a change of bands is possible.

Universal conduction fluctuations were seen in a device which was placed in direct contact with liquid He. This is thought to have occurred due to a static scattering sites causing the mean free path to be smaller than the phase coherence length which causes the localisation effects of universal conduction fluctuations.

A scheme has been presented which would enable both the splitting of the path of ballistic electrons and recombination of those paths to form a closed loop about

which a phase difference could be introduced. Methods for introducing that phase difference include global magnetic field or local gates which could allow individual control of many such structures should an array of them be connected together to perform computation.

This thesis represents four years of work split between long hours on the microscope, exfoliating graphene flakes, reading papers, understanding the past and current work in the field, fabricating the samples in the cleanroom, researching new fabrication techniques, finding and avoiding the many pitfalls in cleanroom techniques, many weeks spent on cooling the cryostat, late nights taking measurements, evenings and weekends analysing the data and much time preparing this document. I hope that future graphene experimentalists are able to use the information presented here to get a head start on doing some interesting and fulfilling experiments in quantum optics with graphene.

Chapter 5

Future Work

It is hoped that the work presented in this thesis can be used to guide further work in quantum optics of electrons in graphene. In order to make progress in this field there are many further experiments which can be performed, by building a toolbox of analogous quantum optics devices some very powerful and interesting experiments can be performed.

5.1 Veselago Lensing Using a PN Step

This is essentially the device which I have been making. Using a potential step to create a PN junction and with an equidistant source and drain from the step edge a strong lensing effect should be present when compared with the absence of the step. This should be evident from an increase in current in the equidistant mirror image drain when the lens is switched on as compared with it switched off.

5.2 Split Path Interferometer & Measure $g^{(1)}$

With a PNP barrier the transmission of the device is dependent on the angle of incidence of the electron with the barrier edge. Fabry Pérot oscillations are expected to determine the allowed angles of transmission. For mono-layer Klein tunnelling allows the electrons with $\theta = 0$ to pass through unimpeded. However for Bi-layer graphene the transmission is expected to follow a $sin^2(\theta)$ relation as given by equation 2.16 leading to two paths available. By placing small finger topgates above the expected separate paths after the main PNP barrier it should be possible to introduce an additional phase due to the difference in fermi wavelength through the $PP'P$ barrier. This uses a single source and a single detector and uses the bulk transport of charge carriers.

5.3 Measure $g^{(2)}$

Taking things a step further a Hong Ou Mandel experiment with electrons could be envisaged with this device if there was precision control and detection of single charge carriers. Using a charge pump as shown by Connolly et al (58) or a QPC with pulsed barriers to produce stream of charge carriers and also a single charge detector; Neumann et al (41) have shown work towards this. By sending a stream of single electrons through the interferometer and measuring their coincidence rates through the two arms one could look for anti bunching of the electrons. This work is beyond the scope of this PhD as the fabrication and measurement of a single electron source is very challenging and the single electron detector is yet to be fully realised as a working device in the community of graphene research although Neumann et al (41) have made excellent steps towards it.

5.4 Electrons or holes?

Following the work of Allain et al (14) which describes the interactions of electrons which are incident on PN junctions in graphene, there appears to be a question which can be answered by experimentation. (14) describe and give arguments for the reader to interpret the electron as remaining as an electron as it passed from conduction band to the valence band in a PN junction. This is in contrast to Milovanovic et al (59) who describes the electron as changing to a hole as it passes through the PN junction and switches bands. The switching from electrons to holes is an essential effect in order to observe snake states along PN junctions. Snake states are predicted to be observed along PN junctions when a magnetic field is applied as the hole and electron have opposite charge polarities which would therefore lead to a switch in direction of the Lorentz force that the charge carrier experiences after passing through the PN junction. An electron which is travelling along a circular trajectory and which becomes incident on the PN junction switches to being a hole on the other side and then follows a reversed circular direction back towards the PN junction further along the junction to repeat the process as it crosses and reverts to an electron. If on the other hand the electron remains as an electron and retains its negative charge then the electron will experience the Lorentz force in the same way either side of the PN junction, this would prohibit snake states and only the effects of cyclotron movement and scattering at the PN junctions would be observed. Therefore a robust method to measure and observe snake states in PN junctions would prove the behaviour of the electron which has passed through a PN junction.

References

[1] I. Neder, N. Ofek, Y. Chung, M. Heiblum, D. Mahalu, and V. Umansky, "Interference between two indistinguishable electrons from independent sources.," *Nature*, vol. 448, pp. 333–7, jul 2007.

[2] R. Hanbury Brown and R. Q. Twiss, "A Test of a New Type of Stellar Interferometer on Sirius," *Nature*, vol. 178, pp. 1046–1048, nov 1956.

[3] M. Henny, "The Fermionic Hanbury Brown and Twiss Experiment," *Science*, vol. 284, pp. 296–298, apr 1999.

[4] W. D. Oliver, "Hanbury Brown and Twiss-Type Experiment with Electrons," *Science*, vol. 284, pp. 299–301, apr 1999.

[5] R. Loudon, "Fermion and boson beam-splitter statistics," *Physical Review A*, vol. 58, pp. 4904–4909, dec 1998.

[6] M. A. Nielsen and I. Chuang, "Quantum computation and quantum information," 2002.

[7] S. L. Braunstein and P. Van Loock, "Quantum information with continuous variables," *Reviews of Modern Physics*, vol. 77, no. 2, p. 513, 2005.

[8] W. Xiang-Bin, "Theorem for the beam-splitter entangler," *Physical Review A*, vol. 66, no. 2, p. 24303, 2002.

[9] E. Knill, R. Laflamme, and G. J. Milburn, "A scheme for efficient quantum computation with linear optics," *Nature*, vol. 409, no. 6816, pp. 46–52, 2001.

[10] A. H. Castro Neto, F. Guinea, N. M. R. Peres, K. S. Novoselov, and A. K. Geim, "The electronic properties of graphene," *Reviews of Modern Physics*, vol. 81, pp. 109–162, jan 2009.

[11] Phys.Org, "Topological matter in optical lattices," 2011.

[12] C. Jacoboni, *Theory of Electron Transport in Semiconductors: A Pathway from Elementary Physics to Nonequilibrium Green Functions*. Springer Series in Solid-State Sciences, Springer Berlin Heidelberg, 2010.

[13] A. K. Geim and K. S. Novoselov, "The rise of graphene," *Nature Materials*, vol. 6, pp. 183–191, 2007.

[14] P. E. Allain and J. N. Fuchs, "Klein tunneling in graphene: optics with massless electrons," *The European Physical Journal B*, vol. 83, pp. 301–317, oct 2011.

[15] C. Kittel, *Introduction to Solid State Physics*. Wiley, 1996.

[16] C. Schonenberger, "Bandstructure of Graphene and Carbon Nanotubes : An Exercise in Condensed Matter Physics," Tech. Rep. 2, 2000.

[17] R. Saito, G. Dresselhaus, and M. S. Dresselhaus, *Physical Properties of Carbon Nanotubes*. 1998.

[18] S. Reich, C. Thomsen, and J. Maultzsch, *Carbon Nanotubes: Basic Concepts and Physical Properties*. Wiley, 2008.

[19] H.-A. Bachor and T. C. Ralph, eds., *A Guide to Experiments in Quantum Optics*. Weinheim, Germany: Wiley-VCH Verlag GmbH, jan 2004.

[20] R. C. Liu and B. Odom, "Quantum interference in electron collision," vol. 391, no. January, pp. 263–265, 1998.

[21] C. K. Hong, Z. Y. Ou, and L. Mandel, "Measurement of subpicosecond time intervals between two photons by interference," *Physical Review Letters*, vol. 59, pp. 2044–2046, nov 1987.

[22] T. Jonckheere, J. Rech, C. Wahl, and T. Martin, "Electron and hole Hong-Ou-Mandel interferometry," 2012.

[23] C. Lee, X. Wei, J. W. Kysar, and J. Hone, "Measurement of the Elastic Properties and Intrinsic Strength of Monolayer Graphene," *Science*, vol. 321, pp. 385–388, jul 2008.

[24] A. a. Balandin, S. Ghosh, W. Bao, I. Calizo, D. Teweldebrhan, F. Miao, and C. N. Lau, "Superior Thermal Conductivity of Single-Layer Graphene," *Nano Letters*, vol. 8, pp. 902–907, mar 2008.

[25] J. S. Bunch, S. S. Verbridge, J. S. Alden, A. M. van der Zande, J. M. Parpia, H. G. Craighead, and P. L. McEuen, "Impermeable atomic membranes from graphene sheets.," *Nano letters*, vol. 8, pp. 2458–2462, aug 2008.

[26] K. S. Novoselov, a. K. Geim, S. V. Morozov, D. Jiang, Y. Zhang, S. V. Dubonos, I. V. Grigorieva, and a. a. Firsov, "Electric field effect in atomically thin carbon films.," *Science (New York, N.Y.)*, vol. 306, pp. 666–669, oct 2004.

[27] Y. Zhang, Y.-w. Tan, H. L. Stormer, and P. Kim, "Experimental observation of the quantum Hall effect and Berry's phase in graphene.," *Nature*, vol. 438, pp. 201–204, nov 2005.

[28] K. I. Bolotin, F. Ghahari, M. D. Shulman, H. L. Stormer, and P. Kim, "Observation of the fractional quantum Hall effect in graphene.," *Nature*, vol. 462, pp. 196–199, nov 2009.

[29] J. R. Williams, L. DiCarlo, and C. M. Marcus, "Quantum Hall effect in a gate-controlled p-n junction of graphene.," *Science (New York, N.Y.)*, vol. 317, pp. 638–641, aug 2007.

[30] T. Taychatanapat and P. Jarillo-Herrero, "Electronic Transport in Dual-Gated Bilayer Graphene at Large Displacement Fields," *Physical Review Letters*, vol. 105, pp. 1–4, oct 2010.

[31] C. R. Dean, A. F. Young, I. Meric, C. Lee, L. Wang, S. Sorgenfrei, K. Watanabe, T. Taniguchi, P. Kim, K. L. Shepard, and J. Hone, "Boron nitride substrates for high-quality graphene electronics.," *Nature nanotechnology*, vol. 5, pp. 722–6, oct 2010.

[32] A. S. Mayorov, R. V. Gorbachev, S. V. Morozov, L. Britnell, R. Jalil, L. A. Ponomarenko, P. Blake, K. S. Novoselov, K. Watanabe, T. Taniguchi, and A. K. Geim, "Micrometer-scale ballistic transport in encapsulated graphene at room temperature.," *Nano letters*, vol. 11, pp. 2396–9, jun 2011.

[33] L. Wang, I. Meric, P. Y. Huang, Q. Gao, Y. Gao, H. Tran, T. Taniguchi, K. Watanabe, L. M. Campos, D. a. Muller, J. Guo, P. Kim, J. Hone, K. L. Shepard, and C. R. Dean, "One-dimensional electrical contact to a two-dimensional material.," *Science (New York, N.Y.)*, vol. 342, pp. 614–7, nov 2013.

[34] S. Datta, *Electronic Transport in Mesoscopic Systems*, vol. 3 of *Cambridge studies in semiconductor physics and microelectronic engineering*. Cambridge University Press, 1995.

[35] K. I. Bolotin, K. J. Sikes, Z. Jiang, M. Klima, G. Fudenberg, J. Hone, P. Kim, and H. L. Stormer, "Ultrahigh electron mobility in suspended graphene," *Solid State Communications*, vol. 146, pp. 351–355, jun 2008.

[36] V. V. Cheianov, V. Fal'ko, and B. L. Altshuler, "The focusing of electron flow and a Veselago lens in graphene p-n junctions.," *Science (New York, N.Y.)*, vol. 315, pp. 1252–5, mar 2007.

[37] V. G. Veselago, "The electrodynamics of substances with simultaneously negative values of ϵ and μ.," *Soviet Physics Uspekhi*, vol. 10, pp. 509–514, apr 1968.

[38] E. Stolyarova, D. Stolyarov, K. Bolotin, S. Ryu, L. Liu, K. T. Rim, M. Klima, M. Hybertsen, I. Pogorelsky, I. Pavlishin, K. Kusche, J. Hone, P. Kim, H. L. Stormer, V. Yakimenko, and G. Flynn, "Observation of graphene bubbles and effective mass transport under graphene films.," *Nano letters*, vol. 9, pp. 332–7, jan 2009.

[39] V. Cheianov, V. Fal'ko, and V. Fal'ko, "Selective transmission of Dirac electrons and ballistic magnetoresistance of n-p junctions in graphene," *Physical Review B*, vol. 74, p. 041403, jul 2006.

[40] O. Klein, "Die Reflexion von Elektronen an einem Potentialsprung nach der relativistischen Dynamik von Dirac," *Zeitschrift fr Physik*, vol. 53, pp. 157–165, mar 1929.

[41] C. Neumann, C. Volk, S. Engels, and C. Stampfer, "Graphene-based charge sensors.," *Nanotechnology*, vol. 24, p. 444001, nov 2013.

[42] B. van Wees, H. van Houten, C. Beenakker, J. Williamson, L. Kouwenhoven, D. van der Marel, and C. Foxon, "Quantized conductance of point contacts in a two-dimensional electron gas," *Physical Review Letters*, vol. 60, pp. 848–850, feb 1988.

[43] V. V. Mitin, V. A. Kochelap, and M. A. Stroscio, *Introduction to Nanoelectronics: Science, Nanotechnology, Engineering, and Applications*. Cambridge University Press, 2008.

[44] M. I. Katsnelson, K. S. Novoselov, and A. K. Geim, "Chiral tunnelling and the Klein paradox in graphene," *Nature Physics*, vol. 2, pp. 620–625, aug 2006.

[45] N. Stander, B. Huard, and D. Goldhaber-Gordon, "Evidence for Klein Tunneling in Graphene p-n Junctions," *Physical Review Letters*, vol. 102, p. 026807, jan 2009.

[46] R. V. Gorbachev, A. S. Mayorov, A. K. Savchenko, D. W. Horsell, and F. Guinea, "Conductance of p-n-p graphene structures with "air-bridge" top gates.," *Nano letters*, vol. 8, pp. 1995–9, jul 2008.

[47] B. Van Duppen and F. M. Peeters, "Klein paradox for a pn junction in multilayer graphene," *EPL (Europhysics Letters)*, vol. 102, p. 27001, apr 2013.

[48] T. Tudorovskiy, K. J. a. Reijnders, and M. I. Katsnelson, "Chiral tunneling in single-layer and bilayer graphene," *Physica Scripta*, vol. T146, p. 014010, jan 2012.

[49] P. J. Zomer, S. P. Dash, N. Tombros, and B. J. van Wees, "A transfer technique for high mobility graphene devices on commercially available hexagonal boron nitride," *Applied Physics Letters*, vol. 99, no. 23, p. 232104, 2011.

[50] A. Venugopal, L. Colombo, and E. M. Vogel, "Contact resistance in few and multilayer graphene devices," *Applied Physics Letters*, vol. 96, no. 1, p. 013512, 2010.

[51] C.-R. Wang, W.-S. Lu, L. Hao, W.-L. Lee, T.-K. Lee, F. Lin, I.-C. Cheng, and J.-Z. Chen, "Enhanced Thermoelectric Power in Dual-Gated Bilayer Graphene," *Physical Review Letters*, vol. 107, p. 186602, oct 2011.

[52] R. R. Nair, P. Blake, A. N. Grigorenko, K. S. Novoselov, T. J. Booth, T. Stauber, N. M. R. Peres, and A. K. Geim, "Fine structure constant defines visual transparency of graphene.," *Science (New York, N.Y.)*, vol. 320, p. 1308, jun 2008.

[53] T. Taychatanapat, K. Watanabe, T. Taniguchi, and P. Jarillo-Herrero, "Quantum Hall effect and Landau-level crossing of Dirac fermions in trilayer graphene," *Nature Physics*, vol. 7, pp. 621–625, jun 2011.

[54] M. C. Lemme, D. C. Bell, J. R. Williams, L. A. Stern, B. W. H. Baugher, P. Jarillo-Herrero, and C. M. Marcus, "Etching of graphene devices with a helium ion beam.," *ACS nano*, vol. 3, pp. 2674–6, sep 2009.

[55] S. A. Boden, Z. Moktadir, D. M. Bagnall, H. Mizuta, and H. N. Rutt, "Focused helium ion beam milling and deposition," *Microelectronic Engineering*, vol. 88, pp. 2452–2455, aug 2011.

[56] Z. Cheng, Q. Zhou, C. Wang, Q. Li, C. Wang, and Y. Fang, "Toward Intrinsic Graphene Surfaces: A Systematic Study on Thermal Annealing and Wet-Chemical Treatment of SiO2-Supported Graphene Devices," *Nano letters*, vol. 11, pp. 767–771, 2011.

[57] A. F. Young and P. Kim, "Quantum interference and Klein tunnelling in graphene heterojunctions," *Nature Physics*, vol. 5, pp. 222–226, feb 2009.

[58] M. R. Connolly, K. L. Chiu, S. P. Giblin, M. Kataoka, J. D. Fletcher, C. Chua, J. P. Griffiths, G. a. C. Jones, V. I. Fal'ko, C. G. Smith, and T. J. B. M. Janssen, "Gigahertz quantized charge pumping in graphene quantum dots," *Nature Nanotechnology*, vol. 8, pp. 2–5, may 2013.

[59] S. P. Milovanovic, M. Ramezani Masir, and F. M. Peeters, "Bilayer graphene Hall bar with a pn-junction," *Journal of Applied Physics*, vol. 114, no. 11, p. 113706, 2013.